Building a Cross-Cavity node for Quantum Processing Networks

A Dissertation presented

by

Bertus Scholtz Jordaan

to

The Graduate School

in Partial Fulfillment of the

Requirements

for the Degree of

Doctor of Philosophy

in

Physics

(AMO Quantum Information Technology)

Stony Brook University

December 2018

Stony Brook University

The Graduate School

Bertus Scholtz Jordaan

We, the dissertation committe for the above candidate for the

Doctor of Philosophy degree, hereby recommend

acceptance of this dissertation

Prof. Eden Figueroa - Dissertation Advisor
Associate Professor, Department of Physics and Astronomy

Prof. Harold Metcalf - Chairperson of Defense
Professor, Department of Physics and Astronomy

Prof. Vladimir Korepin - Committee member
Professor, Department of Physics and Astronomy

Prof. Jonathan Simon - External member
Associate Professor, Department of Physics, University of Chicago

This dissertation is accepted by the Graduate School

Dean of the Graduate School

Abstract of the Dissertation

Building a Cross-Cavity node for Quantum Processing Networks

by

Bertus Scholtz Jordaan

Doctor of Philosophy

in

Physics

(AMO Quantum Information Technology)

Stony Brook University

2018

Worldwide there are significant efforts to build networks that can distribute photonic entanglement, first with applications in communication, with a long-term vision of constructing fully connected quantum processing networks (QPN). We have constructed a network of atom-light interfaces, providing a scalable QPN platform by creating connected room-temperature qubit memories using dark-state polaritons (DSPs). Furthermore, we combined ideas from two leading elements of quantum information namely collective enhancement effects of atomic ensembles and Cavity-QED to create a unique network element that can add quantum processing abilities to this network. We built a dual connection node consisting of two moderate finesse Fabry-Perot cavities. The cavities are configured to form a cross-cavity layout and coupled to a cold atomic ensemble. The physical regime of interest is the non-limiting case between (i) low N with high cooperativity and (ii) free-space-high-N ensembles. Lastly, we have explored how to use light-matter interfaces to implement an analog simulator of relativistic quantum particles following Dirac and Jackiw-Rebbi model Hamiltonians. Combining this development with the cross-cavity node provides a pathway towards quantum simulation of more complex phenomena involving interacting many quantum relativistic particles.

Dedication Page

To my parents,
Barend and Petro Jordaan
and grandparents,
Boet and Bertha Scholtz and Dale Jordaan

Contents

List of Figures

Acknowledgements

Finishing my Ph.D. and my dissertation wouldn't have been possible if it wasn't for the hard work and support of many people. I would like to acknowledge their help here.

To my advisor or *Doktorvater* if you like, Eden Figueroa, thank you for all the opportunities you gave me over the last few years. I learned many skills and material from you as an experienced and intelligent physicist. The way you have enthusiastically shared your knowledge has always inspired me. I have enjoyed your visionary management and appreciated you as a supportive mentor. Eden as the strong leader you are, you have always pushed me to do more than I think I could. Even though I sometimes did it kicking and screaming, I think it allowed me to develop a lot of independence and self-confidence.

I would like to thank my committee for their time and patience. Thank you, Professor Harold Metcalf, for the support throughout my graduate career and the scientific discussions we've had. Thank you, Professor Korepin for the interest in the quantum simulation work and the ideas for its future. A particular word of thanks to my external examiner, Professor Jonathan Simon, that after short notice came on board with incredible positivity and encouragement.

I am grateful to Chris Ianzano who I had the privilege to teach, work with and train throughout my time at Stony Brook. Our discussions on where to take the project next gave me a great example of how productive teamwork can look like. Your willingness to take considered risks has rubbed off on me. You helped me develop my understanding of optics, cavities, and atomic physics and my teaching skills. I also appreciated your help during thesis writing. Finally, thank you for putting up with measuring all the beam coordinates and the many times you had to align the cavities!

Mehdi Namazi was an incredible friend and colleague over the last few years. In your own unorthodox way, you were also integral in teaching me how to stand on my own two feet. The many successful projects we did together is a testament to how we made a great team.

I was lucky enough to have Guodong Cui and Samet Demircan to join the MOTley crew in the last year and a half. You two came in at a critical time, and your hard work in the lab, enthusiastic participation in discussions and critical eyes gave the project the right amount of push to get it to the point we needed. I can't think of better hands to leave the experiment in.

Connor Kupchak and Christian Nölleke were big role models. Connor's hard work and "get down to business" attitude was instrumental in my deve-

lopment. Thanks for the friendship that has endured. Thank you, Christian, for the impactful work you did in the short amount of time that you helped us out. I went back to your notes and codes numerous times and could always learn something. Your insights in physics and career development have always given me a refreshingly different perspective.

Sonali Gera, thank you for your friendship and Mael Flament, for breathing new energy into the lab with your impressive work ethic and optimism. Thank you to Zak Burkley, Carl Cheung and Sam Rind for the foundation you built for the cavity experiment. I would also like to acknowledge Reihaneh Shahrokhshahi and Steven Sagona-Stophel for the interesting physics discussions, learning and for their hard work on the phase experiments.

I would like to thank our collaborators Changsuk Noh, Dimitris Angelakis and Paolo Villoresi. I enjoyed the work we did together. A special thanks to Giuseppe Vallone and Alessia Scriminich, whose visits were very productive and were essential times of learning for me.

To Professors Metcalf, Weinacht and Schneble, thank you for allowing us as a new group to borrow so many optics and optomechanics.

To Mark, JT and Jeff from the machine shop, thank you for the incredible work you did with the holders of the cavities. Thank you for the help and friendly demeanor when I had questions about using the machine shop.

Thank you for Sara Lutterbie and Don Sheehan for the help and great demeanor while making the administration easier during my time at Stony Brook.

Beyond the lab, I made many friends in the AMO groups. Thanks to my "brother-in-arms" Spencer Horton, who had helped and supported me through so many parts of the Ph.D. Together we passed the comprehensive exams, the dreaded few years in the middle when nothing seemed to work and even after you graduated your encouragement during the thesis had immeasurable value. Thanks for all the great walks, talks, debates and arguments! Ludwig Krinner, thank you for sharing your depth of knowledge, always being willing to help and the example you were. Thank you to the other friends I made in the basement, especially Yusong Lui, Arthur Zhao, Brian, and Melissa Arnold.

For four years of my Ph.D. I the home in Townehouse drive provided a welcome refuge. I would like to thank Zoya for being such an incredible friend, roommate, and dance-partner over these 6 odd years. Without your emotional support, I would have given up years ago. Your example of excelling in work and life and positivity has been inspiring to watch close-up. Thanks for introducing me to many people who became close friends. Thank you, Chirag, for being the best birthday partner and such a good and steadfast friend. A special thanks to Abhishodh Prakash who was a joy to have as a roommate

and who helped me in many material and immaterial ways. Thank you to Naveen Prabhakar, Mat Madhavacheril, Mike Hazoglou, and Anusha Shankar for adding so much joy to our home the times you would visit.

In graduate school, I've made the acquaintance of too many other fantastic people to mention individually. More than once, I paused in thankfulness that my life has brought me to this place where I could have such engaging discussions about important things going on in the world.

I would also like to thank my friends back in South Africa that always had a word of encouragement - Charl, Anel, Suzanne, Nicole, Nina, Michael, Andre, Chantelle, and Christopher.

Though I haven't met the following people, their books or videos have made a profound impact on my ability to get work done and helped me finish the Ph.D.: Linda Sapadin, Gretchen Rubin, Jon Acuff, Russell Barkley, Dale Carnegie, Caren Baruch-Feldman, Angela Duckworth, Jessica McCabe, Chris Croft, Dave Crenshaw, and Todd Dewett.

To Herta and Wolfgang Wulf, my host-parents in Stony Brook, I enjoyed all the enjoyable times you invited me into your home.

I would like to thank my parents, Barend and Petro Jordaan for all of their support throughout my life and especially over the last few years with my Ph.D. Studying in a different country, wasn't always easy for them or me, but they supported me in uncountable many ways. They always listened and offered solutions during the numerous Skype calls and endured me complaining about just not being able to handle the stress of graduate school. Thank you, Ouma Bertha, for all the love and support throughout the years. I would like to posthumously thank my two grandparents that passed away during my Ph.D., Ouma Dale and Oupa Boet. Ouma Dale, always believed that I could do anything and was my greatest fan. I would also like to thank Oupa Boet whose work ethic, and attention to detail was ever an example to me. My thesis is therefore dedicated to my parents and grandparents. I would like to thank my bother Jaco, whose immense success has always been a beacon of motivation and to thank my extended family for their steadfast support.

I want to thank the Fulbright foundation and the South African National Research Foundation for funding.

Please forgive me if I have left someone out, but know that I am grateful to all who have made this degree possible.

Chapter 1

Introduction

The audacious idea of creating an interconnected network of quantum devices that share entangled information and operate in both a nonlocal and nonclassical [1, 2] way has interested people for a very long time [3, 4, 5]. What has changed is that science and technology, in different levels of size and scale has made it a realistic goal to build elementary quantum networks within the next decade. Our group has started a research program that aims to contribute to this grand goal by advancing prudent and practical systems that reduce the technical overhead and get interconnected nodes as soon as possible. I have been involved from the start of this endeavor, and this thesis will highlight my contributions to the achievements we have reached over the last few years and present the outlook over the next few years.

On a small scale, people are creating quantum processors and control over quantum matter and single photons, have been achieved. The success of loophole-free Bell Inequality tests [6, 7, 8] and the quantum satellite [9] has shown that we can control quantum systems over larger and larger distances. From the photonic side, the success of LIGO [10] in detecting gravitational waves is a testament to how incredible control one can have on laser and optical systems.

Developments in quantum communication together with quantum key distribution protocols have enormous potential for the creation of a global, secure quantum information exchange network[11, 12, 13, 14, 15, 16, 17].

A notable example of an elementary network will be the modular connection of quantum cryptography systems operating over free-space quantum channels [18], assisted by room temperature quantum memories increasing the distance, security, and connectivity of quantum key distribution protocols [19, 20].

Quantum memories also address another challenge for quantum networks.

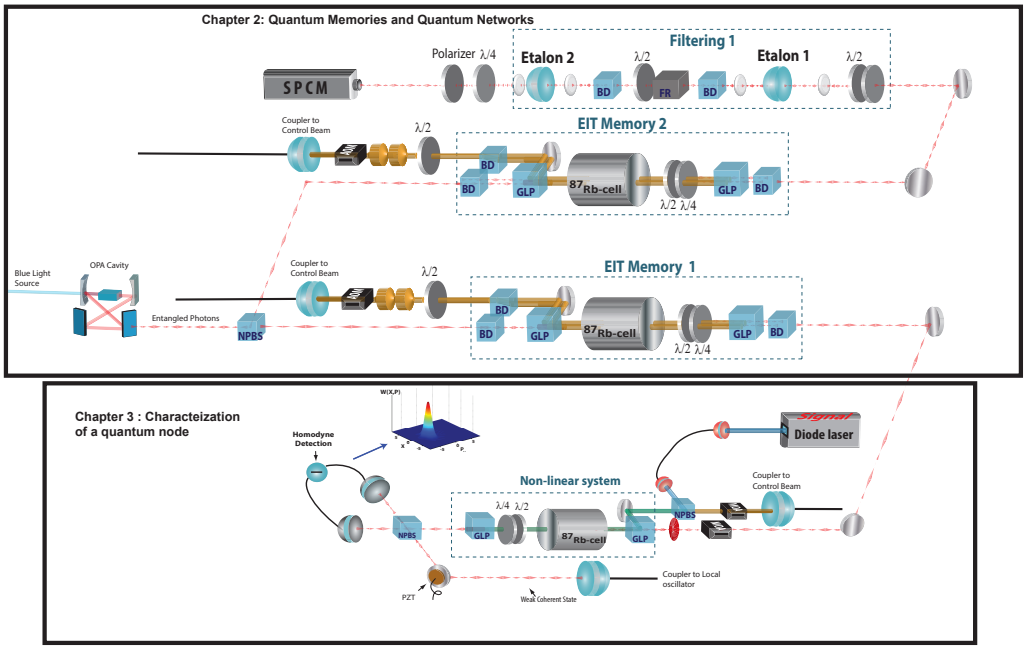

Figure 1.1: Developing a small-scale quantum network at Stony Brook University. Room-temperature quantum memories [23] storing polarization qubits (top block) that have been cascaded with each other [24] into a network with non-linear nodes [25] (bottom block) characterized using csQPT.

The distances are severely limited because of the lack of the analogous amplifier for fiber losses of classical networks that the quantum no-cloning theorem prevent.[21, 22]. Quantum memories form a part of the quantum repeater solution for this problem.[21, 22].

In our lab, we have created an elementary quantum network with room-temperature devices as shown in Fig1.1.

In addition to quantum repeater nodes, scaling of networks would require some processing capacity. The current state of the art entanglement sources are too probabilistic and lead to an exponential decrease in success with time and distance.[26]. Deterministic protocols of producing entanglement include deterministic Bell-State measurements [27, 28], assistance with entanglement purification [22]. Interconnects between different quantum systems [4], and quantum error correction [29] also require processing nodes in the network.

The relationship between communication and processing is not a new one, as both the point-contact transistor and the junction transistor emerged from a program of basic research on solid-state physics because executives were see-

king solid-state devices to replace the vacuum tubes and electromechanical relays that served as amplifiers and switches in the Bell Telephone System [30]. Which makes the parallel development of processing nodes for quantum networks and distributed optical quantum computing [2, 31] all the more sensible.

The system in which we are working toward achieving these goals is that of ensembles of multi-level atoms, laser control and linear optical resonators. More specifically we use near-infrared laser light (780nm,795nm) to control rubidium atoms through cooling [32] and coherent light-atom interactions namely EIT [33].

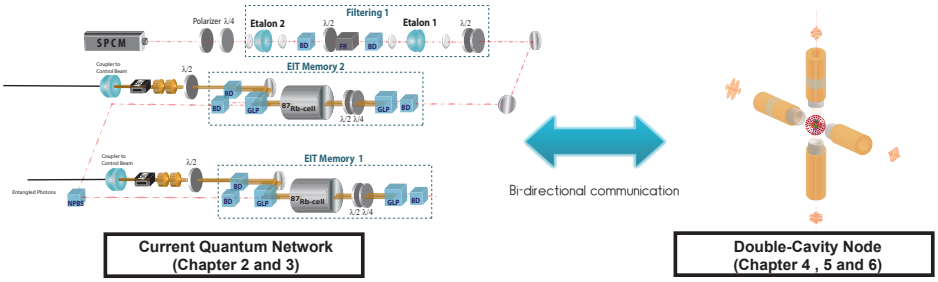

Figure 1.2: Towards a quantum processing network. A double cavity atom ensemble system can form different roles in our quantum network, due to the bi-directional communication that we can establish for photons originating from the memories or the cavity/ensemble device. We take advantage of using the same atoms and laser fields in order to establish this relationship

For creating processing nodes, we were motivated by the state-of-the-art results of single-atom cavity QED [2, 28, 27] and the success of our and other ensemble memories to construct a system where two optical resonators are coupled to an multi-particle atomic medium. Increasing the number of optical channels allows different network topologies, such as butterfly networks [34, 35] and the potential for strong non-linear interactions between qubits. Creating photon sources for the memories from this setup is also a option since the similarities of our atomic systems allow for bi-directional connection between the cavity node and the memories.

I will discuss these topics in the following way:

In Chapter 2, I discuss the network infrastructure that we have built, which starts with laser systems and a stand-alone node, the room-temperature qubit memory. The route to $> 90\%$ qubit fidelities is discussed through our experimental and simulation investigations. I also discuss the first experiment in which we show the network operation of the memory connected to a quantum

cryptographic channel. (Fig. 1.1).

In Chapter 3, I present the results of our first entry into quantum processing node design and characterization. Using the same room-temperature ensemble system, and coherent state quantum process tomography (csQPT) we characterize the nonlinear effects of an N-type extension to EIT. (Fig. 1.1)

In Chapter 4, I give the motivation for and details of building a double cavity system coupled with a laser-cooled atomic system. The details of the magneto-optical trap, optical cavities, and detection are described. (Fig. 1.2)

In Chapter 5, I present the theory and results of the first measurements showing that our atomic system is coupled to the cavities. I present the theory behind the scattering model [36] that our experiments are compared to, and the simulation was done to evaluate it. (Fig. 1.2)

In Chapter 6, I present the results of our first application for quantum processing nodes, the quantum simulation of relativistic particles. The simulation is done using Spinor of Slow Light from tripod linkage systems of EIT, in the room-temperature systems.

In Chapter 7, I explain some experimental and theoretical results that put us on the way to achieve double cavity EIT in the system. (Fig. 1.2)

In Chapter 8, I present the final outlook for the research.

Chapter 2

Quantum networks at Stony Brook

2.1 Introduction

The importance of quantum networks was highlighted in the introduction, but when addressing such a diverse and broad subject, one needs to think about where one needs to start. A critical look at the limitations of quantum networks reveal a few good places to start. One of which is the limitations that currently exist in the distance that these networks operate.[26]. The lengths are limited because of the different kinds of losses that can be experienced in the system namely power loss and entanglement losses. I will only be concerned with power loss.

When a quantum particle, such as a photon, is sent over a communication channel there is a certain probability of losing it. This problem also exists in classical networks, but the quantum no-cloning theorem [21, 22] prevents the analogous amplifier that has been developed for power losses of classical networks. That is to say, that if the information is encoded in a basis set of the quantum properties of the particle, such as polarization or spatial mode, the information cannot be copied onto another particle.

To move quantum information over large distances, this would need to change. One of the most well-researched solutions is that of the quantum repeater[21, 22]. The procedure of the quantum repeater is shown in 2.1. In step 1, two entanglement sources send their states to no-less than *four* quantum memories. In step 2, the entanglement is stored in the quantum memories. The quantum memories allow for synchronization between the different sources and also provides for an accumulation of two pairs since the entanglement

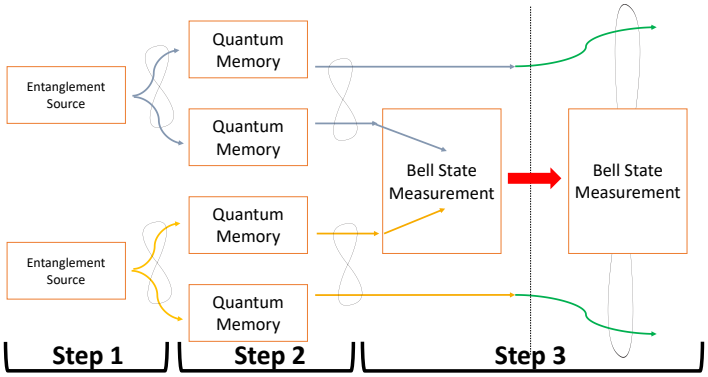

Figure 2.1: **Diagram of a Quantum Repeater**. In step 1, two entanglement sources send their states to no-less than *four* quantum memories. In step 2, the entanglement is stored in the quantum memories. In step 3 two unentangled (one from each entangled pairs) interfere at a beam splitter. When the projection on a Bell state is measured, the two photons that were not part of the measurement end up entangled.

sources will have imperfect duty cycles. In step 3 two unentangled (one from each entangled pairs) interfere at a beam splitter. When the projection on a Bell state is measured, the two photons that were not part of the measurement end up entangled. Now you have entanglement between far-off photons that have *never interacted before*[37]. This together with entangle purification and nested protocols, lead to an increase in the distance that can be reached by quantum networks.[21, 22]

The need for *four* quantum memories highlights the importance of scalable quantum memories to realize this protocol. Our lab has started to address this problem with developing room-temperature quantum memories that analyze both the physical limitations of noisy quantum systems and the technological obstacles in creating a scalable platform for quantum information. In this chapter, I present the theoretical foundation of our memories, the lab infrastructure we built, the characterization, modeling and improvement that led to the creation of the first polarization qubit memories operating at room-temperature. The ending of the chapter shows how these memories can be used in currently relevant quantum cryptographic networks. **Disclaimer:** This chapter contains work included in the papers :

- Kupchak, C., Mittiga, T., Jordaan, B., Namazi, M., Nlleke, C. and Figueroa, E. Room-Temperature Single-photon level Memory for Polarization States Scientific Reports,2015, 7658

- Namazi, M., Kupchak, C., Jordaan, B., Shahrokhshahi, R. and Figueroa, E. Ultralow-Noise Room-Temperature Quantum Memory for Polarization Qubits Phys. Rev. Applied, 2017, 8, 034023

- Namazi, M., Vallone, G., Jordaan, B., Goham, C., Shahrokhshahi, R., Villoresi, P. and Figueroa, E., Free-Space Quantum Communication with a Portable Quantum Memory Physical Review Applied, 2017, 8, 064013

In all these works I contributed to the implementation and modeling of the experiment, the interpretation of the results and the writing of the manuscript. Permission from the other authors was received to include the results in this thesis.

2.2 Theory

2.2.1 EIT

We use Electromagnetically Induced Transparency or EIT to do store photons in an atomic ensemble. In a three-level atom, a strong control field and a low-level probe field couples in a lambda configuration. We use Rubidium 87. EIT is an interference phenomenon between the decay channels of two transitions, which changes the shape of the resonance of the atoms. The difference in dispersion allows the pulses to be compressed and slowed down and the change in absorption provides the controllable transparency for the probe pulses. This can be seen using the following derivation from [33].

Starting with a three level atom with a Λ level scheme and an incident electric fields like shown in Fig. 2.2b you have a general Hamiltonian $H = H_0 + H_{\text{int}}$

The H_0 is given by

$$H_0 = \hbar \begin{bmatrix} \omega_1 & 0 & 0 \\ 0 & \omega_2 & 0 \\ 0 & 0 & \omega_3 \end{bmatrix} \tag{2.1}$$

And the interaction term given by

$$H_i nt = \vec{\mu} \cdot \vec{(}E) = -E \begin{bmatrix} 0 & 0 & \rho_{13} \\ 0 & 0 & \rho_{23} \\ \rho_{31} & \rho_{32} & 0 \end{bmatrix} \tag{2.2}$$

After the rotating wave approximation (RWA) and co-rotating frame trans-

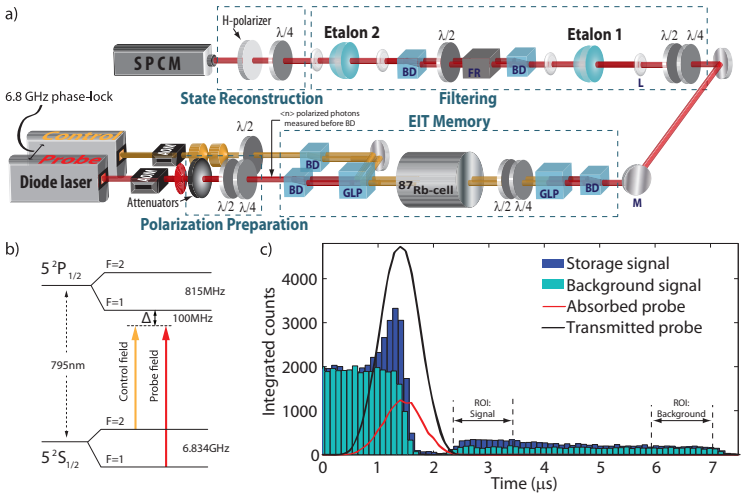

Figure 2.2: **Experimental setup and photon-arrival histograms.** (a) Experimental setup for polarization qubit storage in rubidium vapor at the single-photon level, including the stages of control-filtering. AOM: Acusto-optical modulators; BD: Beam displacers; GLP: Glan-Laser-Polarizer; FR: Faraday rotator; SPCM: Single-Photon-Counting-Module; L: Lens; M: Mirror. Probe: red beam paths; control: yellow beam paths. (b) Atomic-level scheme and EIT configuration. (c) Histograms of photon-arrival times, including the input pulse after transmission through the filtering stages (black line), input pulse after absorption in the cell (red line), storage experiment (blue bars) and background (light green bars). The region of interest (ROI) for the data analysis is also displayed.

formations this becomes

$$H = -\frac{\hbar}{2}\begin{bmatrix} 0 & 0 & \Omega_p \\ 0 & -2(\Delta_p - \Delta_c) & \Omega_c \\ \Omega_p & \Omega_c & -2\Delta_p \end{bmatrix} \tag{2.3}$$

The eigenstates when the two-photon $(\Delta_p - \Delta_c) = 0$ detuning is zero is

$$|a^+\rangle = \sin\theta\sin\phi|1\rangle + \cos\phi|3\rangle + \cos\theta\sin\phi|2\rangle \tag{2.4}$$
$$|a^o\rangle = \cos\theta|1\rangle - \sin\theta|2\rangle \tag{2.5}$$
$$|a^-\rangle = \sin\theta\cos\phi|1\rangle - \sin\phi|3\rangle + \cos\theta\cos\phi|2\rangle, \tag{2.6}$$

with

$$\tan(\theta) = \frac{\Omega_p}{\Omega_c}, \tan(2\phi) = \frac{\sqrt{\Omega_p^2 + \Omega_c^2}}{\Delta}. \tag{2.7}$$

The state $|a^o\rangle$ is the dark-state that has no decay term for in the optical regime. Coupling to this state makes the probe experience low-absorption transparency but a normal dispersion within the transparency window. This can be seen by evaluation the dynamics of the system using a master equation[33]. Starting with the time dependent Hamiltonian

$$H_{\text{int}} = \frac{\hbar}{2}[\Omega_p(t)\sigma_{31}e^{i\Delta_p t} + \Omega_c(t)\sigma_{32}e^{i\Delta_c t} + H.c.] \tag{2.8}$$

The master equation is

$$\begin{aligned}\frac{d\rho}{dt} = &\frac{1}{i\hbar}[H_{\text{int}}, \rho] + \frac{\Gamma_{31}}{2}[2\sigma_{13}\rho\sigma_{31} - \sigma 33\rho - \rho\sigma 33] \\ &+ \frac{\Gamma_{32}}{2}[2\sigma_{23}\rho\sigma_{32} - \sigma 33\rho - \rho\sigma 33] \\ &+ \frac{\gamma_{2\text{deph}}}{2}[2\sigma_{22}\rho\sigma_{22} - \sigma 22\rho - \rho\sigma 22] \\ &+ \frac{\gamma_{3\text{deph}}}{2}[2\sigma_{33}\rho\sigma_{33} - \sigma 33\rho - \rho\sigma 33]\end{aligned} \tag{2.9}$$

With the atomic polarizability given by

$$P(t) = n_{\text{atom}}[\mu_{31}\rho_{31}e^{-i\omega_{31}t} + \mu_{23}\rho_{32}e^{-i\omega_{32}t + c.c.}] \tag{2.10}$$

The off-diagonal elements of ρ are

$$\begin{aligned}
\rho_{32} &= \frac{i\Omega_c e^{i\Delta_p t}}{\gamma_{32} + i2\Delta_c}\rho_{12}, \\
\rho_{12} &= \frac{i\Omega_c e^{i\Delta_2 t}}{\gamma_{21} + i2(\Delta_c - \Delta_1)}\rho_{13}, \\
\rho_{31} &= \frac{i\Omega_p e^{i\Delta_p t}}{\gamma_{31} + i2\Delta_p} + \frac{i\Omega_c e^{i\Delta_c t}}{\gamma_{31} + i2\Delta_p}\rho_{21}.
\end{aligned} \tag{2.11}$$

This gives the susceptibility to be

$$\begin{aligned}
\chi^{(1)}(-\omega_p, \omega_p) = \frac{|\mu_{13}|^2 n_{\text{atom}}}{epsilon_0 \hbar} \\
\times \left[\frac{4\delta(|\Omega_c|^2 - 4\delta\Delta) - 4\Delta\gamma_{21}^2}{||\Omega_c|^2 + (\gamma_{31} + i2\Delta)(\gamma_{21} + i2\delta)|^2} \right. \\
\left. + i\frac{8\delta^2\gamma_{31} + 2\gamma_{21}(|\Omega_c|^2 + \gamma_{21}\gamma_{31})}{||\Omega_c|^2 + (\gamma_{31} + i2\Delta)(\gamma_{21} + i2\delta)|^2} \right]
\end{aligned} \tag{2.12}$$

2.2.2 Dark State Polaritons

Quantum mechanically we look at the three-level atom in the following way. A second quantization formalism allows us to break down the probe field into a sum over quantized modes. We also define a collective atomic operator over the atoms in the ensemble as a sum over individual atomic operators. Assuming the control field changes the state adiabatically allows for us to define a new pseudoparticle, the dark state polariton, that follows the same propagation equation as the electric field. It is a polariton because it is partly atomic state and partly electric field. The Dark state comes from the fact that atomic operator in the expression is over the two ground states that dont allow optical transitions between them. If the propagation of pulses are considered [38, 33], one can arrive at pseudo-particles that contain both the atomic population coherences and electric field. The solution to the combined system of equations is a superposition of $E(z,t)$ and $\sigma_{12}(z,t)$ and is called a Dark State Polariton (DSP), $\Psi(z,t) = \cos\theta E(z,t) - \sin\theta\sigma_{12}(z,t)$.

Storage of light in an atomic medium can then be seen as moving from sending in a DSP that is purely light, mapping to the atomic medium coherently as a mixed DSP, storing as an atomic-only DSP and reversing the process for retrieval.

2.2.3 From light storage to storage of polarization states

In the section above, EIT explains how we can store light in an atomic medium. An encoding mechanism is needed to store qubits. We use polarization states to encode our qubits.

Storage experiments for polarization qubits have to be tested against three mutually unbiased bases [39, 40, 41] of the qubit Hilbert space. These bases are

$$Z = \{|H\rangle, |V\rangle\} \tag{2.13}$$

$$X = \{|D\rangle = \frac{1}{\sqrt{2}}(|H\rangle + |V\rangle), |A\rangle = \frac{1}{\sqrt{2}}(|H\rangle - |V\rangle)\} \tag{2.14}$$

$$Y = \{|R\rangle = \frac{1}{\sqrt{2}}(|H\rangle + i|V\rangle), |L\rangle = \frac{1}{\sqrt{2}}(|H\rangle - i|V\rangle)\} \tag{2.15}$$

The fidelity is evaluated as

$$F = \frac{1}{2}(1 + \mathbf{S}_{out} \cdot \mathbf{S}_{in} + \sqrt{(1 - \mathbf{S}_{out} \cdot \mathbf{S}_{out})(1 - \mathbf{S}_{in} \cdot \mathbf{S}_{in})}) \tag{2.16}$$

The polarized qubits are split into two rails into the EIT memory by beam displacers allowing for simultaneous light-storage in both rails. The retrieved signals are then recombined with an oppositely oriented beam-displacer (Fig 2.2).

2.3 Lab infrastructure

2.3.1 Laser system

A system of optics, control optics and electronics are used to provide the coherent light-matter interfaces as discussed before and showed in Fig.2.2.

Our lab consists of 6 lasers of which 2 are Toptica TA PROs at 795nm, 2 Toptica TA PROs at 780nm and 2 are Toptica DLPros at 795nm. The following setups are how we lock the lasers to the rubidium transitions we need to address.

2.3.2 Rubidium lock

Light from the seed of the TApro laser that is locked to rubidium is split inside the laser before entering the amplifier system. We typically have 14mW of laser power entering the optical setup to the rubidium lock. This light is

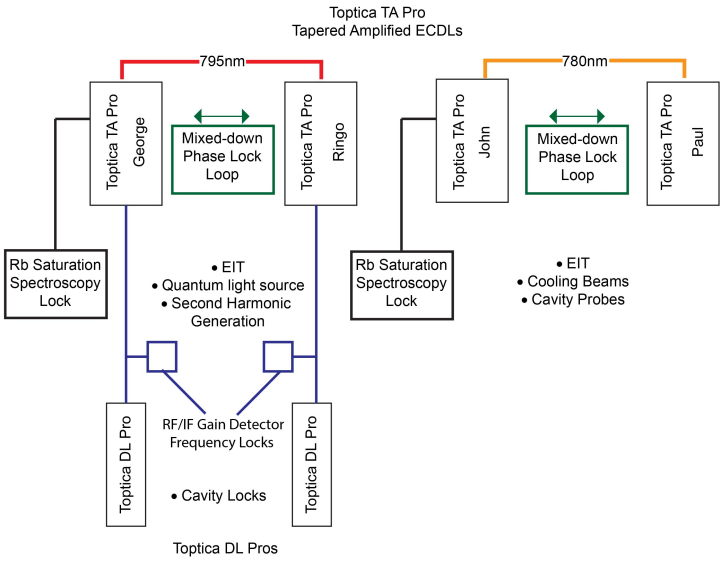

Figure 2.3: **Laser Systems of our lab**. Three locking schemes are shown. Saturation spectroscopy, phase locking and offset-frequency locking. One of each wavelength (780nm and 795nm) pair of lasers are used as a parent to the phase-lock system (Fig. 2.6) and locked to the rubidium lock (see Fig. 2.5).

sent through 2 AOMs that are driven at 200MHz each to give a total frequency difference of 400MHz.

This light is coupled to the CoSy module from Toptica. This setup is aligned in saturation spectroscopy configuration. The different parameters of the unit are set up in such a way such that two signals are retrieved. The first signal is the Doppler-broadened, saturation-free spectroscopy. The second is the "Doppler-free" spectrum that is generated from subtracting a multiple of the saturation-free from the saturated spectrum. These can be seen in Fig 2.4.

The remaining Lamb dips are inverted and amplified. Potentiometers in the CoSy control electronics control the amplification and subtraction.

These signals are sent to the Digilock module in our laser control system rack. A computer can control this module. This allows for scanning and visualizing the ^{87}Rb and ^{85}Rb spectrum in their natural abundance.

The Digilock software controls the locking of the laser by setting the control loop for in the Digilock module. The locking is done using a top-of-fringe locking technique.

A 97kHz signal modulates the Lorentzian peak of the spectrum - the value achieved by the internal switches closest to 100kHz. The modulation amplitude

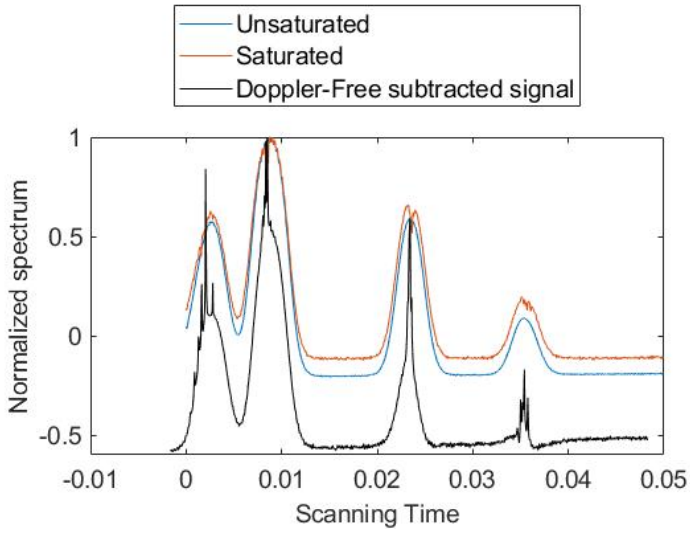

Figure 2.4: Saturation Spectroscopy for Rb Lock. A Doppler-broadened, saturation-free spectroscopy (blue). The saturated spectrum with characteristic Lamb dips (red). A "Doppler-free" spectrum (black) that is generated from subtracting a multiple of the saturation-free from the saturated spectrum.

had to be set to 0.002 to add the phase lock that is discussed in the following section. This is the lowest setting that allows for the top-of-fringe to still function. The modulation can be seen in Fig. 2.5.

This modulation produces a derivate of the signal after being demodulated. This can easily be seen in the following way. Let $F(\omega)$ be the signal of the spectrum at frequency ω. Since the modulation frequency is small compared to the frequency of the resonance, it can be considered a small deviation and the Taylor expansion gives:

$$F(\omega + \omega_\epsilon) = F(omega) + \frac{dF(\omega)}{d\omega}\omega_\epsilon \tag{2.17}$$

If the correct phase modulation is mixed with this signal, and the doubled frequency is filtered out, the only remaining signal is $\propto \frac{dF(\omega)}{d\omega}\omega_\epsilon$. This derivative of the Lorentzian peak gives an error-signal with a zero-crossing at the peak of the spectral peak. Close to the zero-crossing, the signal is linear enough for a Proportional-Integral-Differential (PID) control loop.

The Digilock has two PIDs. One for the current to the diode and another for controlling the voltage of the piezo actuator of the external cavity diffraction grating. Some of the parameters for our locking is shown in Table 2.1.

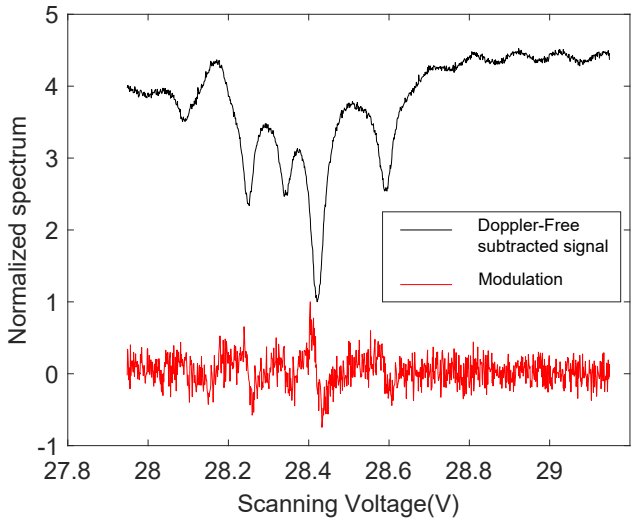

Figure 2.5: **Modulation for Rb Lock.**From the black spectroscopic signal, a locking signal is generated by modulation and demodulation (red). This locking signal is used for lock on of the laser in each wavelength pair (795nm and 780nm).

	PID1(Diode current)	PID2(External Cavity PZT Voltage)
P	8000	8000
I	30	30
D	0	0

Table 2.1: These are values for the different locking parts in the Digilock system.Two different locking loops are used, one for the laser diode current and one for the PZT voltage that controls the angle of the diffraction grating ing the external cavity of the laser seed. This can be controlled using software.

This scheme is done twice in the lab. Once at 780nm and once at 795nm. To have the phase control of the two-photon detuning required in EIT, each of these lasers are used to phase-lock with a second laser at 780nm and 795nm. This is shown in Fig. 2.3.

2.3.3 Phase lock

The phase lock system was designed to provide very fine frequency stabilization for two lasers. Light from the two lasers are coupled into the same fiber using a setup consisting of a NPBS. This produces a beat node between the two lasers.

$$
\begin{aligned}
E_Beat &= E_A\cos(\omega_A t) + E_B\cos(\omega_B t) \\
&= |E_A - E_B|\cos(\omega_A t) + |E_A - E_B|\cos(\omega_B t) \\
&\ldots + (E_A - |E_A - E_B|)\cos(\omega_A t) + (E_B - |E_A - E_B|)\cos(\omega_B t) \\
&\approx E_{overlap}\cos(\frac{\omega_A+\omega_B}{2} + \frac{\omega_A-\omega_B}{2}t) + E_{overlap}\cos(\frac{\omega_A+\omega_B}{2} - \frac{\omega_A-\omega_B}{2}t) \\
&= E_{overlap}\cos(\frac{\omega_A+\omega_B}{2}t + \frac{\omega_A-\omega_B}{2}t) + E_{overlap}\cos(\frac{\omega_A+\omega_B}{2}t - \frac{\omega_A-\omega_B}{2}t) \\
&\approx E_{overlap}\cos(\omega t + \frac{\delta}{2}t) + E_{overlap}\cos(\frac{\omega t}{2} - \frac{\delta}{2}t) \\
&\approx E_{overlap}\Big[\cos(\omega t)\cos(\frac{\delta}{2}t) - \sin(\omega t)\sin(\frac{\delta}{2}t)\Big] \\
&\ldots + E_{overlap}\Big[\cos(\omega t)\cos(\frac{\delta}{2}t) + \sin(\omega t)\sin(\frac{\delta}{2}t)\Big] \\
&= 2E_{overlap}\cos(\omega t)\cos(\frac{\delta}{2}t)
\end{aligned}
$$

since the photodiode measure intesity, the signal is of the form

$$
\begin{aligned}
& && (2.18)\\
I &\propto E^2 && (2.19)\\
&= E^2_{overlap}\cos(2\omega t)\cos(\delta t) && \\
&\text{after DC filtering} && (2.20)
\end{aligned}
$$

I mixer combines this beat note carrier frequency δ with a 6.834MHz (+80MHx for 780nm and +40 MHz for the 795nm system) signal generator. The mixed-down signal is amplified and sent to a Toptica mFALC (mixing, Fast Analog Laser Controller).

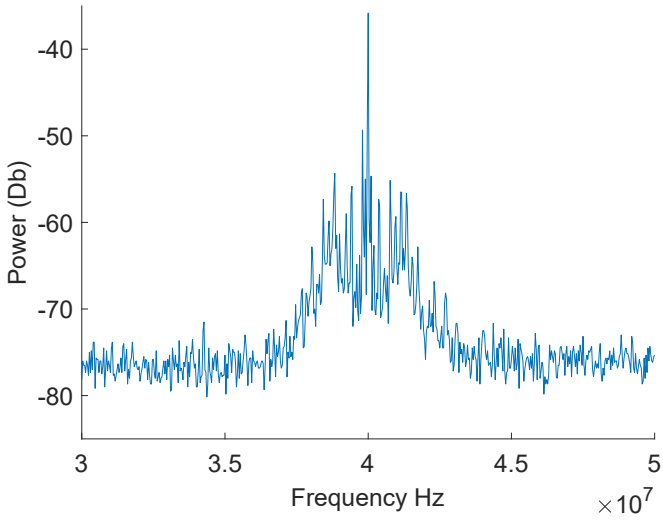

Figure 2.6: Phase Lock Spectrum of 795nm phase-lock system. Locking point at 40MHz. The characteristic wing structure of an OPLL is seen where $|G| = 1$ i.e the magnitude of the feedback gain reaches 1.

Electronics in the Toptica mFALC, handle phase detection from this beat node. A mixer acts as an analog phase-detector as the mixed-down signal has a $\propto \cos(\delta_{\text{mixed-down}})$ behaviour. When the frequency between the input and reference signal becomes 0, the phase response has a linear region.

Switches in the Toptica mFALC tune different filters (integrators and differentiators) that shape the control filter for the PLL. Two different output control the PZT and the diode current.

The feedback loop allows us to phase-lock the laser and gives a typical OPLL signal as shown in Fig. 2.6

2.4 Room-temperature polarization state memory

This section highlights the evaluation and measurement in [42].

2.4.1 Experimental setup for storing polarization states

To store a polarization qubit of the form $|\psi_{in}\rangle = cos\theta|H\rangle + e^{i\phi}\sin\theta|V\rangle$ (where $|H\rangle$ and $|V\rangle$ refer to horizontal and vertical polarization states and θ and

ϕ correspond to the polar and azimuthal angles on the Poincaré sphere, respectively), we map the photonic polarization mode onto two spatially separated atomic ensembles concurrently under conditions of electromagnetically-induced transparency (EIT), in a single ^{87}Rb vapor cell at 62° C, containing Ne buffer gas (Fig. 2.2a).

We employed two external-cavity diode lasers phase-locked at 6.8 GHz to resonantly couple a Lambda configuration composed of two hyperfine ground states sharing a common excited state. The probe field frequency is stabilized to the $5S_{1/2}F = 1 \rightarrow 5P_{1/2}F' = 1$ transition at a wavelength of 795 nm (red detuning Δ=100 MHz) while the control field interacts with the $5S_{1/2}F = 2 \rightarrow 5P_{1/2}F' = 1$ transition. The level scheme is shown in (Fig. 2.2b).

The pulse shapes for both the probe and control fields are independently controlled with acousto-optical modulators. Two polarization beam displacers are used to create a dual-rail set-up allowing simultaneous light-storage in both rails. A set of polarization elements supply 42 dB of control field attenuation while maintaining 80% probe transmission. Furthermore, two monolithic, temperature-controlled etalon resonators provide a further 102 dB of control field extinction. Both etalons have a thickness of 7.5 mm, a radius of curvature of 40.7 mm, a free spectral range of 13.3 GHz, finesse of 310 and transmission linewidth of 43 MHz. Together they achieve a probe transmission of 16%. In between the etalons we have implemented a polarization insensitive Faraday isolator to suppress any back reflections of the etalon surfaces (transmission $\sim$ 50 %). Overall, our setup achieves 144 dB control field suppression while yielding a total 4.5% probe field transmission, hence exhibiting an effective, control/probe suppression ratio of 130 dB.

2.4.2 Evaluation of polarization states

The result of storing 1μs long probe pulses containing 1.6 photons on average is shown in Fig. 2.2c as a blue storage histogram. The background (control-only) histogram is shown in green.

Two regions of interest (ROIs) are defined. A signal ROI from 2.4 μs to 3.4 mus and a bacground ROI from 6μs to 7 μs (shown in Fig. 2.2). The efficiency is calculated as

$$\eta = \frac{I_{\text{S-ROI}} - I_{\text{B-ROI}}}{I_{\text{No Atoms}}} \tag{2.21}$$

where I is the integrated counts over the signal (S-ROI) and background (B-ROI) ROIs. $I_{\text{No Atoms}}$ is the total counts in the transmitted probe through

the filtering system without atomic interaction (black line in Fig. 2.2). The signal to background ratio (SBR) is calculated as

$$\text{SBR} = \frac{I_{\text{S-ROI}} - I_{\text{B-ROI}}}{I_{\text{B-ROI}}} \tag{2.22}$$

The complete evaluation of the polarization fidelity is done in four steps: First, we measure the Stokes parameters of our input probe polarization entering the first beam displacer. Second, we perform the same procedure for pulses that have propagated through the entire setup (cell included) and the filtering stages in the absence of EIT conditions (see Fig. 2.2c, red line). Third, we estimate and apply the unitary rotation to the original input states due to all optical elements by using a least squares fit method which fits them to the transmitted states without changing their lengths (see Fig. 2.7c).

The fidelity between the rotated inputs ($\mathbf{S}_{in}$) and the transmitted states was greater than 99% on average (green dots in Figure 2.8a). This step can alternatively be achieved in the system using linear optical elements. Lastly, we perform a polarization analysis of the retrieved pulses ($\mathbf{S}_{out}$) which are then compared directly to the rotated input states to obtain a fair estimation of fidelity with respect to the original input states. The fidelity is evaluated as given by (2.16).

In Figure 2.7d, the Poincaré sphere associated with the retrieved states clearly shows orthogonal but shortened vectors (as compared to the input) due to the influence of decoherence processes and the uncorrelated background counts. Table 2.5.1 summarizes the storage efficiency, SBR, and fidelity reconstruction for all the polarization inputs for $\langle n \rangle = 1.6$ and shows an average fidelity of 71.5 ± 1.6%. It is important to note that this fidelity value is dependent on the SBR and therefore reliant on the ROI being analyzed due to the dynamics of our memory system.

Input	**H**	**V**	**D**	**A**	**R**	**L**	**Average**
SBR	1.68	1.1	1.27	1.15	1.53	1.38	1.35 ± .09
Fidelity (%)	71.3	79	69.2	71.4	70.2	67.6	71.5 ± 1.6
Efficiency (η)(%)	7.9	5.3	4.6	3.8	5.6	5.9	5.5 ± .6

Table 2.2: Storage of polarization states in ROI. The high fidelity of the V polarization was one of the reasons we investigated noise from the control field background.

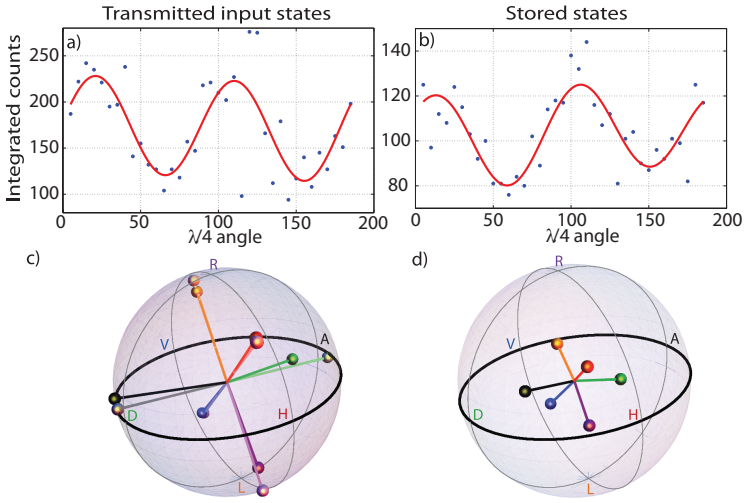

Figure 2.7: **Polarization analysis.** Storage of polarization qubits at $\langle n \rangle = 1.6$. (a) Stokes reconstruction of $|D\rangle$ transmitted input. (b) Stokes reconstruction of $|D\rangle$ stored and retrieved output. The red line is the fitting used to estimate the Stokes vector. (c) Poincaré sphere of the transmitted input polarizations (bold colors) and Poincaré sphere of the rotated input polarizations (light colors). (d) Poincaré sphere of the stored and retrieved output polarizations.
Reproduced from [42]

2.4.3 Direction for improvement

Reducing the ROI to 500 ns (2.5 to 3.1 μ s) our average fidelity increases to 74.3 $\pm$ 1.6 with an average SBR of 1.61 $\pm$ 0.14. This fidelity value is relevant since it is above the optimal classical fidelity for Poissonian distributed coherent states containing an average 1.6 photons and memory efficiencies of unity given by $\langle F_{\text{opt}} \rangle = \sum_{n=1}^{\infty} F_{\text{opt}}(n) p_n / [1 - p_0] \approx 73.4\%$, where $p_n = e^{-\langle n \rangle} \langle n \rangle^n / n!$. However, our measured fidelity is less than the classical threshold of 84.9 % needed for more elaborate strategies that take into account the sub-unity efficiencies of our memory [43, 44]. Nonetheless, we will show that in our current physical conditions, our fidelity is more dependent on the SBR than the efficiency. Due to the small leakage of the control field, we also observe a weak vertical polarization of the mostly randomly polarized background noise which leads to higher fidelities for $|V\rangle$ as shown in Table 2.5.1.

To reach single-photon level quantum memory operation, we embarked on two different analysis. Understanding and modeling the background noise and using auxiliary fields in the memory.

2.5 Modeling of noise in the system

2.5.1 Theory in first paper

To quantify the influence of the background on the fidelity of the qubit memory, we have performed a series of polarization measurements (using the ROI as before), where we modify the SBR by increasing the input photon number (see Figure 2.8a). We can see that an average fidelity of $\sim 85\%$ (the classical threshold necessary when considering our memory efficiencies) can be achieved with an SBR of ~ 4.0, which is a four-fold increase over our current experimental implementation at the single photon level. The maximum achievable fidelity is ultimately limited by the technical imperfections of the setup and the decoherence of the hyperfine ground state superposition. The scaling of SBR can be understood with a theoretical model considering a dual-rail optical quantum memory based on two atomic ensembles, with each ensemble assumed to be a Poissonian source of the uncorrelated signal and background photons.

The dependence of the fidelity associated with different ROIs can be explained by the temporal envelope of the retrieved signal being defined by two different time scales. The first is a coherently driven process (EIT retrieval at the beginning of the retrieved pulse) and a second incoherent contribution due to spontaneously emitted photons (latter part of the retrieved pulse).

Hence, by decreasing the ROI, we post-select the part of our retrieved signal corresponding to the coherent storage process.

We assume that each of the ensembles stores one of the two polarization components with efficiency η before recombination and read out. The probability of producing n signal photons and m background photons (for both ensembles) is $P'_s(n) = \frac{(\eta p)^n}{n!}e^{-\eta p}$ and $P'_{bg}(m) = \frac{q^m}{m!}e^{-q}$ respectively. Here p is the average number of input photons, and q is the average number of background photons. Note that two ensembles emitting Poissonian noise with mean photon number $q/2$ into the same spatial mode behave as one noise source with mean photon number q.
In the instance of n signal and m background photons being produced, the probability of detecting a signal photon is simply $\frac{n}{n+m}$, and of detecting a background photon is $\frac{m}{n+m}$ for non photon-number resolving detectors. Then, in general, the probabilities of detecting up to order N signal $P_s(\eta, p, q, N)$ and background $P_{bg}(\eta, p, q, N)$ photons are

$$P_s(\eta, p, q, N) = \sum_{n=0}^{N}\sum_{m=0}^{N} P'_s(n)P'_{bg}(m)\frac{n}{n+m} \tag{2.23}$$

$$P_{bg}(\eta, p, q, N) = \sum_{n=0}^{N}\sum_{m=0}^{N} P'_s(n)P'_{bg}(m)\frac{m}{n+m}, \tag{2.24}$$

and the fidelity is

$$F = \frac{P_s(\eta, p, q, N) + \frac{1}{2}P_{bg}(\eta, p, q, N)}{P_s(\eta, p, q, N) + P_{bg}(\eta, p, q, N)}. \tag{2.25}$$

The theoretical estimation for the fidelity scaling (solid red line in Fig. 2.8a) has been calculated using independently measured parameters η=0.055 and $q = 0.005$ (see Figs. 2.8 a-b).

2.5.2 Background analysis

Furthermore, we experimentally characterize the background noise. To do so we integrate the number of counts in the ROI of histograms corresponding to measurements of only the background (cell present, control field only, green dots in Fig. 2.9 a) and only the technical background (control field only, no cell, red dots in Fig. 2.9 a) and divide by the number of experimental runs. This provides the number of background counts per retrieved pulse. We repeat this procedure for several values of the control field power.

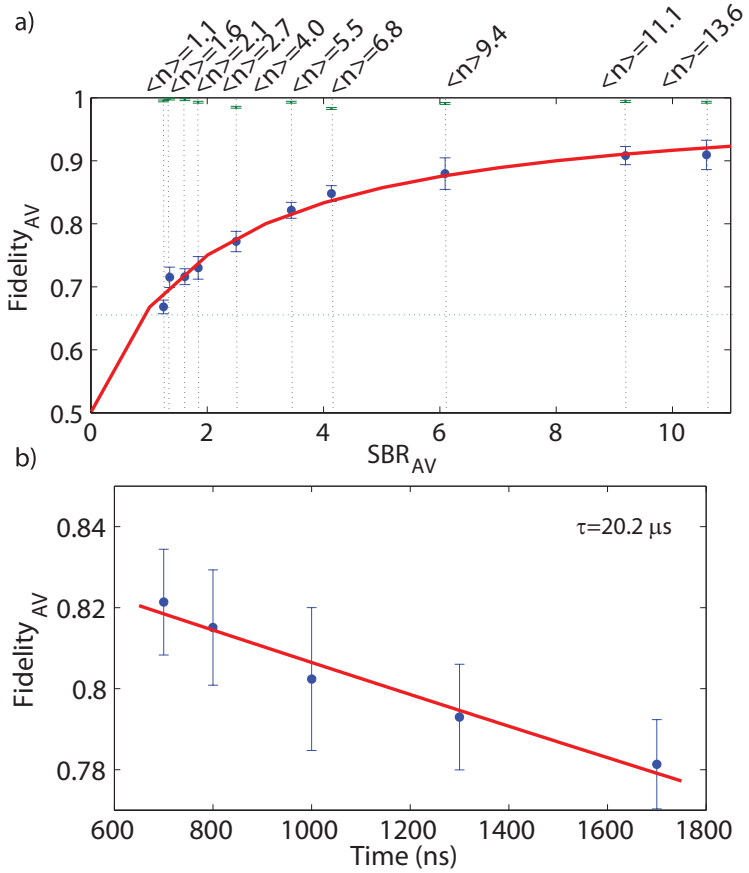

Figure 2.8: **Analysis of the quantum memory.** (a) Scaling of the average fidelity of the qubit memory for varying signal-to-background ratio (transmitted states: green dots, retrieved states: blue dots). Shown in black are the average input photon numbers and the corresponding average signal-to-background ratio. The red line shows the results of a theoretical model considering a dual-rail optical quantum memory, assuming each ensemble to be a Poissonian source of the uncorrelated signal and background photons. (b) Coherence time measurement for $\langle n \rangle$=6 (blue dots) and lifetime fitting (red line). The error bars correspond to the standard error of the mean of the individual state fidelities and outweighs the errors associated with the individual state fidelity measurements. Reproduced from [42]

.

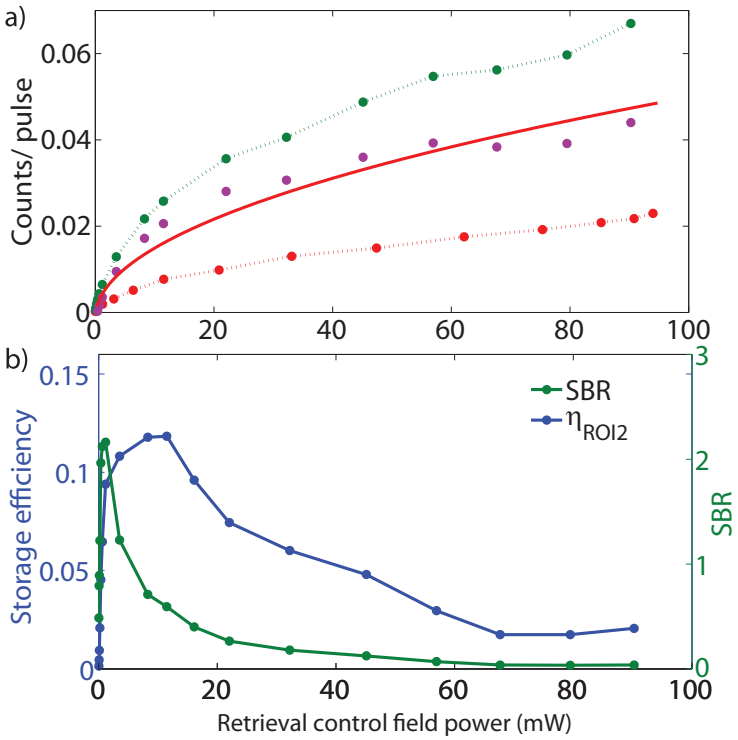

Figure 2.9: **Background noise characterization.** (a) Counts in ROI per retrieved pulse for background (green dots) and technical background (control field only, no cell, red dots) with increasing control field power. The purple dots show the background counts with the technical counts subtracted and the red line is a fitting of a function $\propto \sqrt{POWER_{\Omega_c}}$. (b) Storage efficiency in the ROI (blue dots) and signal to background (green dots) as a function of control field power. Reproduced from [42]

We can see that the entire background is composed of photons from both leakage of the control field (technical background) and those generated by atomic processes such as spontaneous Raman scattering and four-wave mixing [45, 46]. The purple dots in Fig. 2.9a show the resultant of the technical counts subtracted from the background and the red line is a fitting of a function $\propto \sqrt{POWER_{\Omega_c}}$ (or the square root of the control field power), where Ω_c is the Rabi frequency of the control field.

We analyze the behaviour of the storage efficiency in the ROI (η, blue dots in Fig. 2.9 b) and SBR (using the same ROI, green points in Fig.2.9 b) as a function of the control field power. We can see that the efficiency has a substantially different scaling than the SBR and that their maxima do not match. We notice that while our setup is capable of maximum storage efficiencies of $\eta_{max} \sim 16\%$ (over a larger ROI), the ideal signal to background value for quantum memory functionality corresponds to suboptimal storage efficiencies.

2.5.3 Modelling of noise for ultra-low noise operation

Surpassing any classical strategy exploiting non-unitary memory efficiencies requires increasing the SBR substantially. To do so we have developed a model of the quantum dynamics of the room temperature quantum memory. We start by considering atoms exhibiting a four-level energy level scheme interacting with two laser fields, Ω_p (probe) and Ω_c (control), with one-photon detunings Δ_{13} and Δ_{23} respectively (here $\Delta_{13} = \Delta_{23}$, see Fig. 2.2 b). We include the off-resonant interaction of the control field with a virtual state $|4\rangle$. The phenomenological Hamiltonian describing the atom-field coupling in a rotating frame is:

$$\begin{aligned}\hat{H} &= H_{\text{EIT}} + H_{\text{Background}} \\ H &= \Big\{(-\Delta_{13}+\Delta)\hat{\sigma}_{11} - (\Delta_{13}-\Delta_{23})\hat{\sigma}_{22} - \Omega_p E_p \hat{\sigma}_{31} - \Omega_c E_c \hat{\sigma}_{32}\Big\} \\ &\quad + \Big\{ -\frac{\alpha}{\omega_{43}+\Delta}\Omega_c E_c \hat{\sigma}_{41} - \frac{\alpha}{\omega_{43}+\Delta}\Omega_c E_c \hat{\sigma}_{42} - (\Delta_{13}-\omega_{43})\hat{\sigma}_{44}\Big\} + \text{H.c}\end{aligned} \tag{2.26}$$

where Δ is the laser detuning, α is the coupling strength to the virtual state, $\hat{\sigma}_{ij} = |i\rangle\langle j|, i, j = 1, 2, 3, 4$ are the atomic raising and lowering operators for $i \neq j$, and the atomic energy-level population operators for $i = j$ and $E_p(z,t)$ and $E_c(z,t)$ are the normalized electric field amplitudes of the probe and control fields. The equation for H_{EIT} differs from (2.3) by a simple rescaling of the

energy levels that simplify the addition of the virtual state $|4\rangle$. We use the master equation:

$$\begin{aligned}\dot{\hat{\rho}} = -i[\hat{H}, \hat{\rho}] + &\sum_{m=1,2} \Gamma_{3m}(2\hat{\sigma}_{m3}\rho\hat{\sigma}_{3m} - \hat{\sigma}_{33}\hat{\rho} - \hat{\rho}\hat{\sigma}_{33}) \\ &+ \sum_{m=1,2} \Gamma_{4m}(2\hat{\sigma}_{m4}\rho\hat{\sigma}_{4m} - \hat{\sigma}_{44}\hat{\rho} - \hat{\rho}\hat{\sigma}_{44}) \\ &+ \Gamma_{12}(2\hat{\sigma}_{21}\rho\hat{\sigma}_{12} - \hat{\sigma}_{11}\hat{\rho} - \hat{\rho}\hat{\sigma}_{11})\end{aligned}$$

together with the Maxwell-Bloch equation, $\partial_z E_p(z,t) = i\frac{\Omega_p N}{c}\langle\hat{\sigma}_{31}(z,t)\rangle$, to calculate the expected retrieved pulse shape $E_{OUT}(t)$ and the storage efficiency bandwidth response $\eta(\Delta)$. Here L is the atomic sample length, Γ's being the decay rates of the excited levels, c is the speed of light in vacuum and N the number of atoms.

2.5.4 Simulation results

The room temperature response is calculated by convolving two storage efficiency bandwidths $\eta_1(\Delta)$ and $\eta_2(\Delta)$ (corresponding to two excited states in the rubidium D1 line manifold, blue line in Fig. 2.7 b) with a distribution

$$A(\Delta) = A(2\pi v/\lambda) = \frac{\sqrt{\ln 2}}{W_d\sqrt{\pi}}\frac{1}{1 + (2\Delta)^2/W_d^2} \tag{2.27}$$

. We have set W_d to 960MHz to include also pressure broadening effects (obtained from a fit on the measured transmission profile (Fig. 2.7 a)). Defining

$$\Delta = \Delta_j = \Delta_0 + j\Delta_{step}$$

we calculate the response as

$$\eta(\Delta_j) = \sum_{i=-i_{max}}^{i_{max}} A(\Delta_i)\eta(\Delta_{j+i}). \tag{2.28}$$

The resultant broadened storage bandwidth $\eta_{RT}(\Delta)$ is presented in Fig. 2.7 b (solid red line). We also account for the varying optical depth at different Δ by multiplying $\eta_{RT}(\Delta)$ by the measured transmission profile $T_{RT}(\Delta)$ (see Fig. 2.7 a). The resultant is the room temperature efficiency bandwidth (see Fig. 2.7 c red line).

We perform storage experiments for $1/\sqrt{2}(|H\rangle + |V\rangle)$ qubits with a storage time of 700 ns over a Δ region of 4 GHz. Fig. 2.7c compares these results to our model. The most striking observation is that the maximum storage efficiency is not achieved on the atomic resonance, but at detunings beyond the Doppler width. The maximum efficiencies are at $\Delta = 500$ MHz (red detuned) and $\Delta = 1.3$ GHz (blue detuned).

2.5.5 Etalon results

Having found non-trivial regions of optimal operation, we now simulate the quantum dynamics of the atomic system when no probe field is present. The contribution of the Stokes field in the memory background is calculated using an extra term to $E_p(z,t)$ relative to $\langle\hat{\sigma}_{42}(z,t)\rangle$. The numerical values used are $\Gamma_{3m} = 3MHz$, $\Gamma_{4m} = 1GHz$ and the decoherence rate between ground states 0.1kHz. The background response $Q(\Delta)$ is the combination of two quantum fields. Firstly, from transition $|1\rangle$ to $|3\rangle$, which is narrow and associated to photons incoherently scattered from state $|3\rangle$. This is a result of population exchange with the virtual state $|4\rangle$ mediated by decoherence rates between the ground state $|1\rangle$ and $|2\rangle$. Secondly, from the $|2\rangle$ to $|4\rangle$ transition, which is broad and associated to photons scattered from the virtual state $|4\rangle$ (Stokes field) through an off-resonant Raman process (see dotted red line in Fig. 2.10a) [45, 46]. These two fields differ by 13.6 GHz.
We test our model by detecting background photons passing our filtering elements after exciting the atoms only with control field pulses (fixed Δ, varying etalon detunings, dots in Fig.2.10a).

These measurements are accurately resembled (see solid blue line in Fig. 2.10a) by convoluting $Q(\Delta)$ with the etalon transmission function $E(\Delta) = \frac{(1-A)^2}{1+R^2-2R\cos(\frac{2\pi\Delta}{FSR})}$ (dashed blue line in Fig. 2.10a). The total response is the sum of two convolutions calculated separately for each of the response background components (dotted red line in Fig 2.10a) and normalized to the input number of background photons before the etalon. We have used R= 0.9955, A=$2 * 10^{-4}$ and a FSR= 13.6GHz.

We obtain the room temperature background response $Q_{RT}(\Delta)$ by considering two background responses $Q_1(\Delta)$ and $Q_2(\Delta)$ (corresponding to two excited transitions of the rubidium D1 manifold, see blue dotted line in Fig. 2.10 b) and convoluting them with the velocity distribution of the moving atoms (see Fig. 2.10b red line). This model is in agreement with measure-

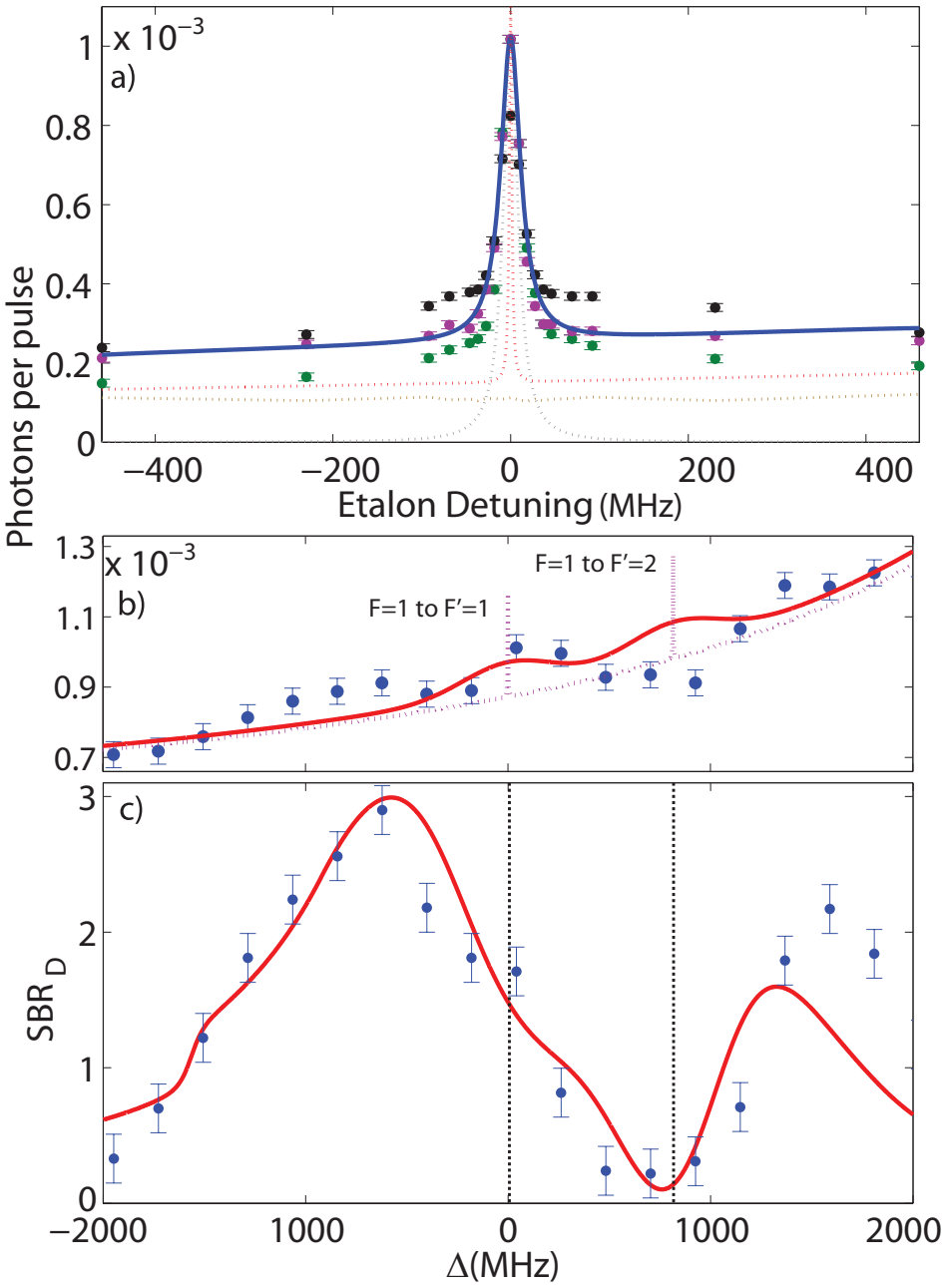

Figure 2.10: (a) Cold atom background response $Q(\Delta)$ (dashed red-line) featuring the contributions of incoherent scattering and Stokes fields; etalon transmission profile (dashed blue line); convoluted response indicating the background transmission through the filtering elements (solid blue line); experimental background measurement for $\Delta = -500$ MHz (green dots), 0 MHz (purple dots) and $+500$ MHz (black dots); technical background (brown dotted line). (b) Cold atom background bandwidths $Q_1(\Delta)$ and $Q_2(\Delta)$ for the two excited states of the rubidium D1 line manifold (the purple dotted line is a master equation prediction of the background bandwidth); warm atom background response $Q_{RT}(\Delta)$ ((the solid red line is the result of the convolution with a velocity distribution)); background measurements vs. Δ (blue dots). (c) Predicted room temperature signal to background ratio $SBR_{RT} \propto (\eta_{RT}(\Delta))(T_{RT}(\Delta))/(Q_{RT}(\Delta))$ (solid red line); SBR experimental measurements (blue dots). The error bars are statistical. Reproduced from [23]

ments of the background with fixed etalon detunings and varying Δ. Our final model for the room temperature SBR is calculated as

$$SBR_{RT} = (\eta_{RT}(\Delta))(T_{RT}(\Delta))/(Q_{RT}(\Delta)) \tag{2.29}$$

Which is the solid red line in Fig. 3c. This accurately predicts the features of the SBR measurements, with an optimal operational point corresponding to $\Delta = 500$ MHz from the central $F = 1$ to $F' = 1$ resonance.

2.5.6 Experimental verification of improved SBR/fidelity

The predicted optimal performance region is probed by using a one-photon detuning $\Delta \sim 250$ MHz (red detuned), and storing light pulses with an average $\langle n \rangle = 1$ photons and $|H\rangle$ polarization using only a single rail of the setup. The result shows an SBR of $\sim$6 for a storage time of 700 ns and a coherence of a few microseconds (See Fig.4a). Universal qubit operation is verified by using the dual-rail setup sending in and retrieving three sets of orthogonal polarizations, where now the background is inevitably twice that of the single rail. Our outcome was an average qubit SBR of 2.9 $\pm$0.04 with an average efficiency of 5.1% $\pm$ 0.07 for the six polarization states $|H\rangle, |V\rangle, |D\rangle, |A\rangle, |R\rangle, |L\rangle$ within a region of interest (ROI) of 400 ns (equal to the input pulse width) upon switching the control field (See Fig. 4b). The polarization of each of the retrieved qubit states is obtained with the following procedure [42]: (a) measurement of the polarization of all the input states, (b) qubit storage experiment and determination of the output Stokes vectors (S_{out}), (c) rotation of input states to match the orthogonal axis of the normalized stored vectors (S_{in}) and (d) evaluation of the total fidelity using (2.16). We obtained an average fidelity of 86.6$\pm$0.6%. This result is well above 71%, the fidelity achievable by a classical memory applying the intercept-resent attack and 83.6%, the maximum fidelity achievable considering the more elaborate classical strategy exploiting the non-unitary character of the memory efficiency, for a system using attenuated coherent states with $\langle n \rangle = 1$ and storage efficiency of 5% [44]. Furthermore, by reducing the ROI below 400ns, the qubit SBR is improved to 3.7 $\pm$0.09 corresponding to fidelities of $\sim$ 90%.

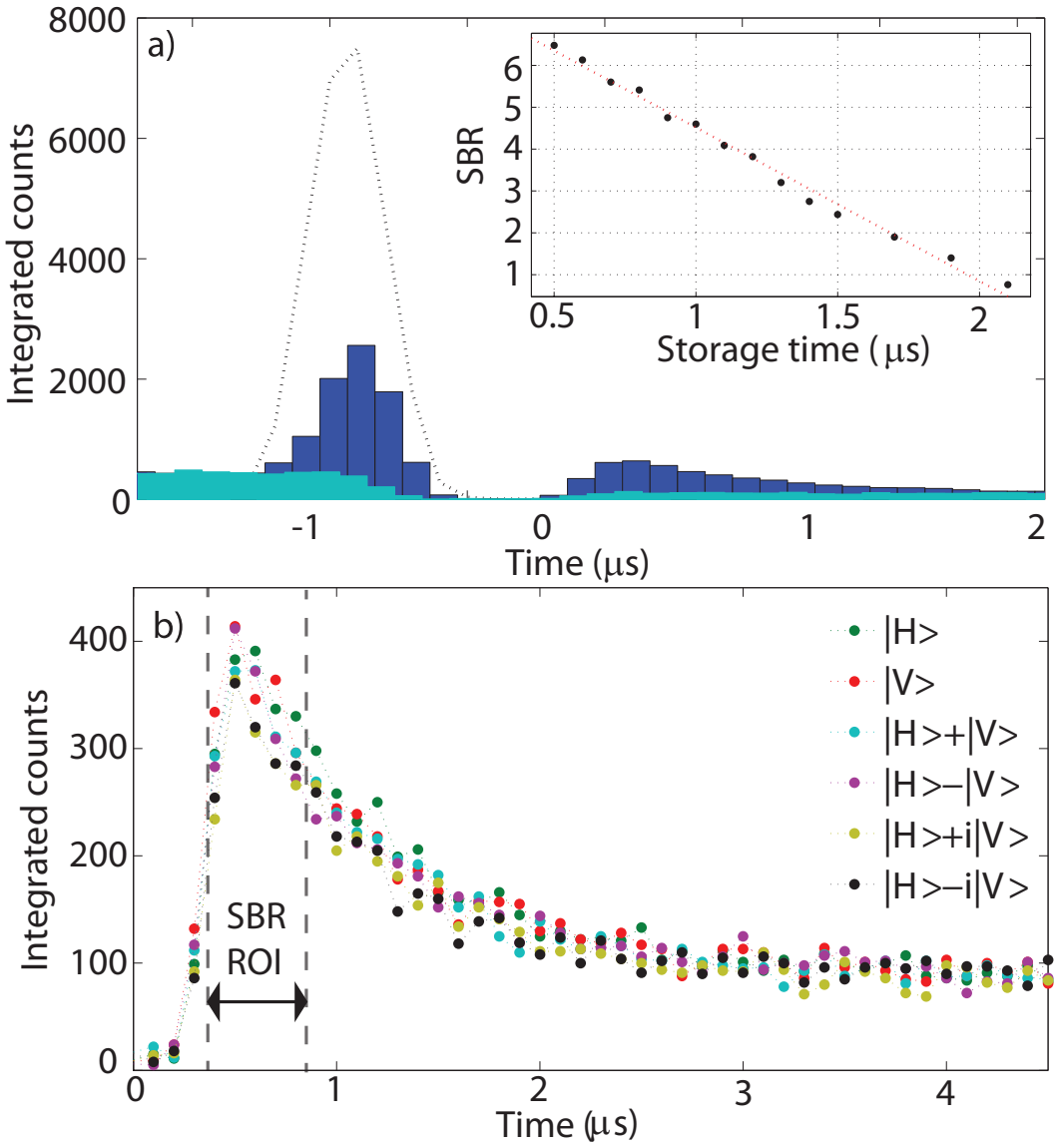

Figure 2.11: (a) Single rail storage with SBR ∼6 where the histogram of photons counts shows the retrieved signal (dark blue bars) compared background counts (light blue bars), the dotted black line shows the original pulse. Inset: SBR vs. storage time (black dots) and experimental fit (red line). (b) Storage efficiencies for six different input polarizations using the dual rail system. Reproduced from [23]

2.6 Ultra-low noise operation: NESIS and higher coherence time

We have assumed the background response $Q(\Delta)$ to be a combination of two quantum fields produced by different physical mechanism and differing by 13.6 GHz. We have tested this concept by replacing one of the etalons in the filtering system with a similar unit with a different free spectral ratio. This allows us to eliminate the background produced by scattering from the virtual state $|4\rangle$.

Moreover, we have pioneered a new noise reduction technique to show the pathway towards noise-free high fidelity operation. We achieve Noise Elimination using a Self Interacting Spinor (NESIS) by applying an additional weak auxiliary beam on resonance with the $5S_{1/2}F = 1 \rightarrow 5P_{1/2}F' = 1$ transition that remains on during the complete storage procedure. We create an interaction between two dark-state-polariton modes (spinor components), one formed by the auxiliary field and Ω_c, and one by Ω_c and the scattered photons from state $|3\rangle$ [47]. The interaction between the spinor components results in maxima/minima in the background noise depending on the phase relationship between the auxiliary and control fields, independently from the probe field. By storing and retrieving the probe light with a small two-photon detuning, we further guarantee independence between the two processes, thus creating a noise-free region without altering the retrieved photons.

Simultaneous improvements of coherence times to up to 50us comes from using different coatings and buffer gas in the cell, which reduces the decoherence from spin-spin collisions. Fig. 2.12a shows the obtained maxima/minima together with storage of pulses with $\langle n \rangle = 6$ and an increased control field power to highlight the dynamics above. By controlling the phases of the auxiliary and control fields using passive elements, we overlap the retrieved pulse with the noise-free region (see Fig. 2.12a), translating into an SBR > 25 for the single-photon level case.

Applying the NESIS technique together with active phase control in each of the qubit rails in the polarization quantum memory shown above correspond to qubit fidelities $> 98\%$. Having such noise-reduction techniques in place will permit the use of higher optical depths and control field powers, leading to storage efficiencies above 50%, already establishing our system as a viable alternative to cryogenic and cold-atom technologies [48, 43, 44]. Reducing the technical overhead allowed us to look into the network behavior of the memories.

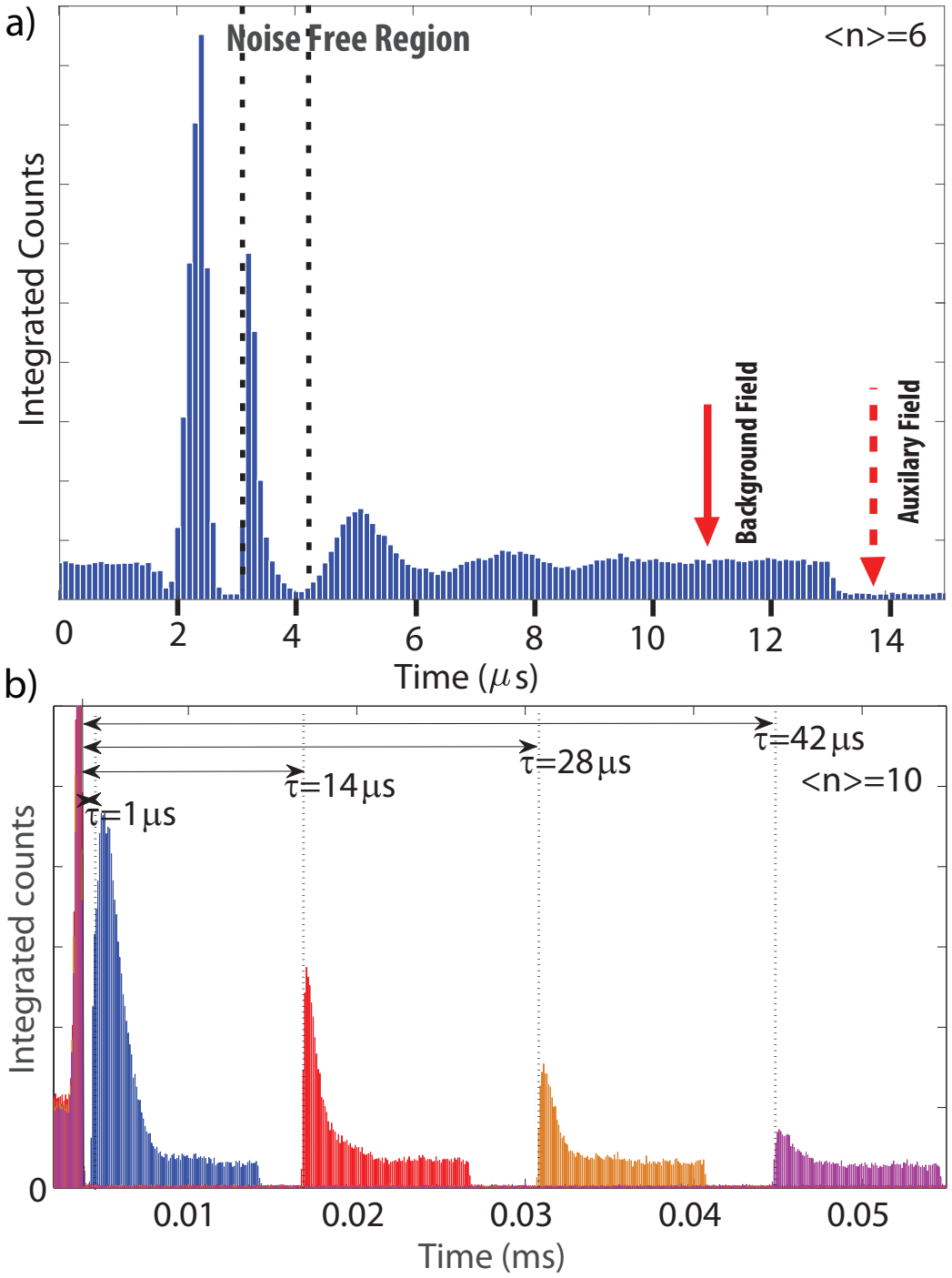

Figure 2.12: a) Noise reduction by introducing an auxiliary field (dashed red), the interaction between dark-state-polaritons creates a background free region. Retrieving the probe within this interval results in a SBR >25 for the retrieved probe field. b) Storage of light at the few photon level with storage times τ =1μs (η=11%, blue), τ =14μs (η=5.6%, red), τ =28μs (η=3.1%, orange) and τ =42μs (η=1.1%, purple). Reproduced from [42]

2.7 Network behavior of memories

The construction of an interconnected set of many quantum devices that performs secure communication protocols in outside settings and with moving targets it is now within experimental reach [37, 49, 4]. Therefore it is of utmost relevance to engineering elementary networks of a few quantum nodes and quantum channels to understand the potential of these novel architectures [50, 51, 52, 53]. The emergent behavior of such small quantum networks should allow us to realize more sophisticated quantum procedures [54]. An important example of such an elementary network will be the modular connection of quantum cryptography systems operating over free-space quantum channels [18], assisted by room temperature quantum memories increasing the distance, security, and connectivity of quantum key distribution protocols [19, 20].

2.7.1 Memories function within network

Our elementary quantum network starts with the creation of a sequence of four polarization states ($|H\rangle, |V\rangle, |D\rangle = 1/\sqrt{2}(|H\rangle + |V\rangle), |A\rangle = 1/\sqrt{2}(|H\rangle - |V\rangle)$) in a distant laboratory (Alice's station, Laboratory II in Fig. 2.13).

We create the qubits using 400ns-long pulses produced every 40 μs by four individual acousto-optical modulators (AOMs). The AOMs are each driven by independent sources regarding their amplitude and frequency modulation to compensate for small deviations in the length of each AOM track. The setup is designed to generate either an ordered sequence of four qubits in cycles of 160 μs (see Fig. 2.14) or a train of qubit pulses where the modulation sources are controlled by an FPGA chip programmed to trigger one of the four AOM's randomly. The resulting random sequence of pulses is attenuated to the single-photon-level and then sent into free space quantum channel module.

The qubits created in the Alice station propagate in a free-space quantum communication channel over a distance of $\sim$ 20m without shielding or vacuum propagation and are then directed to a quantum memory setup in a different laboratory. We have chosen the characteristics of this setup as a test bed of the interconnectivity of this station and the quantum memory setup under more challenging out-of-the-laboratory operation. Of particular interest are the shot-by-shot changes in the mean input photon number due to the air turbulence between the laboratories and the capability of the memory to receive random polarization inputs, pulse-by-pulse. By careful alignment, the loss in the free space propagation is set to be less than 4%. Together with 63% fiber coupling efficiency at the receiving end of the quantum memory setup, this

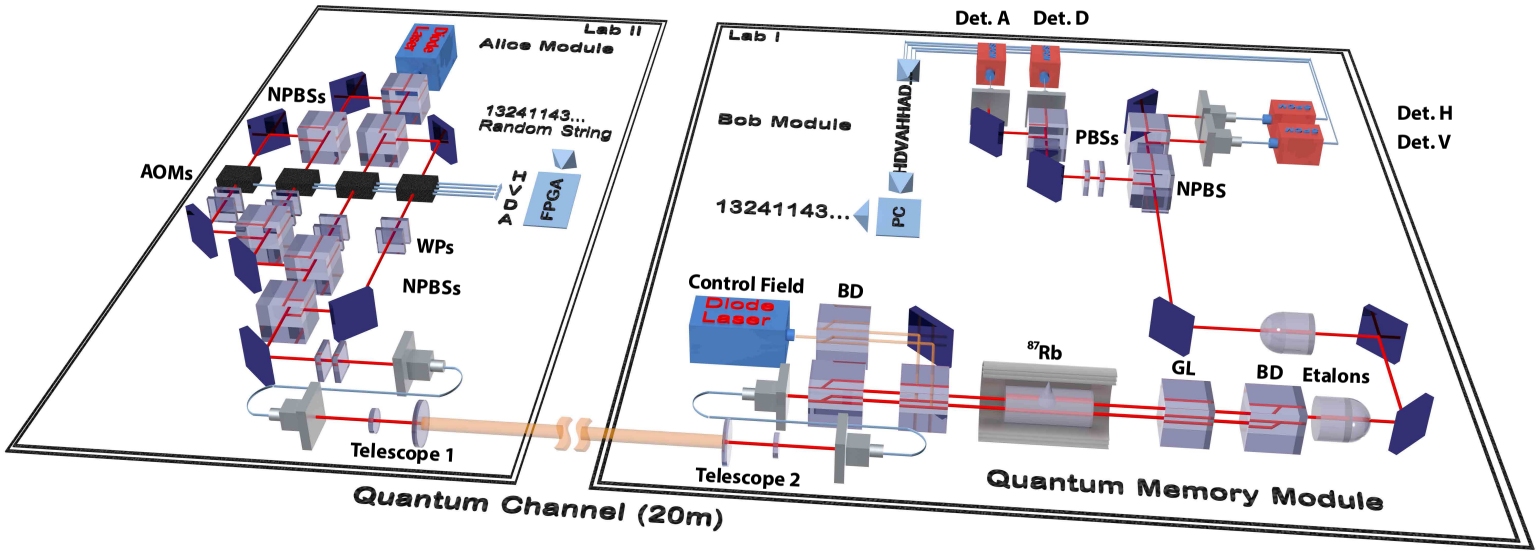

Figure 2.13: **Experimental setup for free-space quantum communication.** In Laboratory II Alice creates a random sequence of four orthogonal qubits ($|H\rangle, |V\rangle, |D\rangle, |A\rangle$). The 400ns-long qubits are produced every 40 μs. The qubits propagate in a free-space quantum communication channel over a distance of $\sim$ 20m. After propagation, the qubits are stored in a room-temperature quantum memory in Laboratory I consisting of a dual-rail rubidium vapor system. The control storage pulses are time-optimized to the arrival of the qubits in front of the memory. In Bob's site, a four detector setup measures all possible basis at the exit of the memory to determine the quantum bit error rate (QBER). PBS: polarizing beam splitter, WP: wave plates, AOM: acousto-optical modulator, BD: beam displacer, GL: Glan-laser polarizer. Reproduced from [55]

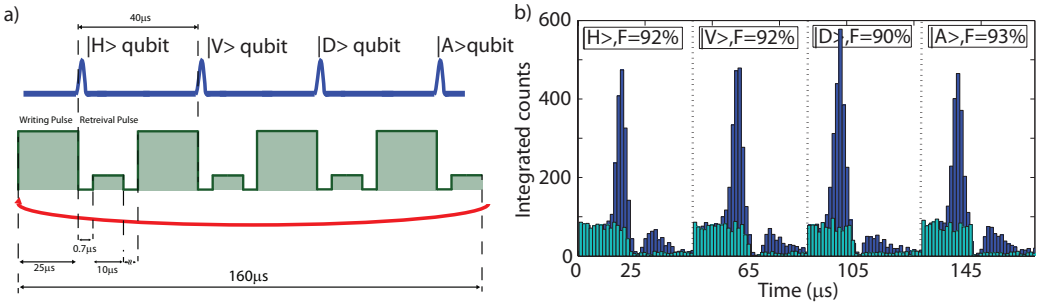

Figure 2.14: **Storage of a sequence of qubits.** (a) A stream of polarization qubits with on average 3.5 photons propagates through a free space quantum communication channel of 20m. In the quantum memory site, the single-photon level qubits are received and stored sequentially using timed control field pulses. (b) Histograms for each of the polarization inputs after storage (dark blue) and background floor (light blue). Each histogram is presented in a 2μs time interval (see dashed black divisions). The fidelities are estimated from the signal-to-background ratio.Reproduced from [55]

yields a total transmission of 59% for the quantum communication channel. The shot-by-shot fluctuations in the mean photon number were measured to be $\sim 5\%$.

The room-temperature quantum memory in which we store the incoming qubits is located in Laboratory I (Fig. 2.13). The quantum memory is based upon a warm ^{87}Rb vapor and controlled using electromagnetically induced transparency (EIT). Two independent control beams coherently prepare two volumes within a single ^{87}Rb vapor cell at 60° C, containing Kr buffer gas to serve as the storage medium for each mode of the polarization qubit. We employed two external-cavity diode lasers phase-locked at 6.835 GHz. The probe field frequency is stabilized to the $5S_{1/2}F = 1 \rightarrow 5P_{1/2}F' = 1$ transition at a wavelength of 795 nm while the control field interacts with the $5S_{1/2}F = 2 \rightarrow 5P_{1/2}F' = 1$ transition. Polarization elements supply 42 dB of control field attenuation (80% probe transmission) while two temperature-controlled etalon resonators (linewidths of 40 and 24 MHz) provide additional 102 dB of control field extinction. The total probe field transmission is 4.5% for all polarization inputs, exhibiting an effective, control/probe suppression ratio of 130 dB [23]. The control field pulses are time-optimized to the arrival of the qubits in front of the memory (see Fig. 2.14a).

After passing through the polarization independent frequency filtering system, the stored pulses enter the Bob module, which is equipped with a non-polarizing beam splitter (separating the $Z = \{|H\rangle, |V\rangle\}$ and $X = \{|D\rangle, |A\rangle\}$ bases) and two polarizing beam splitters whose outputs are detected by four

single-photon counting modules (SPCM). Each SPCM corresponds to a different polarization state. This allows us to compare the detected sequence with the qubits initially sent and estimate the influence of the photonic background of the memory in the evaluation of the QBERs.

We create histograms using the time of arrival and estimate a best-case-scenario fidelity of the stored polarization qubits containing on average 1.6 photons per pulse right before the memory.
We evaluate the signal to background ratio (SBR) in the measurements, defined as η/q, where η is the retrieved fraction of a single excitation stored in a quantum memory and q the average number of concurrently emitted photons due to background processes. Both are calculated by integrating the retrieved and background signals over 100 ns intervals. The fidelities are then estimated as $F = 1 - \frac{1}{2}\frac{q}{\eta}$ from (2.25). Our analysis shows that even with the additional constraint of shot-by-shot fluctuations in intensity due to free space propagation and the addition of randomly polarized background photons in the memory, maximum fidelities of 92% for $|H\rangle$, 92% for $|V\rangle$, 90% for $|D\rangle$ and 93% for $|A\rangle$ can still be achieved.
These results are clearly above the classical threshold limit of 85% for the corresponding efficiencies thus providing the necessary condition of full quantum memory operation [23].

After showing unbiased memory operation over the free space network, we now show that the connection also operates with high fidelity on a pulse-by-pulse basis, demonstrated by full polarization analysis at Bob location. This is done by randomizing the polarization input of the experiment. Further insight into our current capabilities is obtained by analyzing the quantum bit error rates (QBER) Q_X and Q_Z for X and Z bases after propagation and storage. Starting with pulses containing a high number of photons ($\sim$ 100 photons, see Fig. 2.15), we evaluated the QBER after storage of the random polarization states. An average QBER of 0.57% for the two orthogonal bases have been measured within a region of interest equal to the input pulse width. This QBER is compatible with the typical error rate obtained in a standard quantum key distribution experiment. The importance of this result is two-folded: 1) the storage process at room temperature does not intrinsically add non-unitary rotation to the states, and in the limit of high signal-to-background has a negligible effect on the total QBER; 2) the memory is capable of storing and retrieving a generic polarization qubits on a shot-by-shot level.

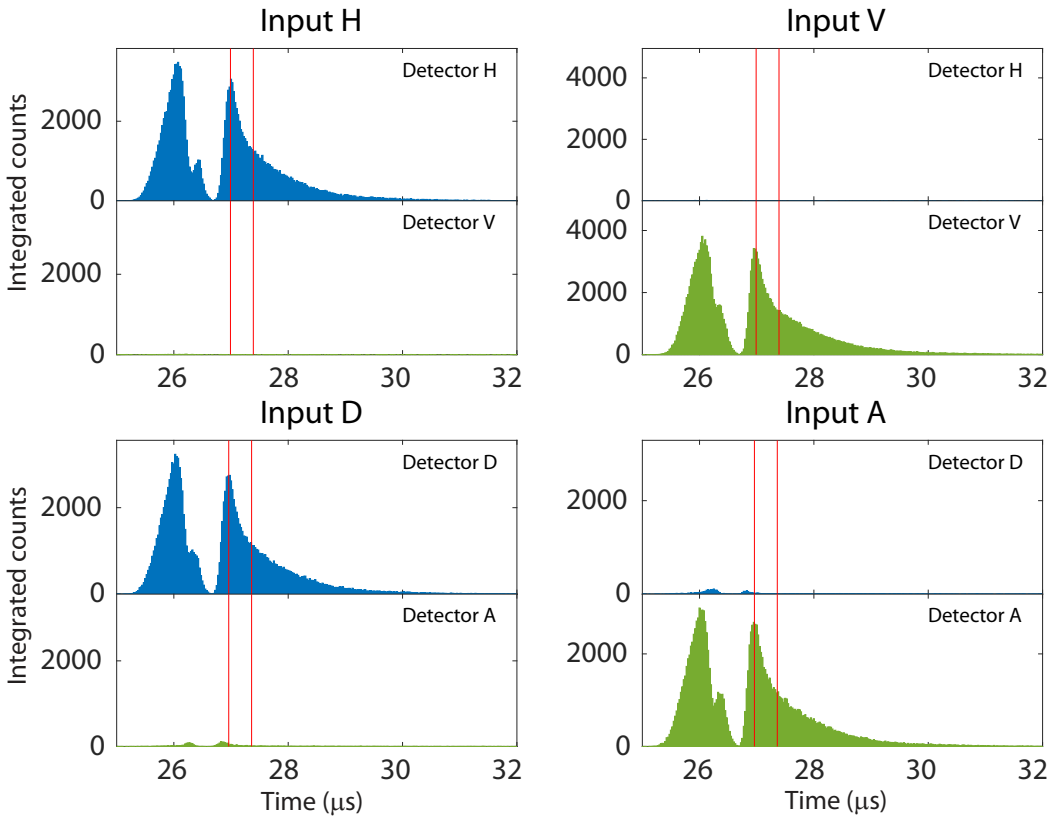

Figure 2.15: **QBER evaluation of the long-distance communication setup plus memory.** In the Bob site, the polarization states are received and stored sequentially in a room temperature quantum memory. We randomly choose one of the Z and X bases to measure the polarization state and then calculate the QBER over a region of interest equal to the input pulse width (red bars). We show histograms on the photons counts in each of the four polarizations. The first peak represents non-stored photon (leakage) while the second peak represents the retrieved photons. In an experiment with high input photon number, the obtained QBERs are less than 1%, as it can be seen in the low counts corresponding to undesirable polarization detections.Reproduced from [55]

2.7.2 Memories extend the possibilities of networks

Storage of a random sequence of polarization qubits at single photon level.

In our next experiment, the complete state measurement in the two bases was used again for an input of 1.6 photons before the memory, corresponding to 3.5 photons at Alice station. The evaluated QBERs after storage for polarization qubits are Q_Z= 11.0% and Q_X =12.9% over a 100 ns region (see Fig. 2.16). The increase of the QBERs is only due to the background noise which is much more significant at the single-photon level.

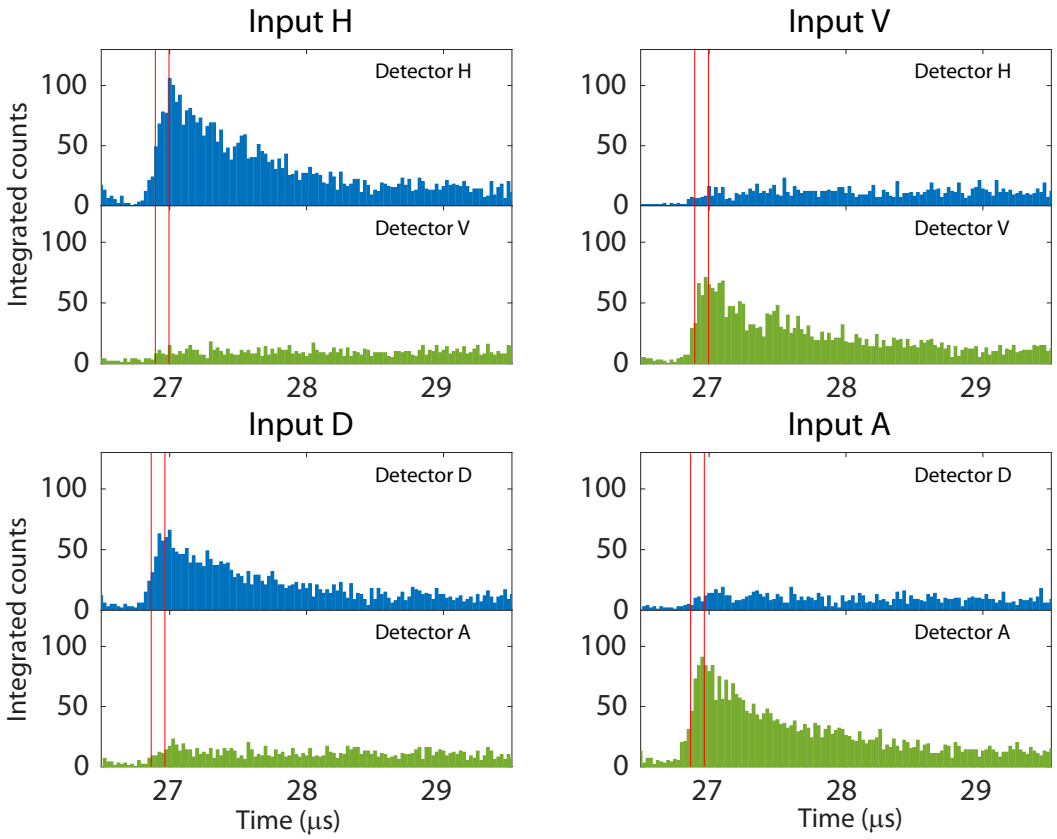

Figure 2.16: **QBER evaluation for single photon level experiment.** (a) The QBER is calculated in a $100ns$ window (red bars). QBER of 11.0% and 12.9% are respectively achieved for Z and X bases. At the single-photon level undesirable polarization rotations remain absent, noise in the orthogonal channel arises from control-field induced non-linear processes.

Nonetheless, the fidelities (corresponding to 1−QBER) remain higher than

the classical limit for the corresponding storage efficiency. Storage of superpositions $|D\rangle$ and $|A\rangle$ implies that the two rails forming the quantum memory store or miss the pulse coherently (in order to preserve the storage fidelity for that particular polarization), as opposed to retrieving $|H\rangle$ or $|V\rangle$ at any given time in a shot-by-shot experiment. This ability is crucial in networks performing quantum key distribution protocols, and it also shows that the memory is currently capable of receiving entangled polarization states without distorting them. We mention that this last experiment constitutes the quantum communication part of the well known BB84 protocol [56], with the addition of a synchronizing quantum memory between Alice and Bob.

After the improvements described in Sec. 2.6 some single rail experiments with lower noise could be done.

Figure 2.17a shows the results of a one-rail experiment including the auxiliary field (light-blue). We can see that after retrieval, the two dark-state-polariton interaction creates regions without the additional background noise. In this experiment, the auxiliary field strength is increased to highlight the ultra-low-noise regions. We measured an SBR ~ 26 for an input $\langle n\rangle \sim 1.3$ photons, only limited by the intrinsic attenuation of the filtering system (in contrast to being limited by the background noise). We can then infer a corresponding fidelity of 97% and QBER's $\sim 3\%$ for $\langle n\rangle \sim 1$ (see caption in Fig. 2.17).

The relevance of this new regime of operation is highlighted by analyzing its consequences to the possible quantum key distribution rate. The rate per channel efficiency for sharing a random secret key, encoded in random polarization states, between Alice and Bob (R) depends on the quantum bit error rate (QBER) and the mean photon number μ. In the infinite key-length limit, it is given by: $R = \mu(e^{-\mu}(1 - H(Q_X)) - H(Q_Z)f(Q_Z))$, where Q_X and Q_Z are the QBERs, $H(x)$ is the binary Shannon entropy function and $f(Q_Z)$ is the efficiency of the classical error correction protocol. We have evaluated the absolute key rate vs. the input photon number and our average QBER with $f(Q_Z)$=1.05 [57] for two cases. In the first case, we include the current quantum memory operation ($QBER = 11.9\%$ for $\mu = 1.6$). Fig. 2.17 b shows that this regime lies just outside of the region for positive key rate generation, indicating not fully-secure qubit communication. This situation is fully-corrected by applying the noise reduction techniques explained above, as in this new regime the operation ($QBER = 3\%$ for $\mu = 1$) is well inside the secure communication threshold. This is a significant achievement as our quantum network has all the elementary capabilities for quantum cryptography operation.

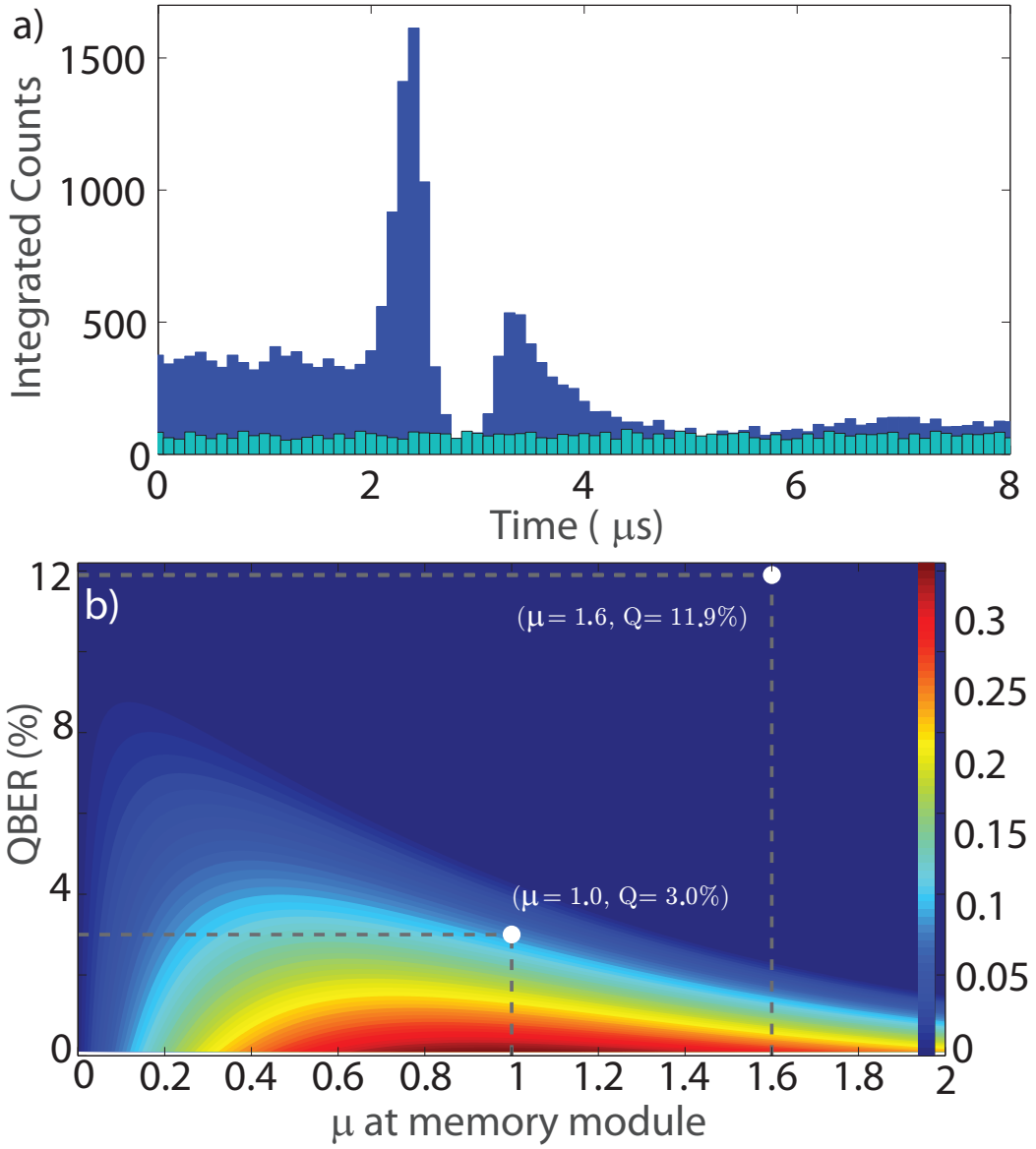

Figure 2.17: **Ultra-low-noise quantum memory operation**. a) Noise reduction by introducing an auxiliary field, the interaction between dark-state-polaritons creates a background free region. Retrieving the probe under these conditions results in an SBR >25. The signal for the SBR is a 100 ns integration region at the peak of the retrieved signal. The background is a minimized averaged background obtained in a 1 μs region centered around 5.2 us (divided by 10). The dark blue histogram includes signal, background and the auxiliary field. The light blue histogram only includes the auxiliary field. (b) Quantum key distribution rate vs. mean photon number and quantum bit error rate. Color bar represents the key rate. The line intersecting light blue and dark blue (negative key rate area) corresponds to the boundary for the positive key rate. The white dots indicate the regime of bare quantum memory and ultra-low-noise memory regimes.

2.7.3 Portability

Portable and robust quantum memories are paramount to have quantum networks become all-environment qubit connections between distant and isolated locations. In our last network experiment, we show the storage of single-photon level qubits in the first fully-portable plug-and-play memory. This prototype has the same features of the designs used in our experiments as mentioned above but is fully independent of laboratory infrastructure as it only requires the probe photons and an EIT control field as inputs. It also possesses a miniaturized version of the filtering system with independent temperature controllers. This device has already proven to be fully portable as it was built in Stony Brook University and shipped to the Royal Institute of Technology in Stockholm. There it has been shown to be fully operational and easily integrated with independent quantum light sources. These experimental results are published in [58]. A detailed depiction of the portable memory is shown in Fig. 2.18a. In Fig. 2.18b we show a storage-of-light experiment in which we store pulses with a mean photon number $\langle n \rangle \sim 2$, in a single-rail experiment, corresponding to an SBR of 7.2.

2.8 Conclusion

This chapter highlights the development of a previously rejection notion: having quantum memories operating at room temperature. The memories are probed using weak coherent states and characterized by polarization qubit fidelity measurements giving an average fidelity of $86.6 \pm 0.6\%$. In our network setup, this was improved to $> 90\%$. We also show shot-by-shot operation. Currently work is being done on interfering the outputs of two these memories and even more, progress has been made in making the memories portable. This development based on the results I've shown, positions the current infrastructure in front of many similar attempts in the quantum information community. [44, 48, 43].

In the offing, powerful quantum networks require quantum processing. Though we have pursued the development of processing and memory nodes in parallel, the rapid success of the memories as a primary node in a scalable network platform gives a firm footing for adding more capable nodes to the network. I will describe our quantum processing node program in the next few chapters.

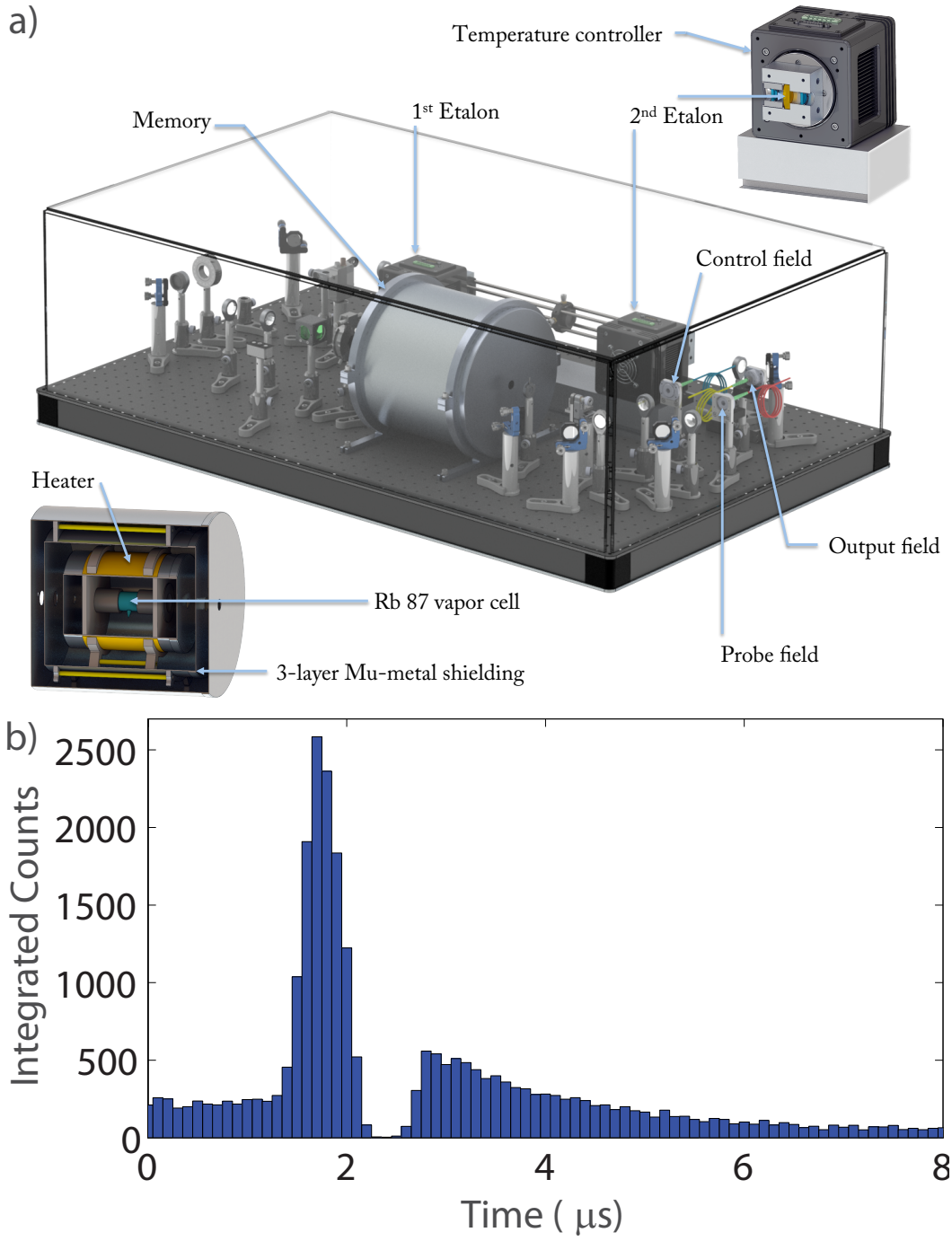

Figure 2.18: a) Prototype of a room temperature portable quantum memory. Upper-right inset: Detail of one of the frequency filtering units, including the silica etalon, isolation oven, temperature control cold-plate and PID temperature regulation circuitry. Bottom-left inset: Detail of the interaction zone including the Rb cell, temperature control electronics and three-layer magnetic shielding. b) Storage of single-photon level light pulses in the portable quantum memory.

Chapter 3

Quantum process tomography of an Optically Controlled Kerr Non-linearity

3.1 Introduction

As mentioned in the introduction, an optical quantum network would consist of many other nodes than the memories described in Chapter 1. One class of nodes that are being investigated on the path to create interactions between qubits are optically controlled non-linear devices [59, 60, 61]. In the same room-temperature ensemble of atoms used for the quantum memories, we characterized an optically controlled nonlinearity. The characterization was done using the same laser setup, by adding one more phase-lock system.

In keeping with our goal with reducing the technical overhead of quantum network experiments, we use a tomography technique that uses laser pulses to do a full quantum characterization of the quantum process. It is called coherent state quantum process tomography (csQPT) [62, 63, 64]. This technique has already been used to characterize ensemble memories [64] that are similar the ones in our network.

Since much of the complexity of characterization is moved from hardware — quantum light sources and specialty detectors — to software — maximum-likelihood algorithms and superoperator matrices — extending it's capabilities to multi-mode characterization seems more tractable. **Disclaimer:** This chapter contains work included in the papers Kupchak, C., Rind, S., Jordaan, B. and Figueroa, E. Quantum Process Tomography of an Optically-Controlled Kerr Non-linearity Scientific Reports 5, 16581, 2015. *I contributed to the im-*

plementation and modeling of the experiment, the interpretation of the results and the writing of the manuscript. Permission from the other authors was received to include the results in this thesis.

3.2 Processing platforms and evaluation

The success of deterministic, multi-field gates is contingent on two stringent conditions: the first is achieving a large cross-talk between quantum-level fields [65]. The second is the generation of relative non-linear phase operations that can act on either discrete qubit variables or continuous quadrature modes [66]. Different avenues are currently being pursued to overcome the first obstacle. One is the use of highly excited Rydberg states, that have demonstrated the promise for creating a sizeable non-linear medium for individual photons to propagate and interact [67, 68]. Another is the use of strong light-matter interaction, as provided by cavity quantum electrodynamics (cQED)[27, 36, 69, 70, 71].

Addressing the second condition remains a challenge, yet is key to building truly functional quantum logic gates. Previously, electromagnetically-induced transparency (EIT) enhanced Kerr non-linearities utilizing atomic four-level schemes [72, 73] have been used to realize small phase shifts for few-photon level classical fields using atomic ensembles [74, 75, 76, 77]. Although fundamental questions concerning how the non-instantaneous behavior of such Kerr non-linearities preclude the creation of overall cross-phase modulation phase-shifts persist [78, 79].

Therefore, the availability of evaluation tools that allow the direct characterization of these deterministic phase-shift operations so one can know *a priori* its function regarding specific quantum optical states inputs would be indispensable. Accomplishing such a task in a tractable manner could be attained with relatively simple technological methods, namely EIT non-linearities in room temperature atomic vapor [80, 81, 82, 83, 84] in combination with full quantum optical characterization via coherent state quantum process tomography (csQPT) [62, 64].

We start with a three-level, Lambda atomic EIT scheme composed of two hyperfine grounds states that couple to a common excited state by a weak probe field and a high power control field. The N-type system is completed by a third, signal field that couples one of the original Lambda ground states to a separate excited state (see Fig. 3.1 a). This signal field induces a cross-phase modulation on the probe giving rise to a relative optical phase shift between the fields [85, 73]. When only the control field is present, the probe pulse

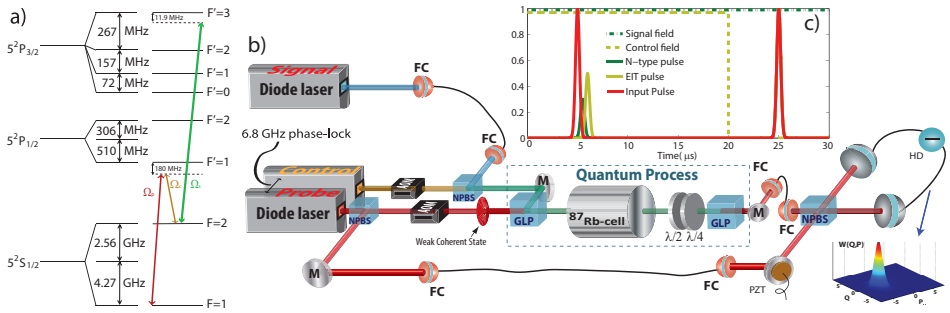

Figure 3.1: **Atomic level scheme and experimental setup.** (a) Atomic level diagram for the N-type scheme in ^{87}Rb. (b) Experimental setup for quantum process tomography of a Kerr non-linearity using rubidium vapor. AOM: Acousto-optical modulators; GLP: Glan-Laser-Polarizer; NBPS: Non-polarizing beam splitter; HD: Homodyne detector; PZT: Piezoelectric device; M: Mirror. Probe and local oscillator: red beam paths; Control: yellow beam path; Signal: blue beam path. (c) Pulse scheme for determining the relative phase shift experienced by the probe pulses (red solid line) under EIT slowdown (yellow solid line) and N-type conditions (green solid line).Reproduced from [25]

sees a characteristic EIT transparency (see Fig. 3.2b, green line) causing it to experience both slowdown conditions and an optical phase shift. The presence of a mode-matched signal field can then negate this EIT effect (see Fig. 3.2b, light blue line). Furthermore, the phase shift undergone by the probe pulse can be controllably reduced by applying a particular power of the continuous wave signal field, as changes in transmission correspond to strong dispersion modifications in the atomic medium.

We probe our system with weak coherent states and measure the phase and amplitude quadratures of the input and output via time domain homodyne tomography allowing us to perform quantum state reconstruction and directly compare the corresponding density matrices. Further, by collecting the output data for a sufficient set of weak coherent state inputs, we gain the information needed to characterize the phase shift process by csQPT completely. The resulting process reconstruction yields a rank-4 process super-operator in the Fock states basis which can then be utilized to find out how our phase shift process will behave on arbitrary quantum optical states, either with discrete variables in the Fock basis on in the continuous variable regime.

We now turn our attention to characterizing the Kerr-based optical phase shift process through means of coherent state quantum process tomography (csQPT) [62]. This is a procedure akin to a "blackbox" problem but in the quantum domain, i.e., given any arbitrary but known quantum state $\hat{\rho}$ we can predict $\hat{\mathcal{E}}(\hat{\rho}_i)$, where $\hat{\mathcal{E}}$ represents our process. Quantum process tomography

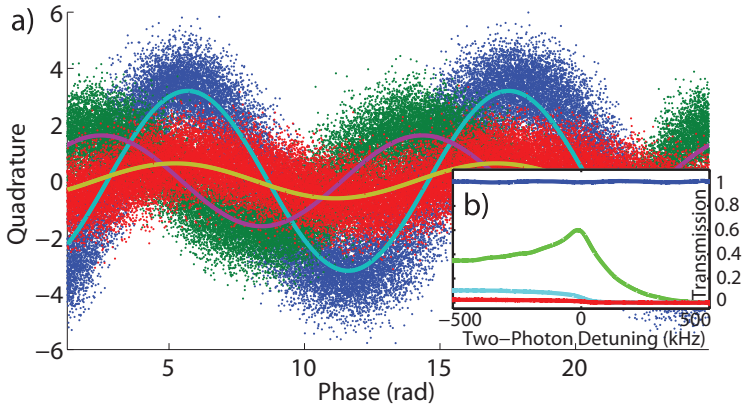

Figure 3.2: **Homodyne tomography of Kerr-induced optical phase shift.** (a) Input coherent state (blue dots), phase shifted state under EIT conditions (green dots), state under N-type conditions (red dots) as measured by the homodyne detector, together with their respective fittings for the phase information (solid lines). Note that each dot represents the time integration of a single pulse. (b) Frequency response of the system for the input (blue line), EIT conditions (green line) and N-type configuration with 0.5 mW signal power (light blue line) and 2.1 mW signal power (red line). Reproduced from [25]

is derived from the fact that all quantum processes are linear in the space of density matrices in the Hilbert space defining the process. More specifically, the technique of csQPT uses coherent states from a common laser source to produce a set of "probe" states spanning the Hilbert space where our process will be characterized. Therefore, by subjecting an ample number of coherent states $|\alpha_i\rangle\langle\alpha_i|$ to our optically controlled phase shift and recording the corresponding output $\hat{\mathcal{E}}(|\alpha_i\rangle\langle\alpha_i|)$, we are provided with the needed information to completely characterize our process for a finite region in a relatively simple and robust manner. For the primary Lambda system, we utilize two external cavity diode lasers phase-locked at 6.8 GHz to correspond to the ^{87}Rb ground state splitting. The probe field is situated 180 MHz red detuned from the $|5S_{1/2}, F = 1\rangle \leftrightarrow |5P_{1/2}, F = 1\rangle$ transition with the control field set to the $|5S_{1/2}, F = 2\rangle \leftrightarrow |5P_{1/2}, F = 1\rangle$ transition; both lasers are at a wavelength of 795 nm. Lastly, for the signal field we have an additional, third diode laser set to the $|5S_{1/2}, F = 2\rangle \leftrightarrow |5P_{3/2}, F = 3\rangle$ transition at 780 nm (Fig 3.1a). In our measurements, the signal field is red-detuned by 11.9 MHz.

Furthermore, the control and signal field are fixed to have the same linear polarization with the probe field set to the orthogonal polarization to allow for convenient separation of the fields after the atomic interaction. All light

fields are also spatially mode matched to a waist of $\omega_0 \approx 200\mu m$ in a single-rail configuration (see Fig. 3.1 b). In the pulsed regime, the intensity of the probe and control fields are temporally modulated using acousto-optical modulators (AOM). For our medium we use a 7.5 cm long glass cell with anti-reflection coated windows containing isotopically pure ^{87}Rb with 10 Torr of Ne buffer gas kept at a temperature of 336 K. The cell is pumped with a 1.75 mW control field for 25 μs before a probe pulse of 1 μs temporal duration is coupled into the vapor. After 30 μs, the control field is shut off and a second probe pulse is sent through the vapor cell to serve as a reference (see Inset of Fig.3.1 c). The repetition rate of the entire experiment was 25 kHz.

The magnitude of this phase shift is quantified using time domain homodyne tomography [86]. To do so, we couple both the probe mode after atomic interaction and a strong local oscillator (LO, coming from the same laser) to fibers and interfere them. Before interference, the local oscillator is reflected off a mirror attached to a piezoelectric device to permit control of the phase and allow total tomographic reconstruction (see Fig.3.1). To quantify the temporal envelope of our weak probe pulses, we first recorded the intensity of bright classical pulses undergoing the different measurement conditions on an auxiliary photodetector (not shown, see pulses in Fig.3.1 c). From this data, the shape and length of the probe's electric field envelope were calculated. A weighted integration over the homodyne signal using the electric field envelope for a given pulse then yields its time-averaged quadrature value. For all input pulses, those subjected to EIT slowdown and the N-type conditions, we acquired 50 000 balanced homodyne values in the time domain by an oscilloscope dual triggered to the pulse start point and piezo scan. The optical phase shift experienced by the probe pulses under EIT and N-type conditions can then be directly quantified by fitting this quadrature measurement data (see Fig. 3.2 a). The second probe pulse sent after the control field is shut off serves to determine the baseline phase of the interferometer from which the phase induced to the initial pulse can then be calculated. This data is then entered into a maximum-likelihood algorithm in order to generate the quantum state (see Fig. 3.3) or to perform quantum process reconstruction in the Fock basis (see Fig. 3.4).

The phase shift undergone by a single state when subjected to EIT conditions can be understood through direct visualization of the state's Wigner function in phase space. The Wigner function can be found by first entering the measured phase and quadrature data into a maximum-likelihood algorithm to obtain the state's density matrix [87] followed by direct calculation of the experimental Wigner function [88]. The information granted by these types of measurements can extend on previous studies [73, 75, 76] as we now attain

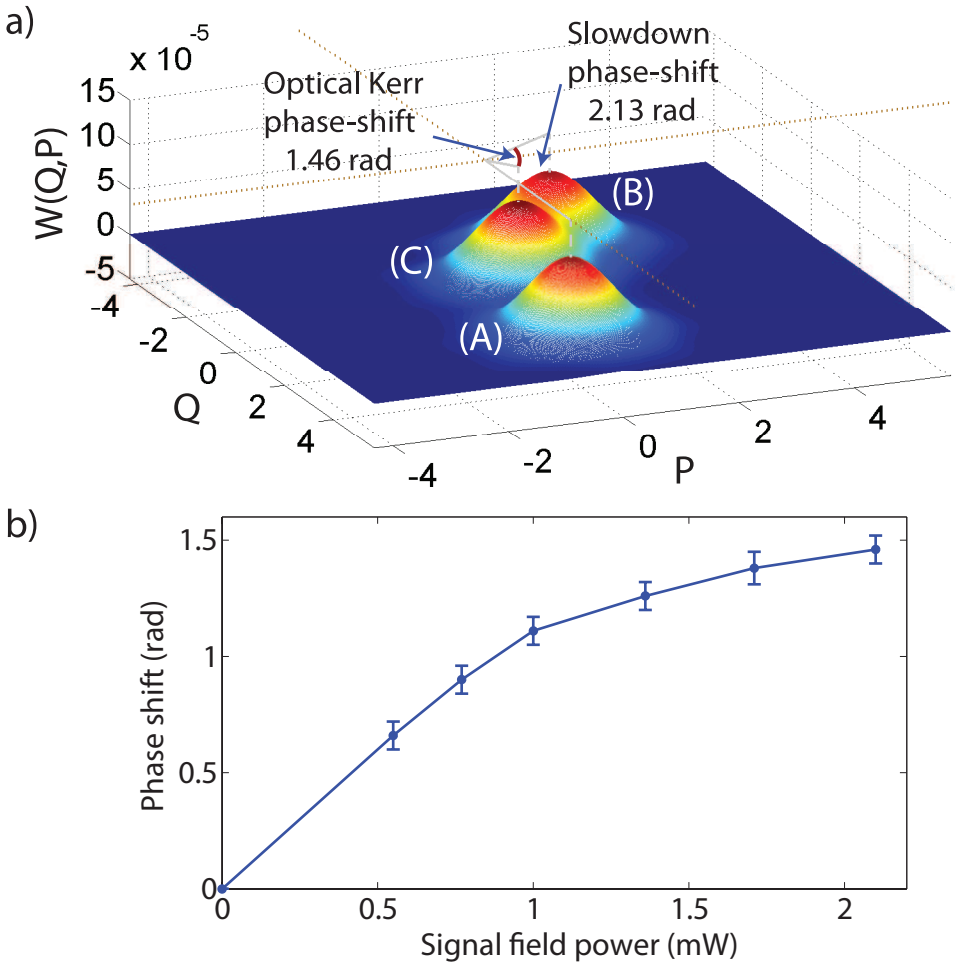

Figure 3.3: **Wigner function reconstruction of coherent states under EIT and N-type conditions.** (a) Wigner function reconstruction of the original input state (A), Wigner function reconstruction of the phase shifted state under EIT conditions (B) and Wigner function reconstruction of the N-type modified state using a 2.1 mW signal field (C). (b) Relative phase shift between the EIT and N-type conditions controlled optically as a function of the signal field power. The solid blue line is a guide to the eye. Error bars are statistical. Reproduced from [25]

the full density matrices of the output, which can be compared directly to that of the input. As an example, for input coherent state containing a mean photon number of $\langle n \rangle = 5.4$ ((A) in Fig. 3.3a), we measure a phase shift of $\Delta\theta_{EIT} = 2.13 \pm 0.04$ rads when subjected to EIT slowdown ((B) in Fig. 3.3a). Moreover, we measure the decrease of this phase shift in the N-type scheme when a 2.1 mW signal field is present ((C) in Fig.3.3a).

In this case, the phase shift with respect to the input is found to be $\Delta\theta_{N-type} = 0.67 \pm 0.04$ rads. Hence, the optically induced phase difference between the two schemes is $\Delta\theta_{N-type} - \Delta\theta_{EIT} = 1.46 \pm 0.06$ rads. From this analysis, we can also find the mean quadrature variance $\bar{\sigma^2}$ of the input and output states. In this case, the variance values corresponding to the input, slowdown and N-type schemes were found to be $0.517 \pm 0.004, 0.562 \pm 0.008, 0.517 \pm 0.004$ respectively. We can see increased deviations from an ideal coherent state for the reconstructed slowdown state [63] which are lessened under the N-type conditions as a result of the losses. Note that due to the losses experienced by the probe in our EIT schemes, the phase shifted Wigner functions are now situated closer to the phase space origin than the original input state. Here, the transmissions of the EIT and N-type schemes averaged 25% and 3.5% respectively. The non-linearity of our Kerr-based optical phase shift is demonstrated in Fig. 3.3 b which shows the measured phase shift versus the signal field power.

To accomplish csQPT experimentally, we measured the output states of both the EIT slowdown and N-type processes along with their corresponding inputs for 13 different coherent states with input amplitudes α_i ranging from 0 to 3.3. This was done for six different signal field powers each serving as their separate characterization. Hence, the temporal modes for every set of conditions were independently measured to account for the group velocity experienced by the probe at a particular signal field power. These temporal modes are shown in Fig. 3.4a. Note that the parameters used to achieve our base EIT slowdown conditions remained constant at all times.

The data obtained through homodyne detection was binned into 40 phase and 40 quadrature bins to encompass the entire range of the coherent state measurements. The binned data was then entered into a maximum-likelihood reconstruction algorithm in line with the procedures described in [64] to obtain the process super-operator. Our process was phase invariant, meaning that any fixed phase difference between two input states was preserved after the process and allowed a majority of the elements to be extinguished. With our data, we found 100 iterations of the maximum-likelihood algorithm to be adequate for our reconstruction to converge. This was followed by truncation of our process superoperator to a maximum photon number of $n = 5$. Note that the linear

losses not associated with the process (detector efficiencies, visibilities, etc.) experienced by the probe states were quantified and corrected for in the same manner as was done in prior studies [89]. All the information related to the atomic interaction remains in the tensor elements. Our process reconstruction provides a mapping of the input density matrix elements to the resulting output elements holding both the phase and photon number information. While the on-diagonal elements $\mathcal{E}_{kk}^{mm}$ exhibiting the photon number information have been shown in prior studies [62, 63, 89], the off-diagonal elements holding the phase information have received less attention [90] but are of higher relevance in this study. This information can be extracted from the components relating to how the input density matrix space maps to a particular off-diagonal element of the output. The pertinent information can be visualized by taking specific slices of the process tensor, where for instance, the phase value for the ρ_{01}^{out} output density matrix element is related to the $Im\{\ln[\mathcal{E}_{01}^{mn}]\}$ process tensor elements. Fig. 3.4 b shows these tensor elements for different powers of the signal field where the height of the elements indicates the size of the phase shift relative to the original input state. In general, it is the summation over the product of these elements with their density matrix counterparts that yields the phase of the output element given by

$$\phi_{kl} = Im\left(\ln\left(\sum_{m,n}\mathcal{E}_{kl}^{mn}\rho_{mn}^{in}\right)\right). \tag{3.1}$$

As expected, the phase component is independent of the input amplitude α (see Fig. 3.4) over the subspace in which the process was characterized. The errors in the process tensor elements shown in Fig.3.4b are those of our experimental statistics and were found to be about ± 0.06 rads in all measurements. Other errors include the statistical nature of our quadrature measurements and how they pertain to the quality of our process tensor reconstructions. To evaluate these effects, we simulated multiple datasets by random variation of the quadrature counts at a given phase within its standard deviation. We then reconstructed a set of simulated process tensors $\mathcal{E}_{sim,i}$ and calculated their fidelity $F(\mathcal{E}_{sim,i}, \mathcal{E})$ with respect to our original reconstruction $\mathcal{E}$ using the Jamiolkowski state representation [91]. We found these fidelities to be near unity with none of the tensor elements shown in Fig.3.4b deviating more than 0.5% of the original value.

The power of csQPT is the ability to make predictions about the process output, or specifically in our case, know *a priori* how our optical phase shift and losses modify input quantum optical states. To exemplify these capabilities, we acted the process tensor reconstructions corresponding to the weakest

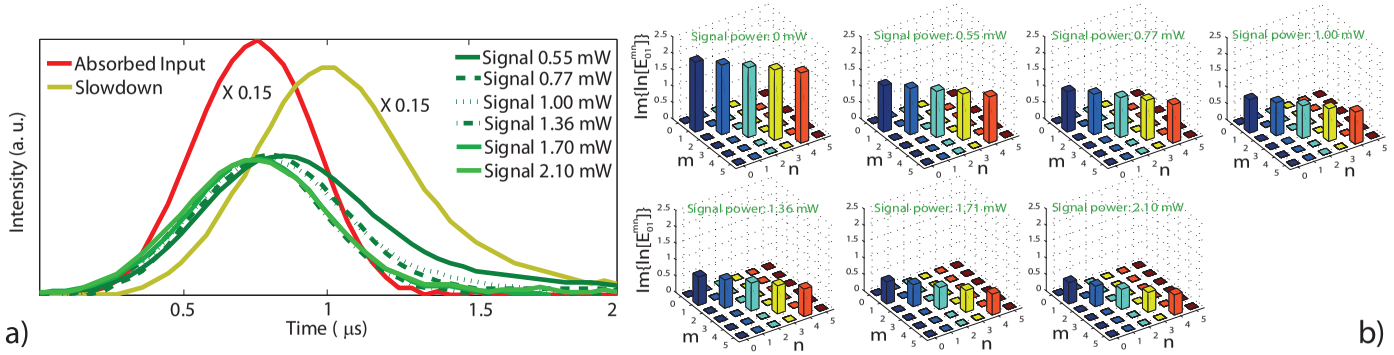

Figure 3.4: **Phase transforming elements of the reconstructed process superoperator.** (a) Slowdown pulses with the group velocity modified by different powers of the signal field and represent the temporal mode of the reconstruction. The signal field power ranges from 0.55 mW to 2.10 mW. (b) Plotted are the $Im\{\ln[\mathcal{E}_{01}^{mn}]\}$ elements for different powers of the signal field, where m and n represent the input indices in the Fock basis. Reproduced from [25]

signal field power of 0.55 mW on a quantum optical state in the form of a theoretical squeezed vacuum with +/− 4.3 dB of anti-squeezing and squeezing. For the EIT slowdown, we found the predicted output state exhibited $\sigma_-^2 = -0.83 \pm 0.04$ dB and $\sigma_+^2 = 2.47 \pm 0.04$ dB in the squeezed and anti-squeezed quadratures respectively with a phase shift of $\Delta\theta_{EIT} = 2.12 \pm 0.03$ rads compared to the input. Likewise for the N-type scheme, our prediction yielded values of $\sigma_-^2 = -0.15 \pm 0.06$ dB, $\sigma_+^2 = 0.43 \pm 0.06$ dB and a phase shift of $\Delta\theta_{N-type} = 1.48 \pm 0.03$ rads. Full information relating the output state predictions to our reconstructed superoperator is shown in Fig. 3.5. Finally, note that our experimental gate characterization can be applied to any quantum phase gate architecture including those involving discrete variables. For instance, a characterized phase rotation of ϕ means that our process superoperator would act on a Fock state qubit such that $(|0\rangle+|1\rangle)/\sqrt{2} \rightarrow (|0\rangle+e^{i\phi}|1\rangle)/\sqrt{2}$, and hence, csQPT could be an effective tool to determine how qubit variables are modified, thus the benchmarking of quantum gate operations becomes a possibility.

In summary, we have characterized a Kerr non-linear process in the form of an optically controlled phase shift mediated by atoms at room temperature via the method of csQPT.Our study signifies the first time that such an optical gate operation, a key for creating quantum optical information processors, has been fully characterized quantum mechanically. These processes comprise a significant part of the more general set of operations involving multi-field interactions [92].

The csQPT technique is achieved with relatively simple optical measurements by probing our phase shift system with only a sufficient set of weak laser pulses and measuring the corresponding output. Further, we highlighted the potential for this method by using our process reconstruction to predict the effect of our phase shift on a squeezed vacuum state.

3.3 Conclusion

In this chapter, I presented how we characterized a 1.46 ± 0.06 rads optically controlled phase shift using csQPT. This was the first time the off-diagonal terms of the reconstructed superoperator from csQPT was used to characterize the phase-shift result, showing the impact of the quantum process on the coherence terms.

The simplicity and robustness or this characterization procedure would make it ideal for the facilitation of practical quantum optical gates into future networks and provide a universal tool for the characterization of multi-state

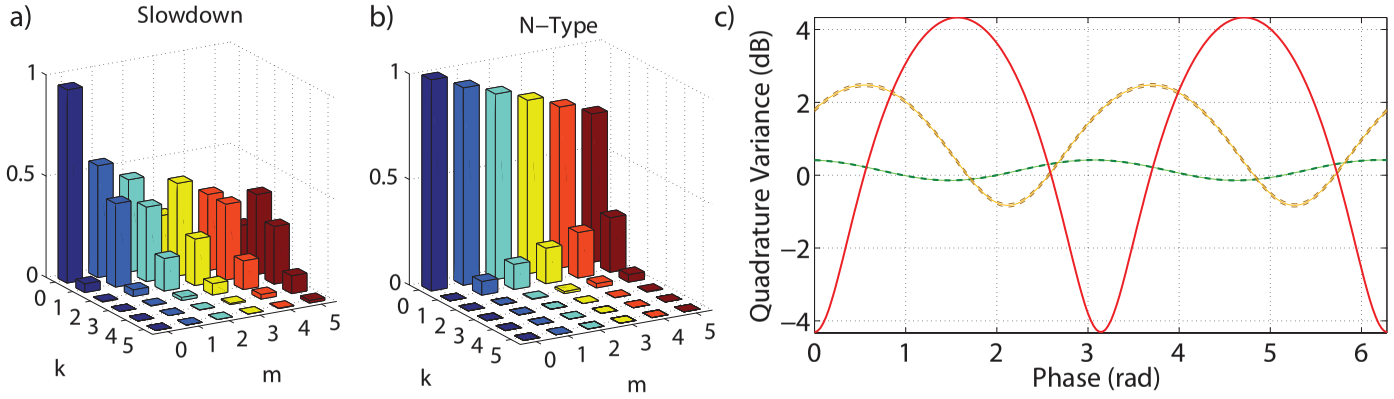

Figure 3.5: **Quantum process tensor predictions applied to squeezed light.** Full information about action of the process given by the on-diagonal tensor elements $\mathcal{E}_{kk}^{mm}$ which show the attenuation for the (a) Slowdown and (b) N-type cases. (c) Phase shift and quadrature noise information highlighted by the variance versus phase for the theoretical input (solid red line) and the predicted output for slowdown (yellow line) and N-type (green line) scheme with errors (dotted-lines). Reproduced from [25]

quantum components.

We are continuing the QPT research towards characterizing different candidate systems to generate optically controlled phase shifts [93] and multiple qubit nodes [90].

Finally, in the class of nonlinear optical systems, in addition to the EIT-based approach shown in this experiment, the use of optical cavities has been very successful [94, 28]. The overlap of these two approaches is what has motivated the construction of the double cavity node that will be discussed in the following chapters.

Chapter 4

Compact cross-cavity light-matter interface

4.1 Introduction and motivation

In the introduction, I mentioned how important it is for quantum networks to move towards multiple qubit processing. It is essential to get nodes that can handle more that one qubit in a *efficient* way.

For photonic networks, fully deterministic processing is still some years away, since combining strong photonic nonlinearities with high quantum fidelities and high efficiency lives on the limit of even the most advanced systems [28].

There is an in-between system where the probabilistic nature is limited and pushed to close to 1, such that it can scale with more than one node [95] and finding ways to herald inherently probabilistic systems to behave deterministically [26].

Strongly coupled systems provide an exciting opportunity for working with atoms and light reversibly. Both microfiber [71] or Cavity QED systems have made this experimentally feasible [2]. These systems have incredible experimental overhead and technical difficulty [96]. The adoption of these systems in future large networks can significantly be enhanced if this overhead can be simplified.

This scalability is what made us look at combining the ensemble physics that we use in our memories with cavity-light interaction.

By deconstructing the way cavities enhance interactions, one is led to strategies to extend their usability beyond the strong-coupling regime.

One starting point is the Purcell effect.

A way to understand the Purcell effect is to consider the momentum and energy states of photons as being in a continuum in free space. If one adds a cavity, a Q-factor that can be related to the finesse of the Fabry-Perot resonator emerges. The Q-factor is the ratio of stored energy to leaking energy.

Because of this, a cavity can effectively change the environment that the atomic medium inside the cavity sees. In strongly coupled regimes this becomes a reversible (non-Markovian) system in that the system has a memory of what happens between the light and the atoms. This occurs when the coupling rate between the cavity and the atomic medium is higher than the leakage rate. For a single atom in a cavity, this leads to the famous Jaynes-Cummings model.

The limiting case of this becomes very interesting when considering ensembles since the atoms have a connection to the environment through the cavity but also because of the neighboring atoms inside the cavity.

Many experiments have investigated a $\sqrt{N}$ scaling of ensemble systems. [97, 98]. The limits to which this gets influenced by the losses and when a full quantum mechanical treatment is needed to describe important behavior such as vacuum-Rabi splitting is still not completely understood [99].

Even if this regime only leads to an increase in the scattering through subsequent passes and thus higher OD, the other advantages of ensemble systems allow new technological advantages.

The use of three-level systems for collective enhancement of photon production [54] or in the use of EIT or related N-type schemes as discussed in the previous chapters, allow many different avenues to control the behavior of quantum states of light in these systems. One added level of control is how atomic cooling has developed in a very robust tool, but still, new cooling methods are still being developed [100].

Finally, the increasing interest in having more than one photonic mode coupled to a quantum system [101, 95] illustrate the extendibility this brings to previously existing technology. Exploring more than one connection to your node also deals with a new complexity of the problem. These engineering challenges still are very intertwined with the physics of the system. The right kind of compromises need to be made within the intermediate future, and we have developed ways to deal with these.

We coupled two Fabry Perot cavities to a cold atomic ensemble trapped in a Magneto-Optical Trap to address these questions. In this chapter, I will discuss the design, construction, and characterization of the integrated atomic and optical system.

4.2 Atomic medium: Cooling

The atomic medium of our experiment consists of laser-cooled atoms. This section briefly overviews laser cooling, and discusses our implementation of a cold atomic ensemble.

4.2.1 Theory

Laser cooling is the term commonly given to a set of techniques that use the radiative force of photons interacting with matter to slow down particles. The advent of the laser with light that was simultaneously intense and narrowband made this possible. Some of the first explorations of what we now call laser cooling involved an atomic beam directed at a laser detuned to the Doppler shifted energy levels[102]. As the atoms absorbed and emitted resonant light, the atoms would slow, and the Doppler shift would decrease. A spatially varying magnetic field along the path of the atom beam simultaneously Zeeman shifts the atoms, keeping them on resonance. This allowed the atoms to be cooled to approximately 60% of their initial temperature[102].

Optical Molasses is the term given for atoms that have been cooled using optical methods but have not been trapped[103]. Consider an atom in one dimension, experiencing the force of a laser beam. Due to the conservation of momentum, the atom will experience a recoil from absorbing a photon. The atom decays and emits a photon in a random direction and recoil with momentum opposite that of the emitted photon. Because of the randomness of the direction of emission, the net force over many absorption-emission cycles will be in the direction of the laser beam. When one has two equivalent counter-propagating beams, for a stationary atom, the net force would be zero.

However, when the atom moves in the direction of one of the beams the Doppler shift will cause the forces on the atom to be different.

In the rest frame of the atom, the light from the two counterpropagating beams will be Doppler-shifted - red detuned for the co-propagating beam, and blue detuned from the counter-propagating beam. If the laser frequencies are red-detuned from the rest frame atomic energy levels, the Doppler shift experienced by the atom will bring the counterpropagating beam *closer* to resonance, and the co-propagating beam *further* from resonance. Thus, photons from the counterpropagating beam will be absorbed more often, resulting in net force in the direction opposite its motion. The magnitude of the force experienced from the counterpropagating (F_+), and co-propagating,

(F_-): beams is [104]:

$$\vec{F}_{\pm} = \pm\frac{\hbar\vec{k}\gamma}{2}\frac{s_0}{1+s_0+\left[2\frac{(\delta\mp|\omega_D|)}{\gamma}\right]^2} \tag{4.1}$$

where s_0 is the saturation parameter for a given zero-detuning atom-light system: $s_0 \equiv 2\left(\frac{\Omega}{\gamma}\right)^2 = \frac{I\pi hc}{3\lambda^3\tau}$ and ω_D the Doppler shift, is simply $\vec{k}\cdot\vec{v}$[104]. Adding these two forces together, gives [104]:

$$\vec{F}_+ + \vec{F}_- = \vec{F}_{net} \approx \frac{8\hbar k^2\delta s_0\vec{v}}{\gamma\left[1+s_0+\left(\frac{2\delta}{\gamma}\right)^2\right]^2} \tag{4.2}$$

.

Expanding this model to three dimensions, the overall velocity of an atom or cloud of atoms can be significantly constrained. The temperature of a sample goes as the RMS kinetic energy of its motion:

$$T = \frac{mv_{RMS}^2}{3k_B} \tag{4.3}$$

Therefore, a significant constraint on the velocity of the atoms in a sample will constrain the temperature of the sample as well. In Eq. 4.2 it can be seen that the force experienced by the atoms is proportional to velocity, and can thus be considered a friction force. This explains the name of optical molasses, results in cooling, but is insufficient for trapping.

The first trap for neutral atoms was a hybrid 'magneto-optical' trap created in 1987 in the group of David Pritchard [105]. This trap combines the concept of optical molasses with that of the quadrupole magnetic field. Our quadrupole field is generated in a typical way using a pair of anti-Helmholtz coils to create a magnetic field with a zero-field point at the center, and a constant gradient near the zero point.

The Magneto-Optical Trap (MOT) Magneto-Optical Trap utilizes the Zeeman effect in a quadrupole potential to confine cold atoms. Optical molasses positioned at the center of the trap will experience no effect from the trap, as a magnetic field zero lies at the coil center however, atoms that drift away from the trap center experience increasing a magnetic field B, resulting in a Zeeman splitting of their magnetic sublevels. Atoms that drift into the positive $\vec{B}$ field region have their $m_F > 0$ levels shifted towards resonance with the σ^+ beam, while atoms that drift into a negative $\vec{B}$ field region have their $m_F < 0$ levels shifted towards resonance with the σ^- beam, as seen in Figure 4.1.

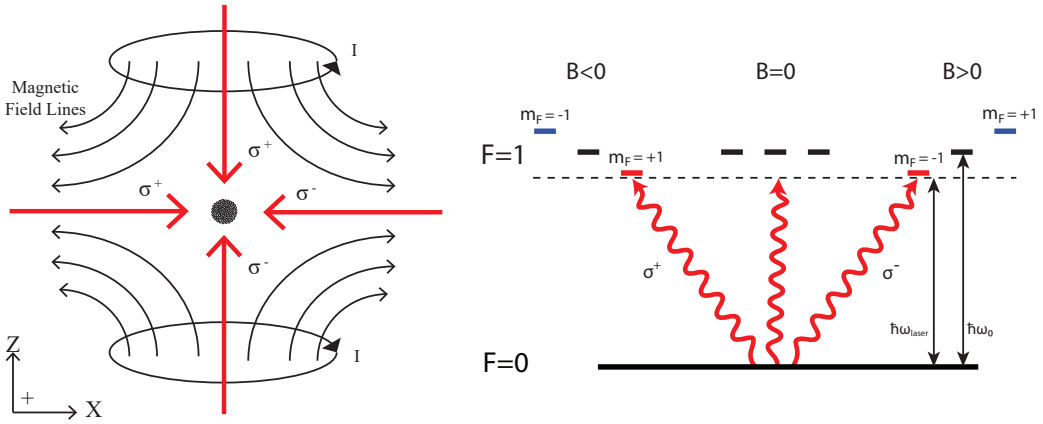

Figure 4.1: (a) A typical quadrupole magnetic field configuration using anti Helmholtz coils. The field in the positive z and negative x directions is negative, while the field in the negative z and positive x directions is positive.(b) A hypothetical F=0 $\rightarrow$ F'=1 transition and the associated light fields. Atoms in $B > 0$ regions see an increased radiative force from σ^- light, while atoms in $B < 0$ regions see an increased force from σ^+ light. Reproduces from [106]

The net scattering force on an atom in a magneto-optical trap is:

$$F^{\sigma^+}_{scatt}(\omega - kv - (\omega_0 + \beta z)) - F^{\sigma^-}_{scatt}(\omega + kv - (\omega_0 - \beta z)) \tag{4.4}$$

where $\beta z = \frac{g\mu_B}{\hbar}\frac{dB}{dz}z$ is the frequency shift of the atomic energy levels due to the external magnetic field at position z, with g the Lande g-factor and μ_B the Bohr magneton. One arrives at the new net force on an atom in a magneto-optical trap potential [104]:

$$F_{MOT} = -\alpha v - \frac{\alpha\beta}{k}z \tag{4.5}$$

This equation contains not only the frictional, velocity opposing force seen in the molasses, but a position dependent restoring force that is characteristic of a trapping potential.

4.2.2 Magneto Optical Trap Implementation

The implementation of the MOT had to consider the final design specifications allowing for two cavities, imaging, and EIT beams.

Custom modification of an existing commercial system was selected having the two optical cavities parallel to the flat sides of the vacuum cell. The

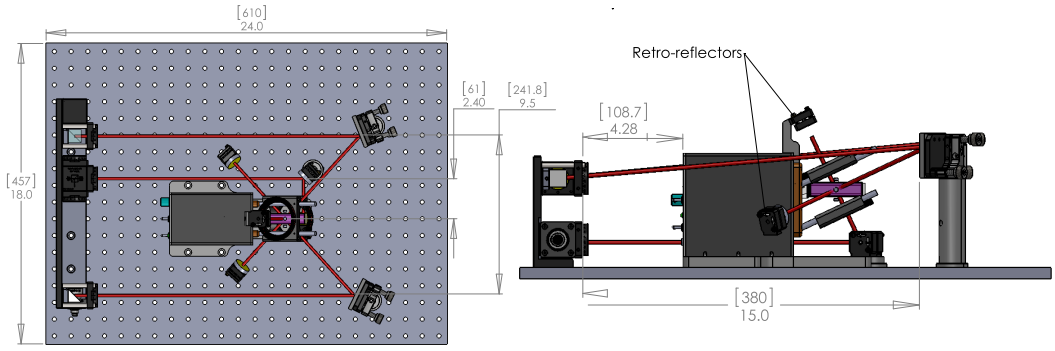

Figure 4.2: **MiniMOT schematics** Design schematics for the custom modification of the MiniMOT system implemented in the experiment. Of particular interest are the downward angled (approximately 27^o from the table), side cooling beams and the upward angled (approximately 63^o from the table) vertical cooling beam and magnetic coils. The vacuum system and rubidium dispenser lie in the large black box. Reproduced from ColdQuanta.

ColdQuanta MiniMOT system contains much of the optical setup necessary for a MOT, and the customizations to the original design include the rotation of the cooling and coil axes to leave the x and z-axes of the lab frame free for cavity placement.

Initial Cold Quanta Design and Modifications

The standard MiniMOT design involves a self-contained vacuum system - complete with vacuum cell, pressure monitor, rubidium dispenser circuit, anti-Helmholtz trapping coils, and an ion pump capable of reaching the low background pressures required of a magneto-optical trap. Additionally, the MiniMOT system includes all of the optics necessary to split the cooling light into three separate beams, circularly polarize it, and retroreflect it. The final result is three pairs of counterpropagating beams intersecting at a magnetic zero in a small, self-contained vacuum system containing Rubidium vapor - nearly all of the ingredients for a MOT.

The main difficulty is that the baseline model has a cooling beam directly on the z-axis in the laboratory frame, which was already reserved for one of the cavities that will be discussed later. As such, this beam and the anti-Helmholtz coils were rotated 27 degrees, leaving the z-axis clear for the vertical cavity. To compensate for this, it was required that the other two cooling beams be rotated 27 degrees below the XY plane to maintain the perpendicularity of the rays (see Figure 4.2). This rotation allowed for, in theory, clearance of

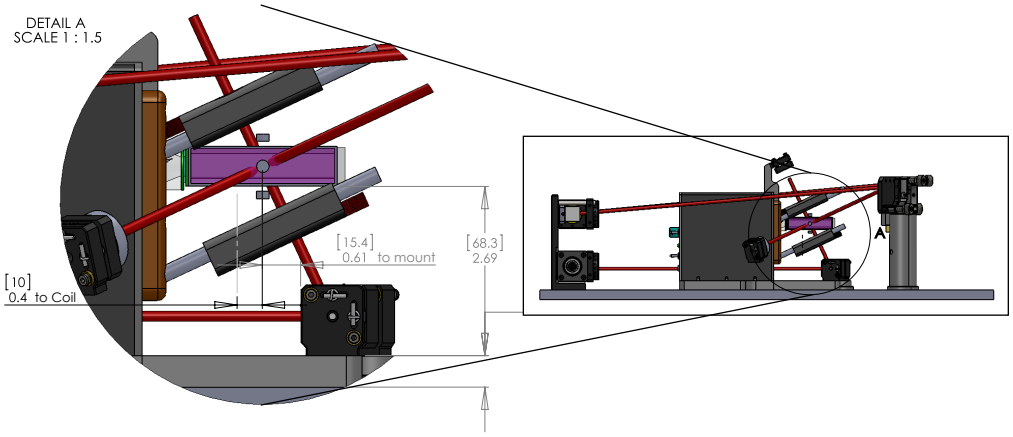

Figure 4.3: Design schematics for the custom modification of the MiniMOT system implemented in the experiment. Of particular interest are the downward angled (approximately 27^o from the table), side cooling beams and the upward angled (approximately 63^o from the table) vertical cooling beam and magnetic coils. The vacuum pump and rubidium dispenser lie in the large black box. Reproduced from [106] and ColdQuanta.

the beams through cavities of 20mm length, thus allowing a cloud of trapped atoms to exist while keeping the horizontal and vertical axes clear for cavities.

Laser beam path A fiber out-coupler composed of a collimating lens, and telescope results in an expected beam size of approximately 5mm, and a half waveplate allows control over ellipticity of the beam. Immediately after the waveplate is a pair of polarizing beam splitters (PBS), with another waveplate between them, followed by a mirror. Typical beam powers after splitting were as follows: 6mW in the vertical arm of the cooling beams, and 1.2mW in each of the other two. Immediately after the reflected portion of each beam is a quarter waveplate to change the polarization to σ^+ or σ^- as required by Figure 4.1.

Vacuum cell for atoms A rectangular cell of borosilicate glass with dimensions 16mm x 16mm x 65mm, coated with anti-reflective coating on both the inner and outer surfaces contains the atomic cloud. The anti-reflection coating was calibrated by ColdQuanta to be 0.042% at 0° incidence, 0.14% for 35° and 0.24% for 45°. A rubidium dispenser with natural isotope abundance, and an ion pump capable of reaching pressures of on the order of magnitude of 10^{-8} Torr are included in the black box, with a control panel for the ion

pump, dispenser, and magnetic coils on the back side.

Implemented Level Scheme As shown if Fig. 4.4 the cooling transition used is the cycling transition $5S_{1/2}|F = 2\rangle \rightarrow 5P_{3/2}|F' = 3\rangle$. We *red-detune* the laser 18MHz from this transition. The dipole-allowed off-resonant transition: $5S_{1/2}|F = 2\rangle \rightarrow 5P_{3/2}|F' = 2\rangle$, while rare, can occur. The excited state $F' = 2\rangle$ has a second decay pathway $5P_{3/2}|F' = 2 \rightarrow 5S_{1/2}|F = 1\rangle$ available to it. To counteract this loss from the cooling cycle, it is necessary to include a repumping beam that is tuned to the $5S_{1/2}|F = 1\rangle \rightarrow 5P_{3/2}|F' = 2\rangle$ transition. The atoms that are pumped into the excited state, $|F' = 2\rangle$ decay to the $|F = 2\rangle$ and $|F = 1\rangle$ states. Atoms that decay into the $F = 2$ state have reentered the cooling cycle, while atoms that decay into the $F = 1$ state will be excited by the laser once more.

Laser locking points For the implementation of this MOT system, two Toptica Tapered Amplifier Diode Lasers (TA-Pro) are tuned near resonance with Rubidium's D2 line. The first laser is locked using saturation spectroscopy (see section **??**) to a transition between two of Rubidium's hyperfine sublevels: $5S_{1/2}|F = 1\rangle \rightarrow 5P_{3/2}|F' = 2\rangle$. The second laser is locked using the OPLL discussed in section **??** the $5S_{1/2}|F = 2\rangle \rightarrow 5P_{3/2}|F' = 2\rangle$ transition, 6.834 GHz detuned from the the first laser.

Acousto-Optical Modulation

Acousto-Optical Modulators (AOMs) with Tellurium Dioxide crystals and a piezoelectric transducer attached to them are driven at radio frequencies to form a standing wave in the crystal, with different densities at the nodes and antinodes. Because these different densities have different indices of refraction, and therefore, different effective optical path lengths through the crystal, the standing-wave crystal essentially becomes a Bragg grating. The 1st order Bragg scattered beams experience a frequency shift precisely equal to the modulation frequency and is deflected by an angle $\theta = 2\theta_B = \frac{\lambda}{\Lambda}$ where angle θ_B is the Bragg scattering angle with λ and Λ is the optical and acoustic wavelengths respectively.

- AOM track 1 is setup in a zero-pass configuration on the $5S_{1/2}|F = 1\rangle \rightarrow 5P_{3/2}|F' = 2\rangle$ transition. This allows for pulsing of the repumper light.

- AOM track 2 shifts the laser frequency into 18MHz detuned from the $5S_{1/2}|F = 1\rangle \rightarrow 5P_{3/2}|F' = 3\rangle$ transition to form the cooling transition.

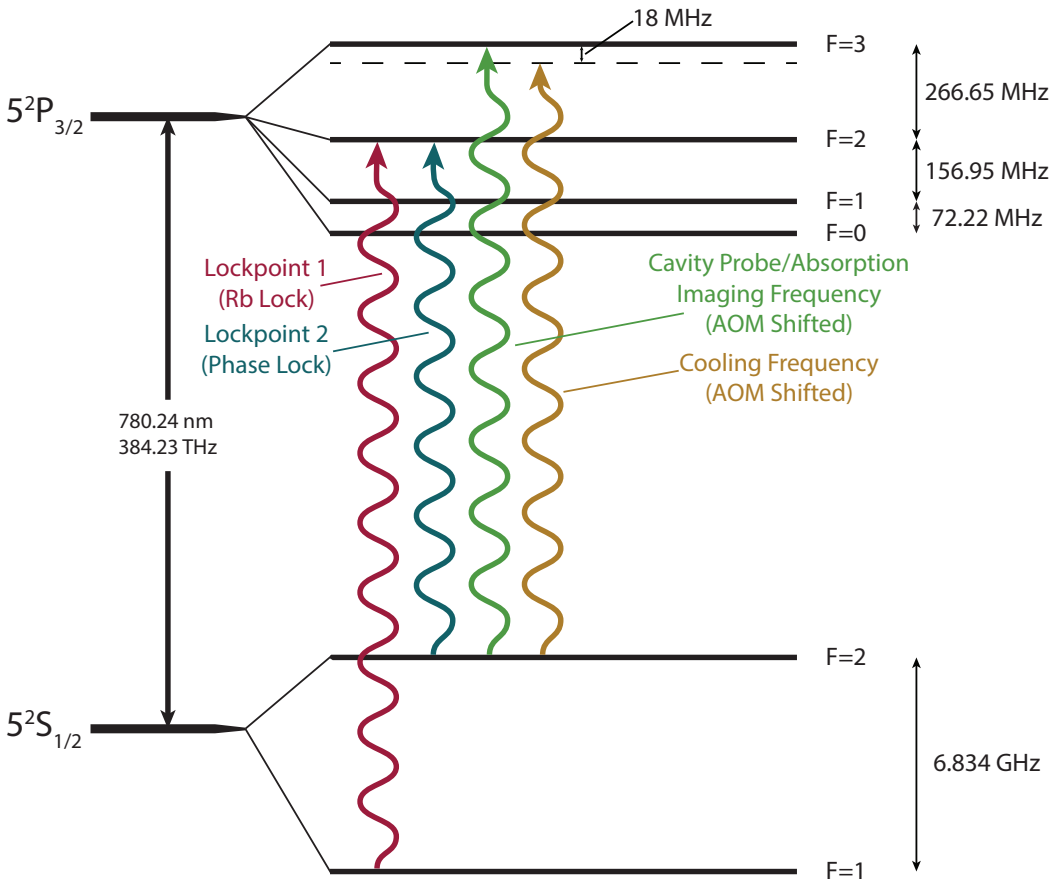

Figure 4.4: The fine (left) and hyperfine (right) sublevels of Rubidium, along with relevant laser fields and energy level structure carrying with it the selection rules $F' = F \pm 1$ or $F' = F$. (Data taken from [107]. Reproduced from [106]

On this track we installed a cats-eye setup to be used to cool more in later experiments.

- AOM track 3 shift again to the $5S_{1/2}|F = 1\rangle \rightarrow 5P_{3/2}|F' = 3\rangle$ transition for probing the cavity. We have used different detunings for this transition.

MOT Positional Engineering

An additional layer of complexity in creating the MOT had to be overcome from our specified implementation. To take full advantage of the commercial system, we limited ourselves in how many changes we made to the optical setup. The position of the MOT beams was decided based on predefined

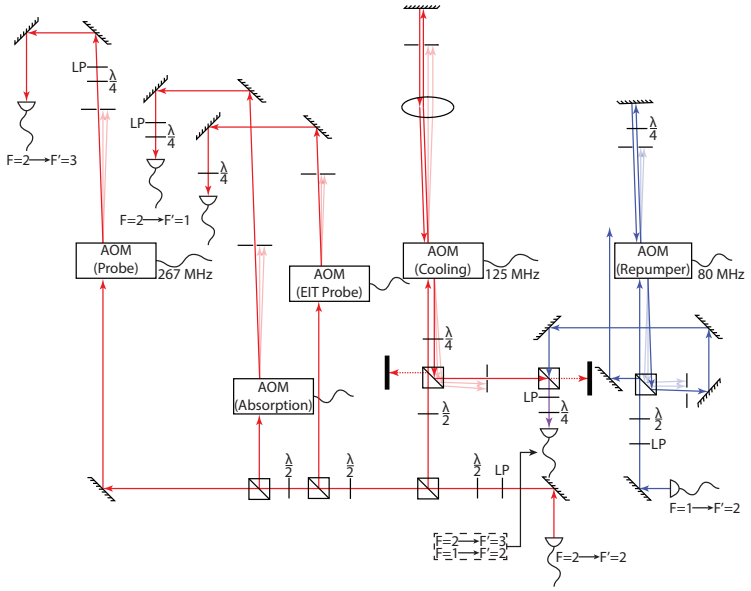

Figure 4.5: The AOM tracks used for the various frequency shifting of our light. From left to right: The probe track (far left), shifted 267 MHz, captures the first positive diffraction order, and is resonant to the $F = 2 \rightarrow F' = 3$ used for the cavity probe. The EIT probe light (center) is shifted to the same frequency, but won't be discussed further. The cooling light (center right) is shifted by 125 MHz, but 'double passed' to bring it 18 MHz red-detuned from the $F = 2 \rightarrow F' = 3$ line. Finally, the repumping light is modulated but not shifted, using a so-called 'zero-passing' technique, where it is negatively modulated on the first pass-through, and positively modulated on the second. Reproduced from [106]

measurements. However, the orientation of the optics to create this position is not aligned with the right-angled coordinate system defined by the table surface. After the initial MOT characterization, the positioning of the cavities required a stable MOT position within a comparable to the 50 μm waist of the cavity modes. The additional optics that were added for cavity control also let to more scattering than expected and the beam paths had to be changed to correct for this. The overlap region for the three beams close to the magnetic zero, was ill-defined, especially after a repair led the coils to be shifted from the original specifications. To probe this region of overlap systematically and later on to pseudo-deterministically change the position of the MOT as more optics were added, we created a procedure to characterize the beam paths and model it in CAD software.

1. *Measure the point on the beams.* We used a filter-holder and a printed alignment sheet to create a finer-grated measurement plane than the inch-separated holes in the optical table. Care was taken to screw this down as similarly each time as possible. The beams were shrunk by centering them on irises. The cross-sections of the different beams were taken at 2 to 3 points of each beam.

2. *Migrate the points to CAD* The coordinates obtained from step 1, were stored in text files. MATLAB script was used to create straight-line fits to the points. Two different SolidWorks scripts were written to import the coordinates and the fitted lines. Added dimensionality of the beams was done inside of SolidWorks.

3. *Simulate the intersection* The difference between intersecting and non-intersecting beams were found on the software, and the simulated beams close to the originals were produced. Coordinates were mapped off the 3D model.

4. *Movement of the mirrors* The relevant mirrors were moved in a "2-mirror walking" fashion to reproduce the desired coordinates.

Plots of the produced beams are shown in Figure 4.6.

MOT Characterization

Characterizations of the MOT were performed before the work described in this thesis. This section will serve only to summarize the findings of [108].

Absorption imaging was used to characterize the size and temperature of the MOT.

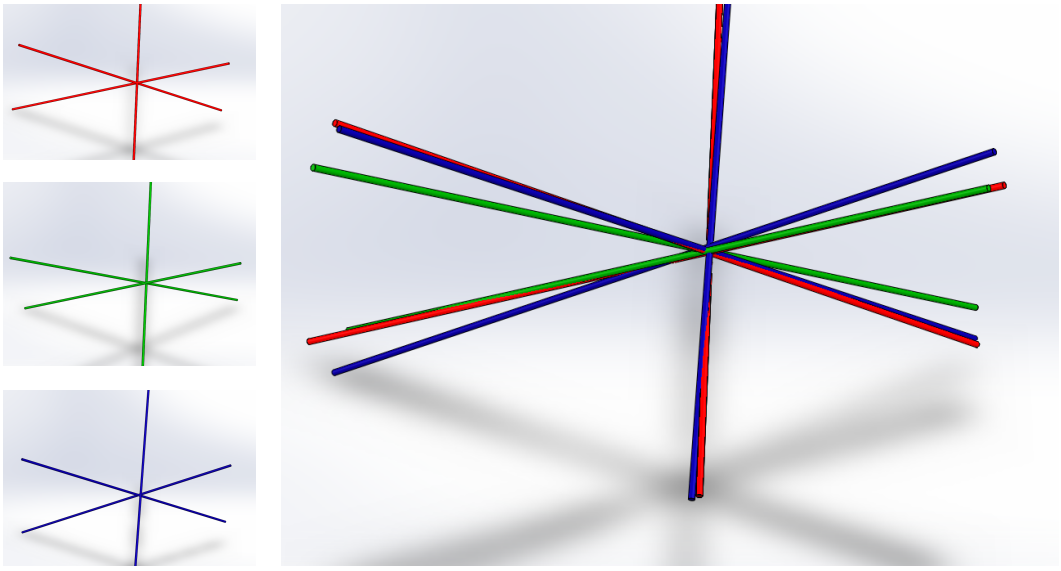

Figure 4.6: **Solidworks cooling beam configurations.** Several different beam configurations (left) that appear quite similar initially. When overlapped (right), non-negligible differences become apparent. These differences will lead to widely varying MOT size, shape, and position. While the intersection does not perfectly correspond to the MOT position because of the effect of the magnetic zero, within a small region, the agreement is strong. Outside of this region, there is a distinct correlation, but it becomes increasingly difficult to evaluate the change in position based solely on the beams. [106]

Theory To find the number of atoms in the cloud, one uses De Beers Law:

$$I = I_0 e^{-\sigma \bar{n}} \tag{4.6}$$

Where I_0 is the initial intensity, σ is a constant (the absorption cross section of Rb), and $\bar{n}$ is the integrated atomic density along the beam.

Furthermore, the temperature of the MOT can be measured using time of flight measurements. The expected size of a thermally expanding cloud should remain Gaussian with a temperature dependent waist: $\sigma(t) = \sqrt{\sigma_0^2 + \frac{kT}{m}t^2}$, the time dependent density can be given to be:

$$n(x_i, t) = \frac{1}{\sqrt{2\pi}\sqrt{\sigma_{x_i,0}^2 + \frac{k_B T_{x_i}}{m}t^2}} \exp\left[-\frac{x_i^2}{2\left(\sigma_{x_i,0}^2 + \frac{k_B T_{x_i}}{m}t^2\right)}\right] \tag{4.7}$$

Experiment If one splits a pair of absorption/non absorption images into pixels, subtracts the intensities on a per-pixel basis, applies De Beer's law to each, and solves for $\bar{n} = \frac{N}{A_{pix}}$, the number of atoms N becomes:

$$N = -\frac{A_{pix}}{\sigma} \sum_{i,j} \ln\left(\frac{\mathrm{Im}_{i,j}^{abs} - \mathrm{Im}_{i,j}^{bkg}}{\mathrm{Im}_{i,j}^{trans} - \mathrm{Im}_{i,j}^{bkg}}\right) \tag{4.8}$$

Where A_{pix} is the pixel area, $\mathrm{Im}_{i,j}$ corresponds to the camera grayscale intensity value for the i, j pixels, and abs, bkg, and trans correspond to the pictures with absorption (beam on, MOT on), background (beam off, MOT off), and transmitted (Beam on, MOT off) light profiles. This investigation concluded an atom number of between 13 and 20 million, increasing linearly with dispenser on-time. For a more thorough analysis of the MOT characterization see [108].

Naïvely assuming a constant density, the final cloud atomic density is found to be 4.5×10^{10} atoms/cm^3 and a cloud size of 200 pixels $\approx$ .75 mm. Therefore, a rough estimate of the number of atoms in a cavity mode of waist 50μm is $\approx 2.7 \times 10^5$, or approximately 270,000 atoms[108].

By pulsing the absorption beam directed at the MOT the moments immediately after the cooling fields have been switched off, it was possible to evaluate the temperature of the MOT. A Gaussian can be fit to the cloud distribution at each picture. This allowed the finding of a $\frac{1}{\sqrt{e}}$ cloud size. Fitting an exponential to these points results in a cloud temperature of 540 μK. Investigations were done using a CW absorption beam to determine the effect

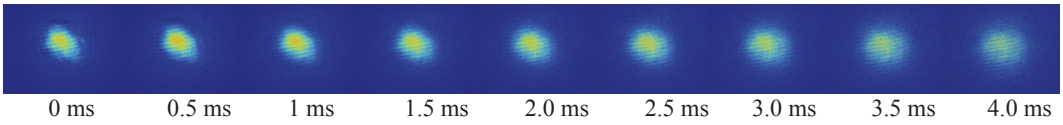

Figure 4.7: The first picture in this series was taken using absorption imaging with cooling, repumping and magnetic fields switched on. The subsequent images were taken with these three fields off at intervals of 500 μs with 30 μs absorption beam pulse duration and 16 μs camera exposure time. The absorption beam was tuned to the $F = 2 \rightarrow F' = 3$ transition of the Rubidium D1 line, the same frequency as the cavity probe (Green in Figure 4.4.)(Picture taken from [108])

of the absorption beam on heating the cloud, which arrived at a temperature of 3 mK for a continuous absorption beam, indicating a significant effect of the absorption beam on temperature.[108]

4.3 Optical Cavities

Starting with simple etalons [109] the optical resonator has had a central role in many optical experiments. Resonant round-trips of the electric fields create fields much stronger than outside the cavities. This allows the amplification of light-matter interaction and is well documented [110, 28, 2]. This tool allows for the control, interaction, and probing of both single atoms [95] or ensembles [111].

4.3.1 Theory

Following [109] the elementary mechanism of Fabry-Perot cavities is explained below. An etalon as in Fig. 4.8 have internal reflections of successive waves that have the following amplitudes after focusing

$$E_{\text{refl}} = r_1 + t_1^2 r_2 \exp(i\psi) + t_1^2 r_1 r_2 \exp(2i\psi) + ... \tag{4.9}$$

$$E_{\text{trans}} = t_1 t_2 + t_1 t_2 r_1 r_2 \exp(i\psi) + t_1 t_2 (r_1 r_2)^2 \exp(2i\psi) + ... \tag{4.10}$$

Since this is a geometric series we can find the infinite sum

$$E_{\text{refl}}(\delta) = \frac{[1 - \exp i\delta(r_1 r_2 + t_1 t_2)]r_1}{1 - r_1 r_2 \exp(i\delta)} \tag{4.11}$$

$$E_{\text{trans}}(\delta) = \frac{t_1 t_2}{1 - r1r2 \exp(i\delta)} \tag{4.12}$$

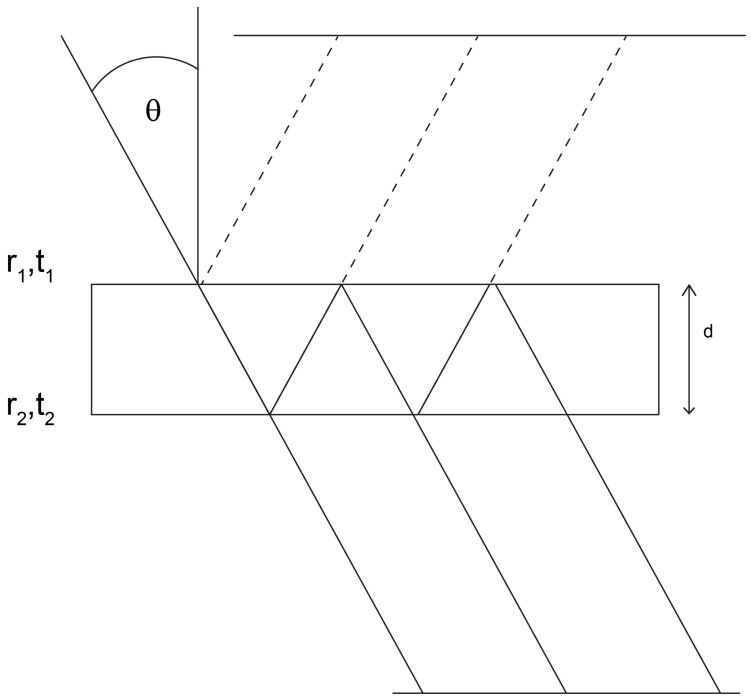

Figure 4.8: For a Fabry Perot cavity with mirror interfaces seperated by d distance and reflectivities and tranmissions r_i, t_i. The reflections inside the resonator is shown for a incident beam at an angle of θ. The planes that are shown correspond to where lenses are needed to interfere the emmisions. Redrawn from [109]

where $\delta = \Psi + 2\chi$ with $\Psi = 2\pi\nu t\cos(\theta)$ and χ is the phase shift from reflecting off the sides. With $R = r_1 r_2$, $T = t_1 t_2$ we have

$$I_{\text{refl}}(\delta) = \frac{r_1^2[1 - 2(R+T)\cos(\delta) + (R+T)^2]}{1 + R^2 - 2R\cos(\delta)} \tag{4.13}$$

$$I_{\text{trans}}(\delta) = \frac{T^2}{1 + R^2 - 2R\cos(\delta)} \tag{4.14}$$

Some equivalent formulations for transmissions with $A = 1 - T - R$ is

$$I_{\text{trans}}(\delta) = \frac{[1 - \frac{A}{1-R}]^2(1-R)^2}{1 + R^2 - 2R\cos(\delta)} \tag{4.15}$$

$$I_{\text{trans}}(\delta) = [1 - \frac{A}{1-R}]^2 \frac{1-R}{1+R}\left(1 + 2\sum_{m=1}^{m=\infty} R^m\cos(m\delta)\right) \tag{4.16}$$

$$I_{\text{trans}}(\delta) = [1 - \frac{A}{1-R}]^2 \frac{1}{1 + \frac{4R\sin^2(\delta/2)}{(1-R)^2}} \tag{4.17}$$

$$I_{\text{trans}}(\delta) = [1 - \frac{A}{1-R}]^2 \frac{1-R}{1+R}\sum_{n=1}^{n=\infty}\left(\frac{2\ln(R^{-1})}{[\ln(R^{-1})]^2 + (\delta - 2\pi n)^2}\right) \tag{4.18}$$

where 5.19 gives the typical picture of a series of repeating Lorentzian curves. The two different linewidths to consider $a^* = \frac{1}{2\pi} 2\arcsin(\frac{1-R}{2\sqrt{(2)}})$ and $l^* = \frac{1}{2\pi}\ln(R^{-1})$ are related by the following relation $sin(\pi a^*) = sinh(\pi l^*)$ which become equal as $R \to 1$.

We take the cavity linewidth to be $\kappa = 2\pi * l^*$ in this limit.

These define important cavity parameters: **FSR** The difference between 2 subsequent peaks

$$FSR = \frac{c}{2L} \tag{4.19}$$

Finesse

$$\mathcal{F} = \frac{1}{2a^*} = \frac{\text{FSR}}{\kappa} \approx \frac{\pi\sqrt{R}}{(1-R)} \tag{4.20}$$

In practical setups, Gaussian beam cavities are used. The ABCD-matrix of the optical elements determines the resonant condition for a general cavity. For linear cavities and Gaussian beams, this reduces to requirements of matching the Gaussian beam radius of curvature and spot size at the mirrors.

This is formally done using the g-factors:

$$0 \leq g_1 g_2 \leq 1 \tag{4.21}$$

where

$$g_1 = 1 - \frac{R_1}{L}, g_2 = 1 - \frac{R_2}{L} \tag{4.22}$$

with R_1, R_2 are the two mirror radius of curvature and L is the cavity length.

4.3.2 Mirrors and mode volume

The reflectivity of the mirrors is 0.99995 and 0.99 respectively. These give an expected Finesse of 312. The radii of curvature are 20mm for the horizontal cavities and 30mm for the vertical cavity.

After different design considerations [106], the cavities were decided to be configured in a confocal design. This corresponds to a $g_1 = g_2 = 0$. As discussed in more detail, this corresponds to the most stable configuration. Also, alignment allows for a degeneracy of modes.

4.3.3 Mirror holders, cavity holders, and piezos

The mirrors are held by a PEAK plastic holder that is machined to close to the dimensions of the cavity mirror. A press-fit was considered, but in the end, a small amount of glue or later on the cleaning polymer FirstContact was used to fix it to the mirror holder.

One side of each cavity has a piezo actuator. This requires the holder to consist of three segments. These segments were machined to have a little rim to guide the positioning of the smaller crystal to the plastic holder. This is to ensure flatness and better control.

The piezos are tubes that have electrode silver sputtered on the outside and inside surfaces. This configuration produces the field in a direction that provides a stronger contraction and extension in the z-direction, along with the length of the crystal. An important consideration of the piezo was the smaller but significant expansion and contraction of the piezo in the transverse plane. At some point, our design had restricted this movement and prevented accurate scanning of the piezo mode. Another important mounting consideration is to have the piezo move against a hard-edge for the piezo. Without a tight fit, the piezo moves both the mirrored side and the empty side, leading to smaller actuation.

Soldering the piezo system caused many difficulties as the temperature of the solder is an important consideration to avoid damaging the silver electrodes.

Only tiny amounts of solder could be used to avoid light from scattering of the solder inside. Excess amounts of soldering could also interfere with the mounting of the cavities.

The cavity holders are illustrated in Fig.4.9 and Fig.4.9 . The tuning-fork design is a result of having the vacuum cell between the mirrors. These are mounted on 3D translation stages with 10mm travel and 50μm micrometer increments.

We mount the horizontal cavity by slipping it underneath the vacuum cell in a U-movement and resting it on the bottom coil mounts. Then the holder was rotated up to put in the furthest mirror. After it is rotated to a position closer to its final position, it is connected to the translation stage. The final angle was determined in conjunction with the final positions of the translation stage.

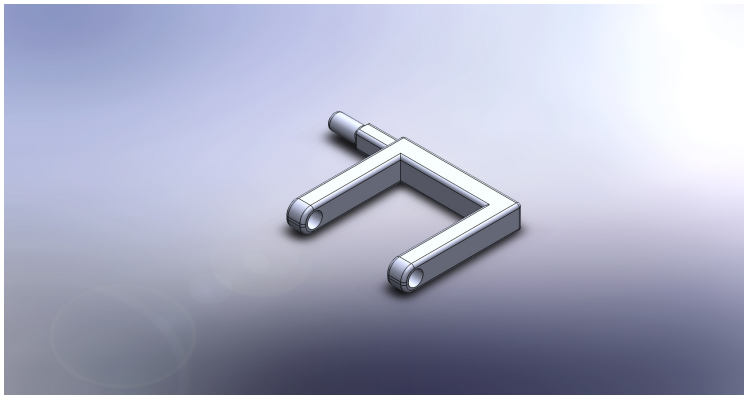

Figure 4.9: CAD drawing of the Horizontal Cavity Holder. Tuning fork design to fit around the vacuum cell. Some material that has been removed around the corners and arms is not shown in the drawing. Connected to a 3D translation stage in setup.

Mounting the vertical requires strict considerations of the position of the horizontal as there is a hole in the holder for the light to escape through, as shown in Fig. 4.10 .

4.3.4 Ex-situ setup

We characterized the two cavities in ex situ setups before moving the optics into the MOT setup. For the horizontal, this corresponded with an initial characterization of different mirror reflectivity. However, for the vertical, this was essential to ensure the correct alignment when more control over the beam paths could be executed. After this alignment, the vertical holders were glued,

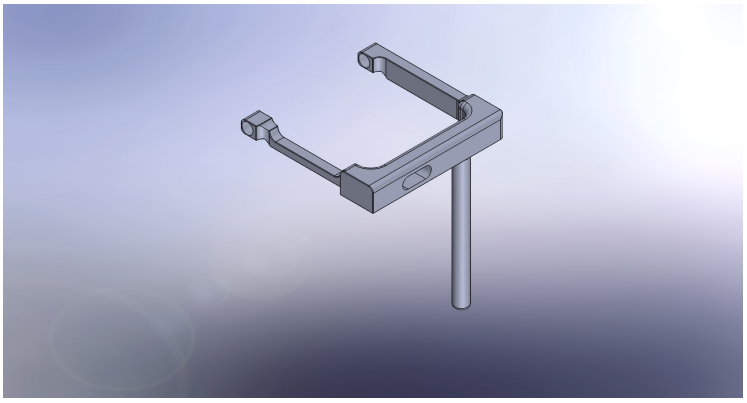

Figure 4.10: CAD drawing of the vertical cavity holder. Tuning fork design to fit around the vacuum cell. Key design elements are the hole in the side for horizontal light to be transmitted.Connected to a 3D translation stage in setup.

which allowed for the vertical modes to be conserved during the in-situ characterization.

4.3.5 Modulation for characterization

We characterize the cavities using phase modulation of the cavity probe laser.

$$\begin{aligned} E_{\text{probe}}(\omega) &= E\cos(\omega t) \\ E_{\text{mod}} &= E_{\text{probe}}(\omega + cos(\omega_m t)) \\ &= E\cos(\omega t + A_m cos(\omega_m t)) \\ &= EJ_0(A_m)cos(\omega t) + J_1(A_m)cos((\omega+\omega_m)t) + J_1(A_m)cos((\omega-\omega_m)t)... \end{aligned} \tag{4.23}$$

were the last is a well-known Bessel-function expansion of FM modulation. The extra terms correspond to new resonances in the spectrum if $\omega_m > \kappa$. Typically the modulation amplitude A_m is chosen not to be big enough to significantly reduce the central peak or produce higher order peaks. An expansion of

4.3.6 Ex situ characterization

To do the horizontal characterization a modulation frequency of $\omega_m = 2\pi \times$ 400MHz was used. The resulting side-bands are shown in Fig. 4.13. By fitting the peaks of the modulation, one gets a linewidth of 65.14 MHz.

Due to a small actuation range of the cavity piezo at the time a full sweep of the FSR couldn't be made. The FSR was measured using different locking

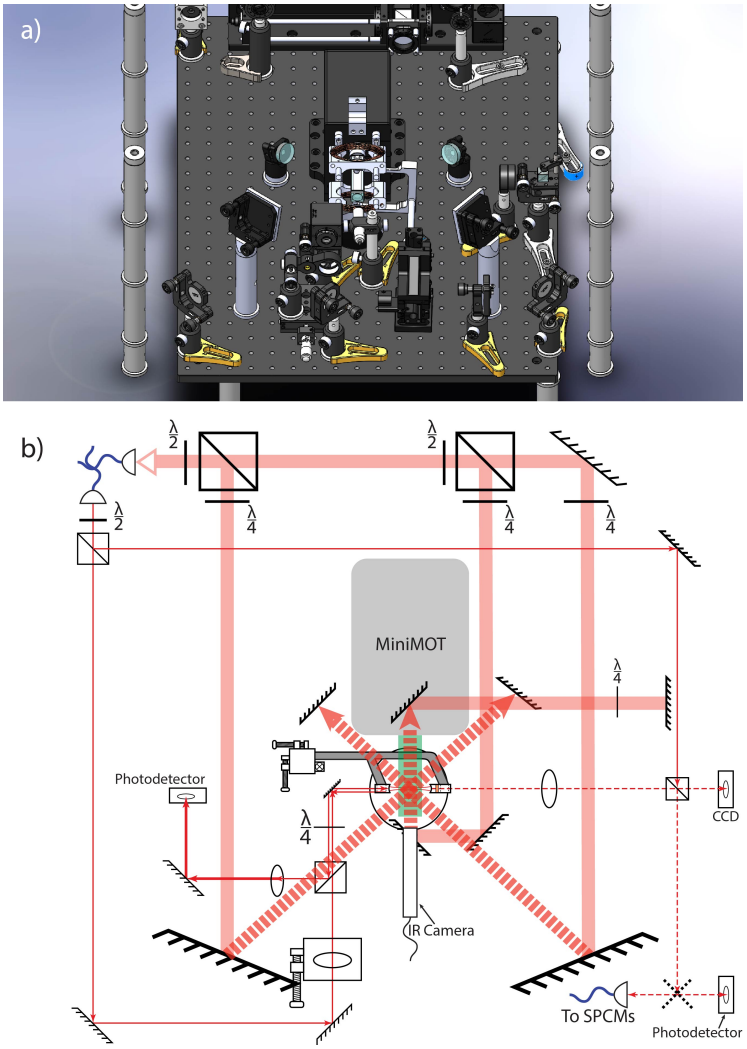

Figure 4.11: Postioning of cavities in MOT setup. a) The CAD setup indicating the position of the vertical cavity specifically. b) A diagram of the MOT and Horizontal cavity. Reproduced from [106]

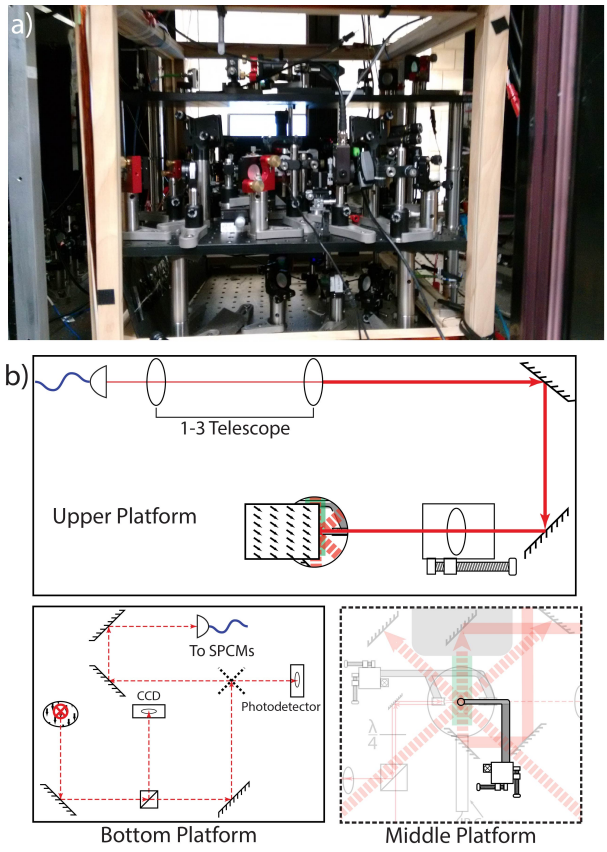

Figure 4.12: **Full Setup of the double cavity node**.a) Photo of the three platforms of the double cavity setup.b) Schematic for the in-situ implementation of the vertical cavity, consisting of 3 platforms. The upper platform (top) outputs the vertical probe beam, mode matches the beam to the cavity and deflects it downwards towards the middle platform (bottom right). A vertical cavity holder has been put in place (compare to Figure **??**). The output mode is retrieved on the bottom platform (bottom left) where it is deflected horizontally. From there it is split off to a CCD camera with a pair of magnetic mirror mounts deflecting it either to a photodiode or a capture fiber for SPCM measurement. Reproduced from [106]

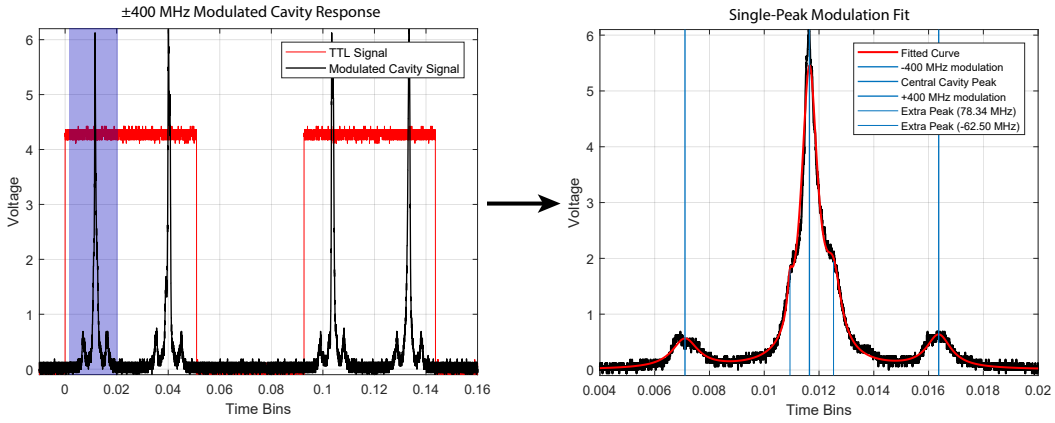

Figure 4.13: Traces from ex-situ setup: A typical cavity response to modulated light using a triangle wave piezo sweep, and the TTL signal to which the sweep was triggered. The main cavity peaks each have a pair of sidebands originating from the extra peaks from equation (4.23). The modulation allows calibration and characterization of the individual peaks (right). The known modulation frequency (400 MHz in this case) provides a conversion scale of time bins → frequency. The calibration, in this case, is 1 second ≅ 88028 MHz. Reproduced from [106]

points of the rubidium lock setup and changing the mixing down frequency. This allowed the laser to be scanned to more than one cavity peak.

This resulted in an FSR of 6.6 GHz ± 780 MHz.The ≈ 10% uncertainty The large measurement error is because of drifts between the different positions at which the FSR was measured. This can be ascribed to slow frequency drifts of an unlocked cavity a ≈ 3 minute delay between having the one locking setup and another one. Using the relation given in (4.19), the measured result gives an experimental finesse of 101 ± 12. The result of entering the 65 MHz measured linewidth into (4.19) gives a finesse of approximately 115.03.

The ex-situ vertical cavity calibration was performed using a $\omega_m = 2\pi \times$ 500MHz modulation signal. The vertical cavity displays higher-order modes that were unable to be optimized out. As it will be seen later on the vertical consistently has been more difficult to produce pure degenerate confocal modes.

The calculated vertical cavity linewidth for this configuration is 7.5 MHz. For a cavity length between 20mm and 25mm give FSR from (4.19) to be between 6GHz and 7.5GHz. Entering these values into Equation **??** results in a finesse measurement for the ex-situ vertical of 1000 or 800.

The expected finesse value given by (4.20) for mirrors r1= 99.995% and 99%

is 312. The horizontal value of 115 is ascribed to aperture losses and imperfect alignment. The high finesse of the vertical was ascribed to a combination of two high reflectivity mirrors, which explained the difficulty of alignment. The theoretical value for such a cavity would be 31000, but the losses in the cell walls would have prevented this setup to be successful.

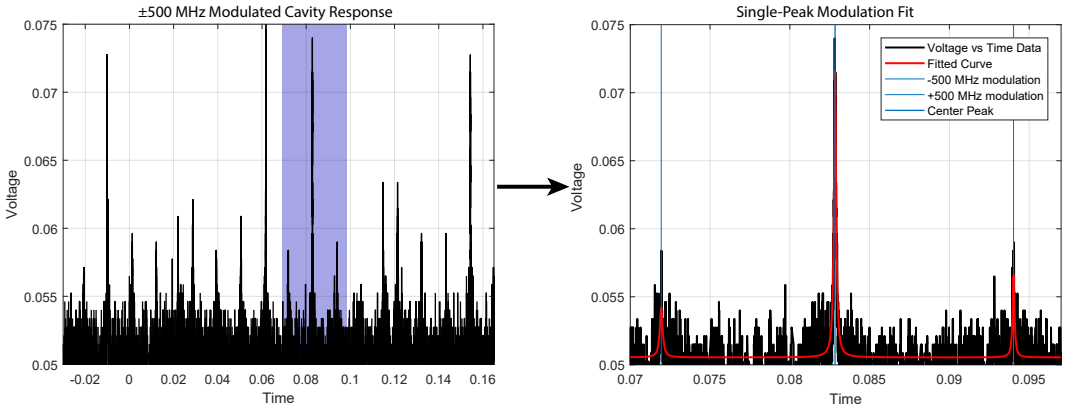

Figure 4.14: Traces from ex-situ vertical setup: A typical vertical cavity response using a triangle wave sweep. The TEM00 modes correspond to the largest peaks, and some higher order modes are present in this trace. The sidebands are distinguished from the parasitic modes by sweeping the modulation frequency. These are the only peaks that should move relative to the TEM00 mode. As before, the modulation allows calibration and characterization of the individual peaks (the right graph is the blue region magnified). The known modulation frequency (500 MHz in this case) provides a conversion scale of time bins $\rightarrow$ frequency. The calibration for this cavity is 1 second $\cong$ 45297 MHz. Reproduced from [106]

4.3.7 In-situ characterization

After the cavities were moved into the MOT setup and aligned, the characterization could be done.

To do the horizontal characterization a modulation frequency of $\omega_m = 2\pi \times 150$MHz is used. The resulting side-bands are shown in Fig. 4.15. Two different beams are incident in the cavity. Large 780nm peaks are observed, and an amplitude of 13.8 dBm modulates the modulated-peaks of a 795 nm laser. The measured linewidth of the horizontal cavity is 42 MHz.

The vertical characterization is done with a modulation frequency of $\omega_m = 2\pi \times 100$MHz. The resulting side-bands are shown in Fig. 4.16. The measured linewidth of the vertical cavity is 23 MHz.

The measured linewidth of the horizontal cavity is 42 MHz.

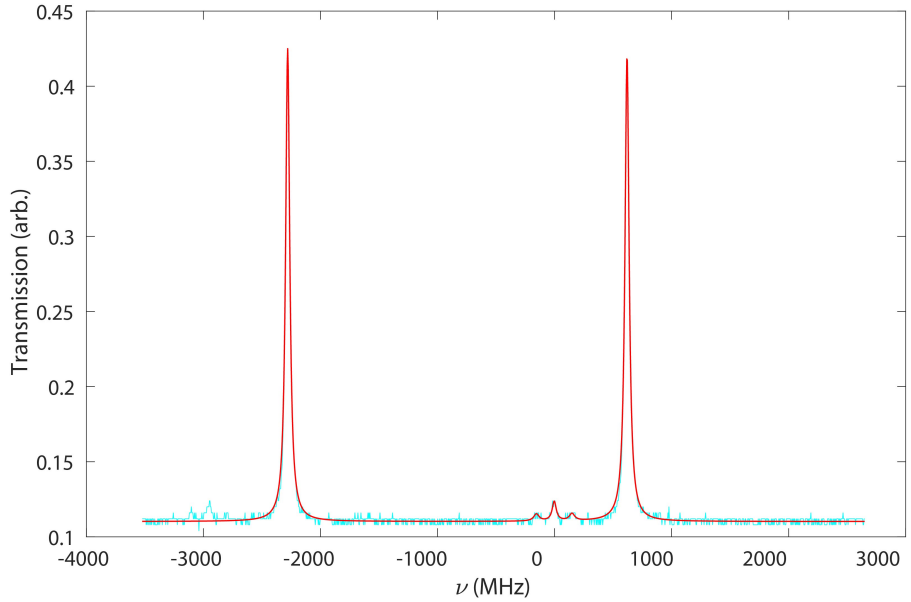

Figure 4.15: In-situ Measurement of horizontal cavity linewidth. A typical horizontal cavity response using a triangle wave sweep. A 795nm probe laser is modulated by 150MHz an amplitude of 13.8 dBm. This is then combined with the normal horizontal cavity probe field at 780nm. The measured linewidth of horizontal cavity is 42 MHz using Lorentzian fitting.

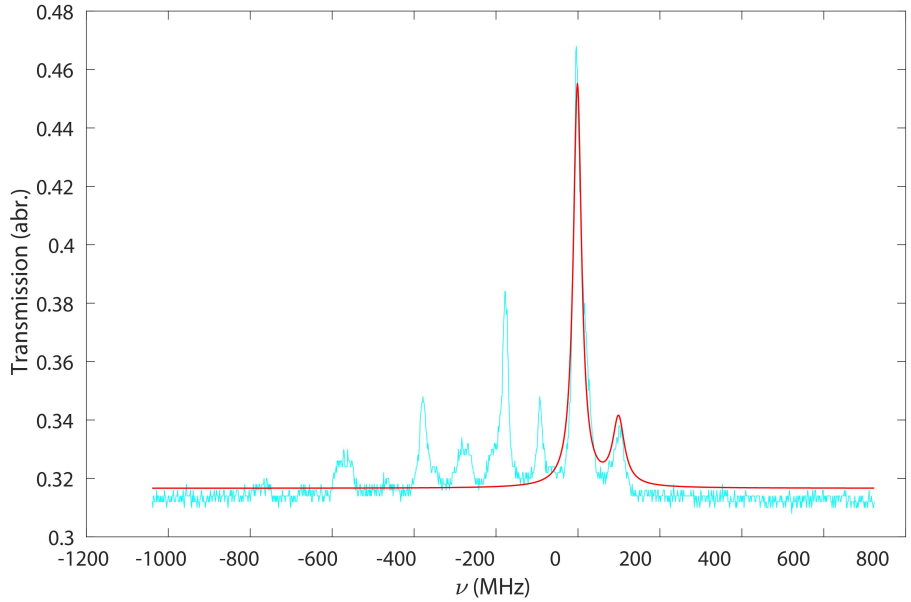

Figure 4.16: In-situ measurement of vertical cavity linewidth. We modulate the cavity modes by 100 MHz with amplitude of 10 dBm. The measured linewidth of vertical cavity is 23 MHz using a Lorentzian fit.

The values found for the FSRs of two cavity lengths of 20mm and 30mm are 7.5GHz and 6GHz, respectively.

This gives Finesse values of 178.147 and 260.87. The reason for a lower finesse than the 312 predicted can be ascribed to the losses in the cavity windows. However, if we compare it to the measurement of the horizontal ex-situ, these losses do not limit the experiment in any significant way.

4.4 Conclusion

In this chapter the design and building of the atomic and optical parts of the world's first, as far as we now, cross-cavity ensemble experiment.

I showed some of the intricacies involved with creating a MOT and two cavities in the modular and small-footprint system. The MOT was characterized and found to have of the order 10^7 atoms. The cavities were constructed, aligned and characterized ex-situ and in-situ. The finesse of the horizontal and vertical cavities was found to be 178 and 261 respectively.

This apparatus leads us to the next chapter in which I present the theory, modeling and results of scattering experiments that we did to characterize the successful coupling between the cavities and atoms.

Chapter 5

Atom cavity coupling

5.1 Introduction

In the preceding chapter it the setup of the double cavity node a was described. This chapter explains the theory and the measurements that we have used to determine that we have coupled the two cavities to the atomic ensemble.

5.2 Theory

5.2.1 Weak coupling/ large N systems

In this section, the derivation of a N-enhancement for the atom-cavity coupling is presented. This provides important context for the type of enhancement and coupling we expect to see. The susceptibility of a cavity coupled to an ensemble can be considered as a quantum mechanical [112] or classical problem [113].

Here we follow the derivation given in [112].

Starting with the Hamiltonian of an N two-level atomic system. Which is given by the following

$$H = \hbar\omega_0 \sum \sigma_i^z + \hbar\omega a^\dagger a + \sum (\hbar g \sigma_i^+ a + H.c) \tag{5.1}$$

The g is the coupling constant between a single atom and the cavity-mode which are represented by a and $a^\dagger$. The value of g is given by

$$g = \sqrt{\frac{\mu_{ge}^2 \omega}{2\epsilon_0 V}} \tag{5.2}$$

Introducing the notation for the collective coupling $S = \sum_i (\sigma_i)$ (5.1) becomes

$$H = \hbar\omega_0 S^z + \hbar\omega a^\dagger a + \sum(\hbar g S^+ a + H.c) \tag{5.3}$$

We defined the ground state as follows:

$$\psi_0\rangle = \left| N/2, -N/2; 0 \right\rangle, E = -\frac{N}{2}\hbar\omega_0 \tag{5.4}$$

where the notation $|S, M\rangle \otimes |0\rangle$ represent the eigenstates $|S, M\rangle \otimes |0\rangle$ of S^2 and S^z and $|0\rangle$ represents the vacuum of radiation. When one assumes the condition that the limit $g\sqrt{N} \gg \kappa$ hold the density matrix of the system ρ obeys

$$\frac{\partial\rho}{\partial t} = -\frac{i}{\hbar}[H, \rho] - \kappa(a^\dagger a\rho - 2a\rho a^\dagger + \rho a^\dagger a) \tag{5.5}$$

Using the eigenfunctions $|\psi_{[j]}\rangle$ and energy $E_{[j]}$ the off-diagonal elements of ρ after making the secular approximation satisfy

$$\frac{\partial\rho_{[i][j]}}{\partial t} = -\frac{i}{\hbar}(E_{[i]} - E_{[j]})\rho_{[i][j]} - \Gamma_{[i][j]}\rho_{[i][j]} \tag{5.6}$$

which leads to the following susceptibility when it interacts with radiation at frequency Ω:

$$\begin{aligned}
\chi_{\alpha\beta}(\Omega) = &\sum_{[i]} \frac{\langle\psi_0|(d_\alpha S^+ + H.c.)\psi_{[i]}\rangle\langle\psi_{[i]}|(\vec{d}_\beta S^+ + H.c.)\psi_0\rangle}{(E_{[i]} - E_0 - \hbar\Omega - i\hbar\Gamma_{[i],0})} \\
&... + \sum_{[i]} \frac{\langle\psi_0|(d_\alpha S^+ + H.c.)\psi_{[i]}\rangle\langle\psi_{[}i]|(\vec{d}_\beta S^+ + H.c.)\psi_0\rangle}{(E_{[i]} - E_0 + \hbar\Omega - i\hbar\Gamma_{[i],0})} \qquad (5.7) \\
&= \vec{d}^{\,*}_\alpha \vec{d}_\beta N \sum_{\{i\}} \frac{|\langle N/2, -N/2+1; 0|\psi_{\{i\}}\rangle|^2}{(E_{[i]} - E_0 - \hbar\Omega - i\hbar\Gamma_{[i],0})} \\
&... + \vec{d}^{\,*}_\alpha \vec{d}_\beta N \sum_{\{i\}} \frac{|\langle N/2, -N/2+1; 0|\psi_{\{i\}}\rangle|^2}{(E_{[i]} - E_0 + \hbar\Omega - i\hbar\Gamma_{[i],0})} \qquad (5.8)
\end{aligned}$$

where $\vec{d}_\alpha$ is the αth component of the dipole matrix elements $\vec{d}_{12}$.

The eigenfunctions have the structure

$$\psi_+^{(S,C)} = \cos\theta|N/2, -N/2+1; 0\rangle + \sin\theta|N/2, -N/2; 1\rangle \tag{5.9}$$

$$\psi_-^{(S,C)} = -\sin\theta|N/2, -N/2+1; 0\rangle + \cos\theta|N/2, -N/2; 1\rangle \tag{5.10}$$

$$E_\pm^{(S,C)} = \hbar\omega_0(-N/2+1) - \hbar\Delta/2 \pm \frac{1}{2}\hbar(\Delta^2 + 4Ng^2)^{1/2} \tag{5.11}$$

with the mixing angle θ and cavity-atom detuning Δ given by

$$\tan\theta = \frac{-\Delta + (\Delta^2 + 4Ng^2)^{1/2}}{2q\sqrt{N}}, \Delta = \omega_0 - \omega \tag{5.12}$$

The imaginary part of the susceptibility that gives the absorption spectrum is given by

$$\chi(\Omega) = \frac{\hbar}{\pi N \vec{d}^*_\alpha \vec{d}_\beta}\chi_{\alpha\beta} \tag{5.13}$$

$$\begin{aligned} Im(\chi(\Omega)) = cos^2\theta \frac{\Gamma_-/\pi}{\Gamma_-^2 + \{\Omega - \omega_0 + \Delta/2 - \frac{1}{2}(\Delta^2 + 4Ng^2)^{1/2}\}^2} \\ ... + sin^2\theta \frac{\Gamma_+/\pi}{\Gamma_+^2 + \{\Omega - \omega_0 + \Delta/2 + \frac{1}{2}(\Delta^2 + 4Ng^2)^{1/2}\}^2} \end{aligned} \tag{5.14}$$

This equation gives rise to the doublet structure for systems with $N \gg 1$ with peaks at $\Omega = \omega_0 \pm g\sqrt{N}$

5.2.2 Scattering theory

More pertinent to the experiments we have done is the theory of off-resonant scattering as developed in [99] and [114].

Scattering from a single atom into a mode $\mathcal{M}$ can be described by the β parameter if the scattering mode considered is small compared to the 4π steradians. This is true for Gaussian beams at optical wavelengths. The relation between the incident field E and mode $E_\mathcal{M}$ is

$$E_\mathcal{M} = i\beta E \tag{5.15}$$

with

$$\beta = \frac{k\alpha}{\pi\omega\epsilon_0} \tag{5.16}$$

since the polarizability α obeys the optical theorem we have

$$|\beta|^2 = \frac{6}{k^\omega} Im(\beta) = \eta_{fs} Im(\beta) \tag{5.17}$$

Inside a cavity, the incident field on an atom, E consists of any field coming from outside the cavity (E_{in}) and the resonating cavity field (E_C). The cavity field needs to be in a stable cavity mode $E_\mathcal{M}$ as shown in Fig.5.1.

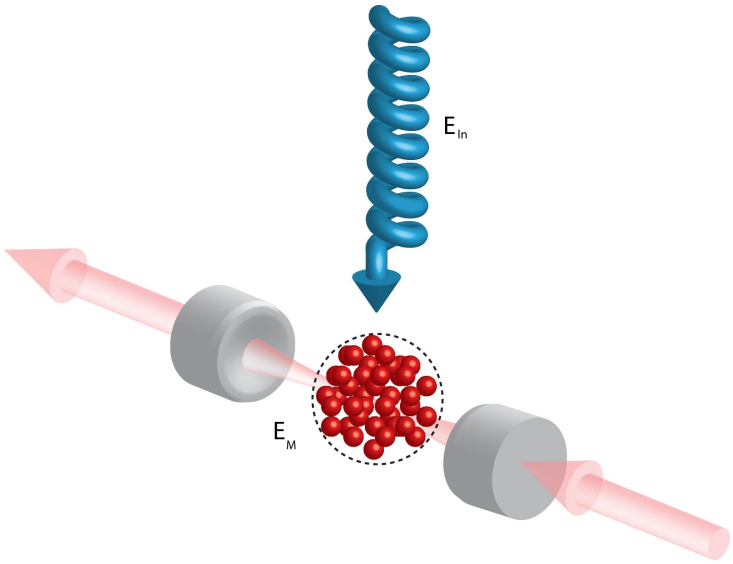

Figure 5.1: The scattering of light into the cavity mode off the atoms. Any field coming from outside the cavity E_{in} is scattered into the cavity mode $E_C = E_{\mathcal{M}}$.

The steady-state behavior of the system is given by the constraints on the different fields. For an empty cavity, the cavity field has to obey the round-trip condition:

$$E_C = 2E_M + r^2 \exp(2ikL)E_C \tag{5.18}$$

which close to resonance solves in the low transmission limit lead to a Lorentzian

$$E_C = \frac{2E_{\mathcal{M}}}{q^2}\frac{1}{1-2i\delta/\kappa} \tag{5.19}$$

with $q^2 = \frac{\pi}{\mathcal{F}}$ and $\mathcal{F}$ is the cavity finesse.

When we use this calculated cavity field as part of the incident field we find that the relation of (5.15) becomes

$$E_M = i\beta(E_{in} + 2E_C)$$

and subsituting (5.19) we have

$$= i\beta(E_{in} + \frac{4E_{\mathcal{M}}}{q^2}\frac{1}{1-2i\delta/\kappa}) \tag{5.20}$$

solving $E_{\mathcal{M}}$ gives

$$E_M = \frac{2i\beta E_{in}}{q^2}\frac{1}{1-i\frac{2\delta}{\kappa}-i\frac{4\beta}{q^2}} \tag{5.21}$$

The extension to an N atom ensemble comes down to adding two coupling terms $\mathcal{H}, \mathcal{G}$ is the coupling between a incident field along the cavity and the atoms and a perpendicular driving field and the atoms, respectively.

$$\mathcal{H} = \frac{1}{N}\sum_{n=1}^{N} cos^2\Big[\frac{2\pi}{\lambda_L} z_n\Big] \tag{5.22}$$

$$\mathcal{G} = \frac{1}{N}\sum_{n=1}^{N} \exp\Big[i\frac{2\pi}{\lambda_L} y_n\Big] cos\Big[\frac{2\pi}{\lambda_L} z_n\Big] \tag{5.23}$$

Then (5.21) becomes:

$$E_M = \frac{2i\beta N E_{in}\mathcal{G}}{q^2}\frac{1}{1 - i\frac{2\delta}{\kappa} - i\frac{4N\mathcal{H}\beta}{q^2}} \tag{5.24}$$

By relating in the RWA the finesse scattering to the atomic lineshape and cavity cooperativity.

$$\Big(\frac{4\beta}{q^2}\Big) = 2C\mathcal{L}(\Delta) \tag{5.25}$$

we get the form

$$E_C = -\frac{E_L}{2}\frac{N\mathcal{G}}{\frac{i}{2C\mathcal{L}(\Delta)} + \frac{\delta}{2\kappa C\mathcal{L}(\Delta)} + N\mathcal{H}} \tag{5.26}$$

5.3 Experimental Setup

5.3.1 Coupling atoms to cavities

Cavity output measurement

The cavity is coupled to a polarization maintaining single mode fiber that leads to a (Laser Components COUNT) single photon counting module (SPCM). A Qutools quTAU time-to-digital converter (TDC) registers the pulses from the SPCM. The TDC windows of the quTAU are 81ps long. Maximally one detection event per window is registered. The exposure time can be set through the hardware or analysis software. All the data presented in the rest of the chapter was with an exposure time of 1ms.

The cavity response of the horizontal cavity was seen on the SPCMs. The first investigation was to identify the different sources of light.

A pulse sequence that left us with the following cases was followed.

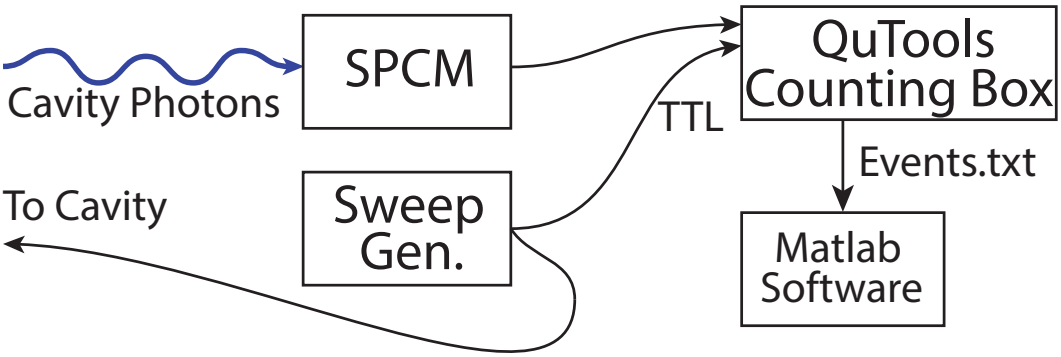

Figure 5.2: Schematic of SPCM measurements performed: a function generator sweeps the cavity length via piezo while sending a trigger to a control box. The SPCM counts photons and the control box outputs trigger information and photon events as a .txt file. The control box has eight channels, for four such setups. Reproduced from [106]

(I) Weak probe field only

(II) Cooling and repumper fields only.

(III) Cooling and probe field

(IV) MOT and probe.

5.4 Analysis

Equation (5.26) was used to generate a simulation for the response of scattering data.

The values for the parameters used are given in the Table 5.1

g	$2\pi\times$ 517kHz
κ	$2\pi\times$ 42MHz
Γ	$2\pi\times$ 6MHz
λ	780nm
w_0	50 μ m
Δ	$2\pi\times$ 18MHz

Table 5.1: Parameters used in the simulation of the scattering into the cavity modes.

An essential addition to the model was the following. The atoms are given a collective phase oscillation dependent on the detuning between the cavity added to account for the geometric effect of having a scanning cavity.

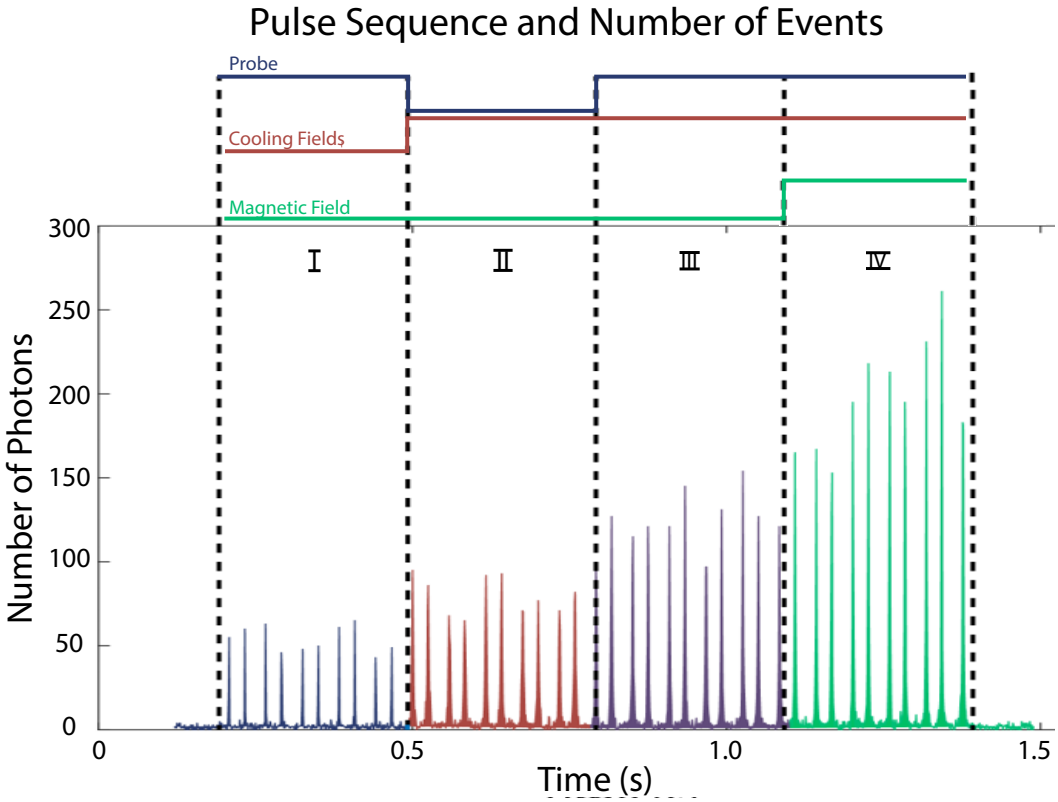

Figure 5.3: Data for various states of cavity probe and MOT. In region (I) a weak probe ($\approx$ 5nW) is input into the cavity with warm background gas, resulting in an average 54 photons/peak. In region (II), the atoms are prepared in optical molasses, and the probe is switched off, resulting in an average peak value of 64. In region (III), the probe is switched back on, resulting in an average 126 photons per peak. In region (IV) the atoms are prepared in a magneto-optical trap, with on average 156 photons/peak. This region also displays a distinct 'ramping' behavior compared to the other three regimes due to the 'loading time' of the MOT, during which the cloud has not reached equilibrium.

Also, the assumption regarding the phases between the atoms is this, for each event, since the OD is high enough, there is at least one atom that is close to the phase required to create a coherent scattering, with a small offset.

The number of atoms that were used was 10 000 to 500 000, and the result is not N dependent at this limit. But since $\mathcal{G}$ should be N-dependent we accept this to be our limiting behavior of the system.

Using the setup as described in section 5.3.1 we measured the effects of the scattering of the cooling photons into the cavity. First, a probe sweep is done, i.e. the MOT fields are blocked and the probe is turned on. Using the finesse measurement done in section 4.3.7 we do a calibration of the scanning of the cavity measurement. The SPCM data is integrated and we fold the peaks on top of each other. The mean curve is produced and this FWHM is identified as the cavity response. Keeping the scanning time constant this ratio is then used to calibrate the splitting of the cavities, once the atoms are in place.

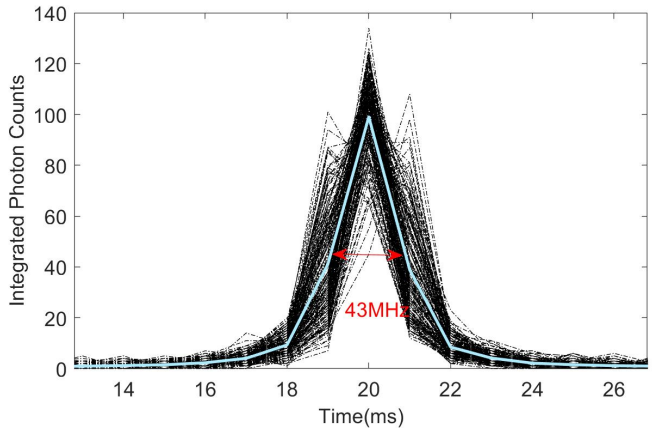

Figure 5.4: Probe sweep of horizontal cavity used to calibrate the scan range. The linewidth of 42MHz measured in Sec. 4.3.7 is used to calibrate the time-scale of the scan.

Blocking the probe and unblocking the cooling fields, the scattering experiment is done. By scanning the horizontal cavity at 10Hz with an amplitude of roughly 300V we could see the traces as shown in figure 5.5.

The power of the cooling beams in these experiments were 11mW. After the data taking the data is analyzed using MATLAB code that folds the different peaks on top of each other. The different time window results are indicated as black dots in Fig. 5.5. We then take the average of these values to produce the blue lines in the figure. If we compare this to the result of the simulation 5.6 a fair amount of overlap is present.

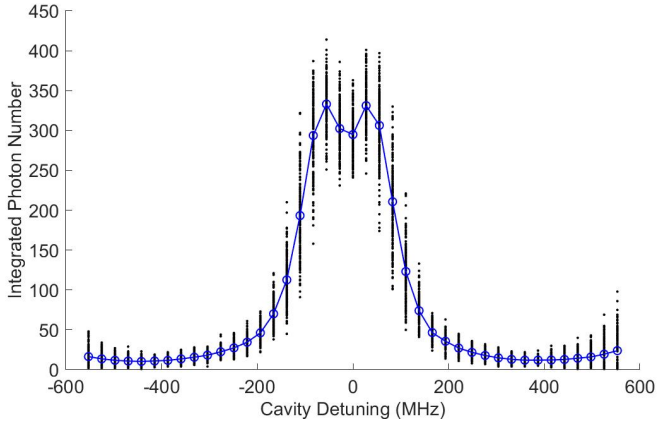

Figure 5.5: Scattering Data from the horizontal cavity. The scan is folded into time-windows based on the peak positions. The black dots represent the data and the blue line the average over these.

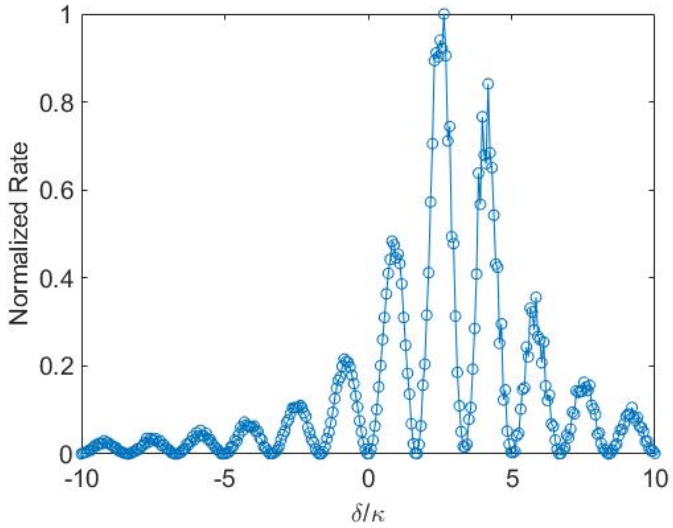

Figure 5.6: Result of the Horizontal cavity simulation. The depth of the frequency oscillation is not dependent on the number of atoms and should filter out of the system as detected by the SPCMs.

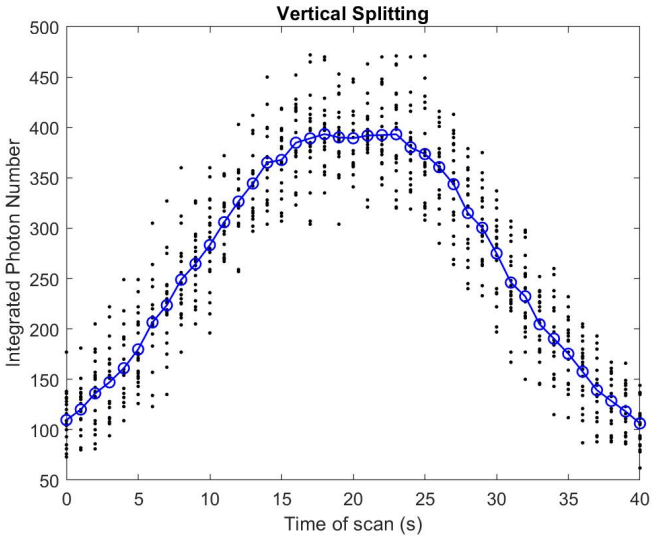

Figure 5.7: Data from the vertical cavity.

For the vertical, the following is the result of the vertical simulation

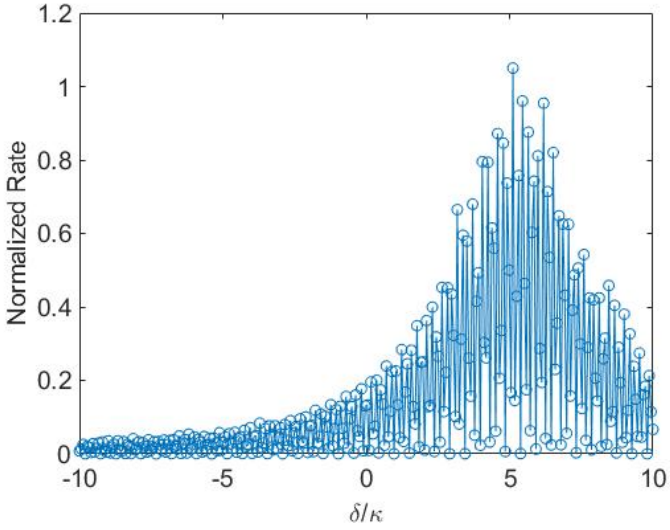

Figure 5.8: Result of the vertical cavity simulation. The high frequency oscillation is not dependent on the number of atoms and should filter out of the system as detected by the SPCMs.

We want to emphasize that these plots show that the cavities are coupled to the atomic medium to such an extent that the scattering of the light is

affected by the back-action of the cavities. This shows that we have succeeded in coupling both of the cavities to the atomic cloud. In Fig. 5.10 we see a Vacuum Rabi Splitting that corresponds to the parameters discovered from this scattering.

This allows us to proceed in evaluating experiments that harness this coupling to produce thin EIT lines and provide the high OD environment that the cavities add.

5.5 Conclusion

In this chapter, I showed some of the preliminary results of two-cavity experiments. We believe that we have successfully coupled the two cavities to the MOT. More predictions of the future work to use simultaneous coupling will be made in Chapter 7, but in keeping with results that have already been achieved first, I will discuss the work on quantum simulation in the next Chapter. Ultimately, we would like to use this system together with the quantum simulation in future experiments.

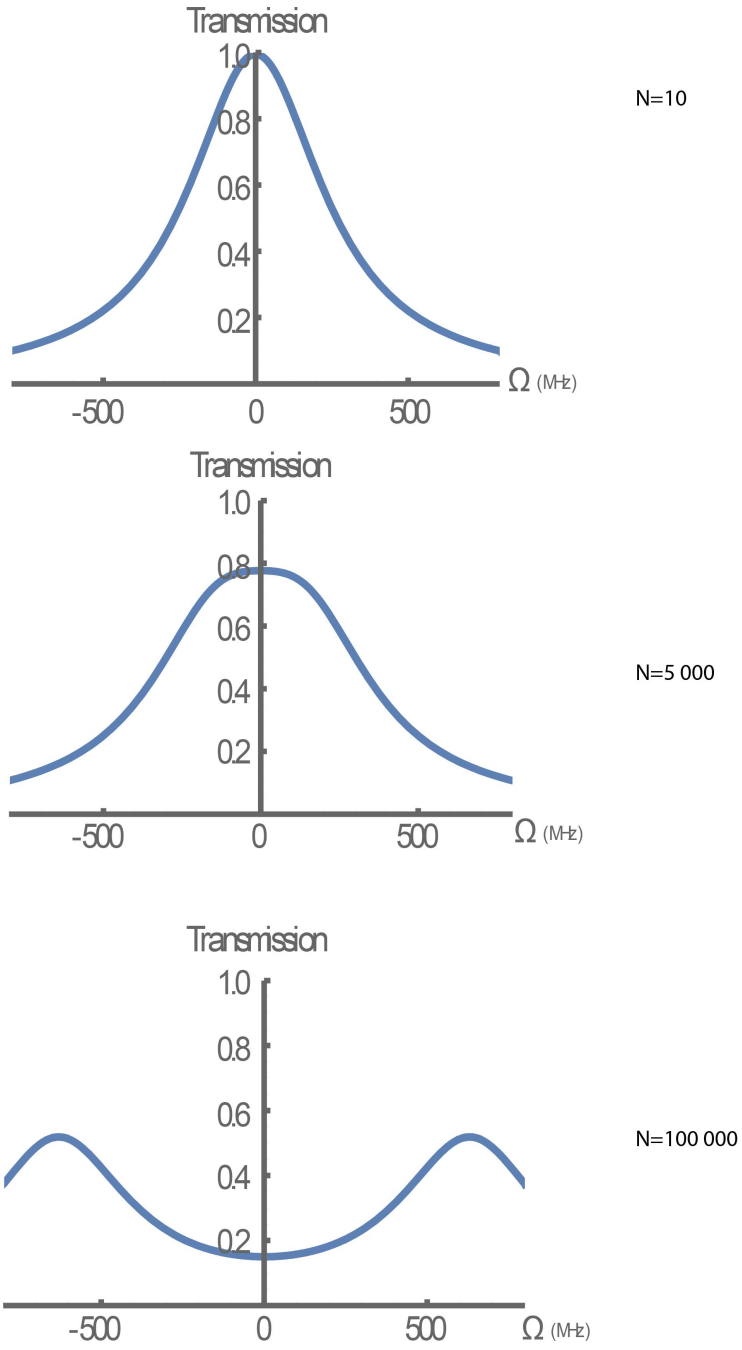

Figure 5.9: Vacuum Rabi Prediction for horizontal cavity. Comparing different atom numbers with the decay terms evaluated by equations and used in the simulation. $[g, \kappa, \Gamma] = 2\pi \times [320kHz, 42MHz, 6MHz]$

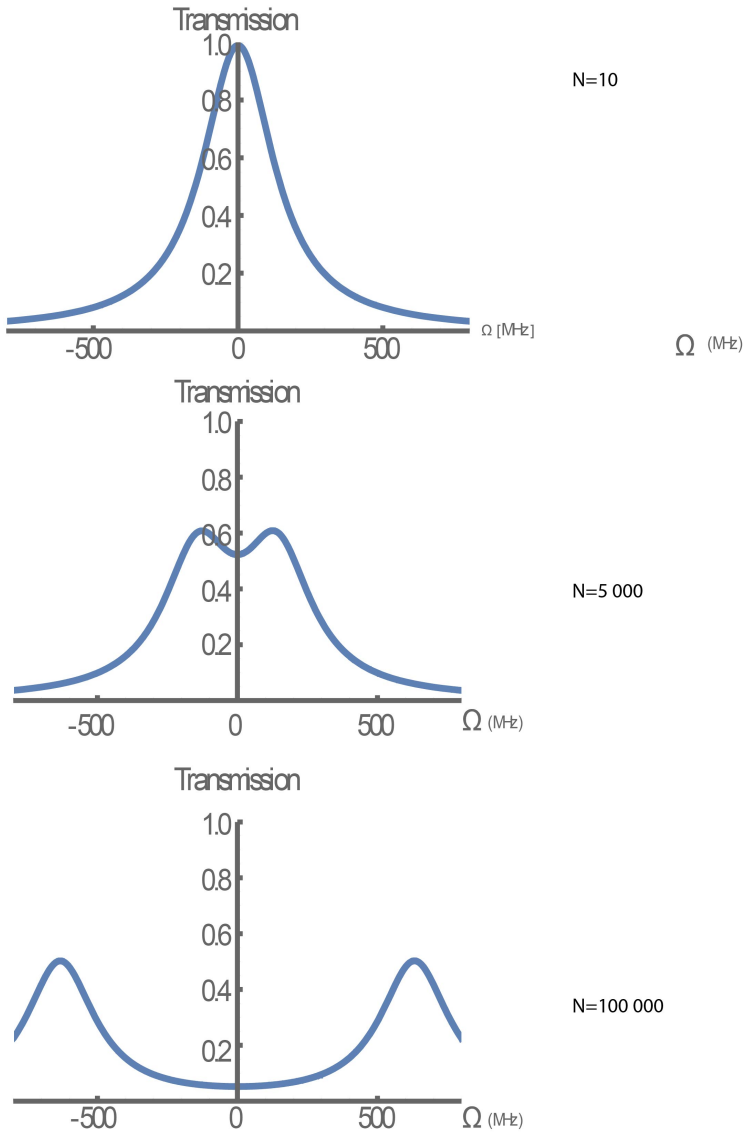

Figure 5.10: Vacuum Rabi Prediction for vertical cavity. Comparing different atom numbers with the decay terms evaluated by equations and used in the simulation. $[g, \kappa, \Gamma] = 2\pi \times [320kHz, 23MHz, 6MHz]$

Chapter 6

Quantum Simulation using Spinor Slow Light

The hardware presented in the previous chapter enables one to think about different applications for this kind of network node. One way to incrementally improve the designs and understanding of the system is to find applications that fit its current specifications. There is great value in controllable quantum systems with more than one photonic field strongly coupled to an atomic cloud in the field of quantum simulation.

In this chapter, I present the work we have done to illustrate this in our room-temperature platform to simulate the dynamics of relativistic quantum particles specifically the Dirac model and the Jackiw-Rebbi model. The Jackiw-Rebbi model is of interest to high energy as well as condensed matter physicists, since it has different topological phases.

I start with an introduction of quantum simulation, the general platform we are using, the theoretical background of the models, experimental implementation, results and discussion. Finally I go through simple conceptual models of how this can be implemented in the nodes and networks I've shown before.

Disclaimer I would like to acknowledge the team and collaborators who made this research possible. The main results of this chapter and a portion of the text and discussion are based on our recent manuscript: "Realizing topological relativistic dynamics with Slow light polaritons at room temperature" Namazi. Mehdi, Jordaan. Bertus, Noh. Changsuk, Angelakis. Dimitris. G, Figueroa. Eden, a rXiv:1711.09346. Mehdi Namazi lead this project. Our collaborators, Dimitris Angelakis and Changsuk Noh, did the numerical simulation of the results. I took part in the data acquisition and analysis. All authors contributed to drafting the manuscript. A more in-depth version

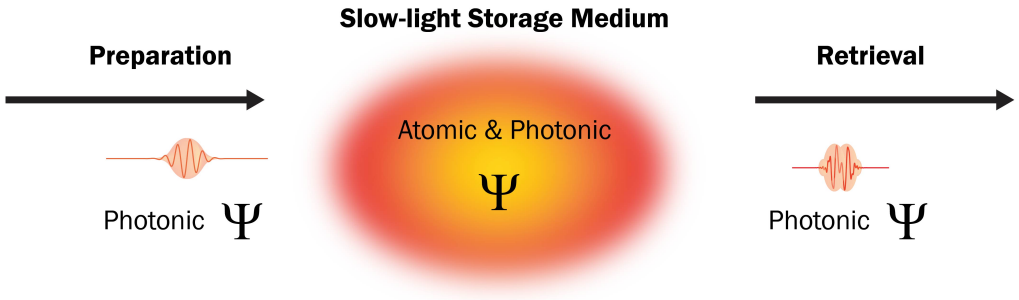

Figure 6.1: Cartoon of quantum simulation. It highlights the versatility of the simulation platform that dark state polaritons(DSPs) provide for quantum simulations. Preparation and retrieval are done with photonic states and make it ideal for a photonic network.

of this work can be found in Mehdi's thesis *"A Scalable Room-Temperature Quantum Processing Network"*

6.1 Introduction to Slow-light quantum simulation

In his seminal work [115] Richard Feynman proposed that by constructing a mathematical relation between two systems one can use a controllable quantum device to simulate the physics of another quantum system.

The controllability of atomic systems has made it ideal for simulations like this. There has been many successful quantum simulations done in recent history including ultra-cold atoms [116], trapped-ions [117]and superconducting qubits [118]. Photonic setups have also been used to emulate relativistic and topological models [119, 120].

Figure 6.1 shows a cartoon diagram of the quantum simulation platform that we have created. It highlights the flexibility that dark state polaritons(DSPs), as introduced in Chapter 2, provide for quantum simulations. Since the polaritons can exist in a different quantity of atomic and photonic part, we can do the state preparation and retrieval stages with purely photonic wavefunctions, exploiting the success of quantum optics. The evolution of the simulation is done inside a slow light storage medium, where the DSP is in a superposition of atomic and photonic states.

The important mathematical relations for this particular simulation platform is provided from the 1+1 Dirac model. Unanyan et al. [121] did the detailed derivation of how a tripod linkage pattern creates a superposition of DSPs between two ground states and can be related to the 1+1 Dirac model.

Following the theoretical paper of our collaborators [122] we aimed to model the Jackiw-Rebbi. The Dirac equation can be extended by having the mass term spatially dependent. One such extension is where the mass undergoes a sign-change. At the transition point of the sign-change the equation can be solved by a new localized zero energy solution [121, 123]. The JR model describes the coupling of a background scalar field coupling to the Dirac particles and gives a mass term $m_eff = tanh(x)$. This kink has the property of leading to $m_eff(-\infty) = -m0$ and $m_eff(\infty) = m0$, leading to the necessary condition for a localized zero energy solution.Also, the soliton mode is protected by the topology of the background field.

Since it is known that the JR model is equivalent to the SSH model [124] that describes the polyacetylene molecule, under the correct regularization, it can be considered a chiral topological Dirac insulator in class AIII [125]. The regularization is required to add a distinction between the topologically trivial or nontrivial phases since the JR model has the same symmetry in terms of positive and negative masses as the Dirac equation has [Springer2012]. Even with this limitation, this was historically the first model to show the relationship between topology and gapless modes [124], preceding the more well-known integer and fractional quantum Hall effects. The relationship with other field theoretical models and topological systems [125], makes it a suitable test case to highlight the abilities of our novel quantum simulation platform. Such a system is interesting because of the interest in topological systems, but also for the possibilities of gaining insights into relativistic particles using this platform.

6.2 Theoretical background

6.2.1 JR model

The Dirac equation in 1+1 dimension reads

$$i\partial_t \mathbf{\Psi} = -ic\alpha\partial_z \mathbf{\Psi} + \beta mc^2 \mathbf{\Psi} \tag{6.1}$$

in which c is the speed of light, $\alpha^2 = \beta^2 = 1$ and anticommute $\{\alpha, \beta\} = 0$. One possible choice is $\alpha = -\sigma_z$ and $\beta = \sigma_y$ in terms of the usual Pauli matrices, which means that the wavefunctions $\mathbf{\Psi}$ are 2 component objects in 1+1 dimension. Following Jackiw and Rebbi let us replace the mass with a position dependent field:

$$i\partial_t \mathbf{\Psi} = -ic\alpha\partial_z + \beta c^2 \phi(z) \mathbf{\Psi}. \tag{6.2}$$

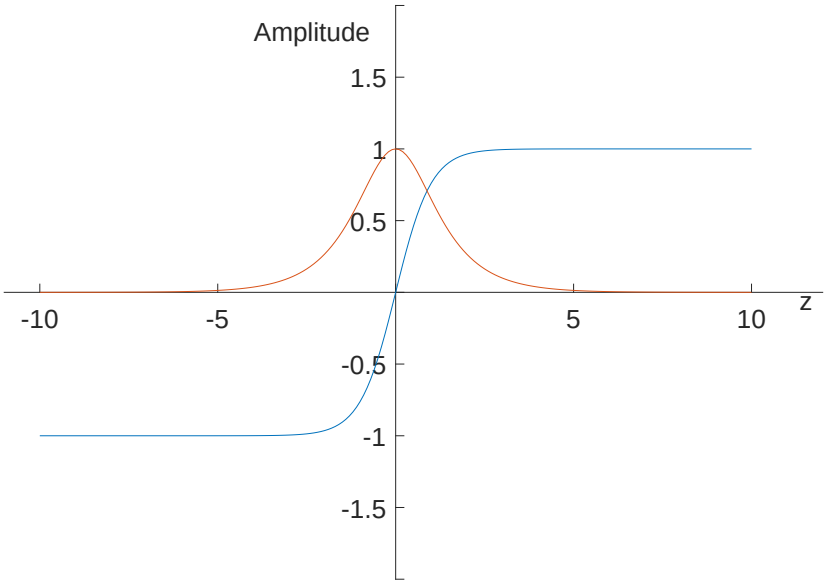

Figure 6.2: **Zero energy mode of JR model**. The blue curve shows the soliton profile of the background field. The red curve shows the zero energy mode produced in the JR model.

Noting that the sign of the mass can be changed, they considered a kink solution that interpolates between the negative and positive signs. Choosing $\phi(x) = \tanh(\lambda z)$, one sees that the solution

$$\mathbf{\Psi}_{zero}(z) = \exp\left(-c\int^{z} dz'\phi(z')\right)\chi = \exp\left[-c\ln\left(\cosh\lambda z\right)\right]\chi \tag{6.3}$$

with $\alpha\beta\chi = -i\chi$ is a zero-energy solution localized around $x = 0$. For our choice of α and β, $\chi \propto (1, -1)$ and we will denote the spatial part with $\phi(z)$ such that

$$\mathbf{\Psi}_{zero}(z) \equiv \psi_{zero}(z)(1, -1). \tag{6.4}$$

This zero-energy mode is shown in Figure 6.2 The presence of the zero-mode was shown to be robust against the detailed form of the kink. What is important is the topology of the kink: that it undergoes a significant change as z changes.[122, 126].

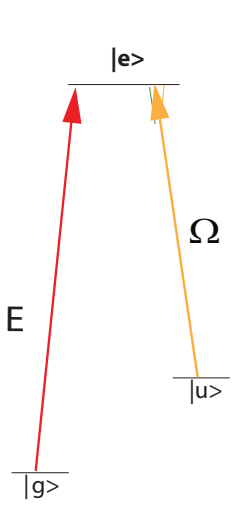

(a) Level scheme for a DSP. Strong control field Ω and weak probe field E

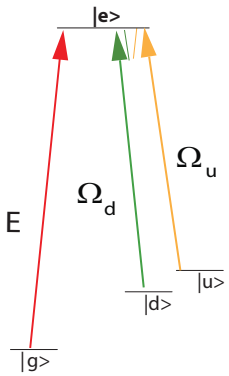

(b) Level scheme for a Tripod. Strong control fields $\Omega_{u,d}$ coupled from two different low-lying states with weak probe field E. Reproduced from

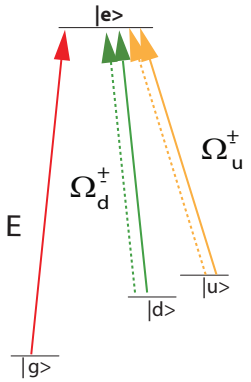

(c) For the creation of the dual tripod configuration, the original field $E(z,t)$ is converted into two counter-propagating fields ($E_-(z,t)$ and $E_+(z,t)$) by introducing two pairs of counter-propagating control fields (Ω_d^+, Ω_u^+, Ω_d^- and Ω_u^-).

Figure 6.3: Increasing complexity toward SSL

6.2.2 Tripod based dark state polaritons.

The building block of the quantum simulation work is the Dark State Polariton. $\Psi(z,t)$ [127]. This is created by a level scheme such as Fig. 6.3a. Based on the usual EIT assumptions, the following equation describes the propagation of the probe $E(z,t)$ under Ω:

$$(\partial_t + v_g\partial_z)E(z,t) = +i\frac{g_\varepsilon^2}{\Omega^2}N\frac{\delta}{2}E(z,t)$$

where $v_g = \frac{c}{1+\frac{g_\varepsilon^2}{\Omega^2}N}$ is the group velocity of the input field in the atomic medium, N is the number of atoms along the beam path, δ is the two-photon detuning and g_ε is the light-matter coupling constant for $E(z,t)$. In the perturbative and adiabatic limit a similar equation for the atomic operator σ_{gu} can be found. The solution to the combined system of equations is a superposition of $E(z,t)$ and $\sigma_{gu}(z,t)$ and is called a dark state polariton, $\Psi(z,t) = \cos\theta E(z,t) - \sin\theta\sigma_{gu}(z,t)$.

In the tripod configuration Fig 6.3b (defined as tripod-type linkage pattern in [128] two control fields Ω_u and Ω_d create two DSPs, $\Psi_u(z,t)$ and $\Psi_d(z,t)$.

The response of the system is then given by a linear combination of the two DSPs also known as the tripod DSP,$\Psi_T = \alpha\Psi_d + \beta\Psi_u$, with $\Psi_{d(u)}(z,t) = \cos\theta_{d(u)}E(z,t) - \sin\theta_{d(u)}\sigma_{gd(u)}(z,t)$ [127].

6.2.3 JR dynamics with DSPs

To mimic the Dirac equation (6.1), the first step is to create a two-level system. Each level of this system can be an independent Tripod DSP state. The interaction between these two tripod DSPs needs to be engineered to follow the 1+1 Dirac Hamiltonian. This can be achieved within two steps: 1) If the tripod DSPs have opposite k-vectors, the spatial variation of the two-level system along the z-axis couples to the Pauli's z-matrix. Assuming two pairs of counterpropagating control fields, see Fig 6.3c solid and dashed lines, the evolution of the two probe fields $E^+(z,t)$ and $E^-(z,t)$ can be derived as [128]:

$$(\partial_t - v_g\sigma_z\partial_z)\begin{pmatrix} E^+(z,t) \\ E^-(z,t)\end{pmatrix} = ig_\varepsilon^2(\mathbf{\Omega^{-1}})^2N\sigma_z\frac{\delta}{2}\begin{pmatrix} E^+(z,t) \\ E^-(z,t)\end{pmatrix}$$

where $\mathbf{\Omega} = \begin{pmatrix} \Omega_d^+ & \Omega_u^+ \\ \Omega_d^- & \Omega_u^-\end{pmatrix}$. Without the two-photon detuning, the R.H.S of the equation equals zero which is the special case of two independent tripod DSPs. Even after applying the proper two-photon detuning, it is the $\mathbf{\Omega}$ matrix that allows a coupling term proportional to Pauli's x- or y-matrix to correctly mimic a 1+1 Dirac Hamiltonian. By individually manipulating the parameters of the control fields, $\mathbf{\Omega} = \Omega\begin{pmatrix} 1 & i \\ i & 1\end{pmatrix} = \Omega(1+i\sigma_x)$ which results in

$$i\hbar(\partial_t - v_g\sigma_z\partial_z)\begin{pmatrix} E^+(z,t) \\ E^-(z,t)\end{pmatrix} = \hbar\frac{g_\varepsilon^2}{2\Omega^2}N\sigma_y\frac{\delta}{2}\begin{pmatrix} E^+(z,t) \\ E^-(z,t)\end{pmatrix}. \tag{6.5}$$

It is possible to derive a similar equation for the atomic operators $\sigma^\pm(z,t) = \frac{1}{\sqrt{2}}(\sigma_{gu} \pm i\sigma_{gd})$, thus constructing an equation for spinor of slow light (SSL) object $\mathbf{\Psi} = \binom{\Psi^+}{\Psi^-}$ as:

$$i\hbar\partial_t\mathbf{\Psi} = \left(i\hbar v_g\sigma_z\partial_z + m_{eff_0}v_g^2\sigma_y\right)\mathbf{\Psi} \tag{6.6}$$

with $\Psi^\pm(z,t) = \cos\theta E^\pm(z,t) - \sin\theta\sigma^\pm(z,t)$ and $\theta = \arctan(\sqrt{\frac{g^2N}{\Omega^2}})$ [121]. Equation (6.6) clearly resembles the Dirac equation (6.1) with the 'speed of light' v_g and mass $m_{eff_0} = \hbar\frac{\delta}{2}\frac{1}{v_g^2}\sin^2(\theta)$. JR model is achieved by allowing the effective mass to vary with z, which in turn can be achieved by controlling the two-photon detuning as a function of z.

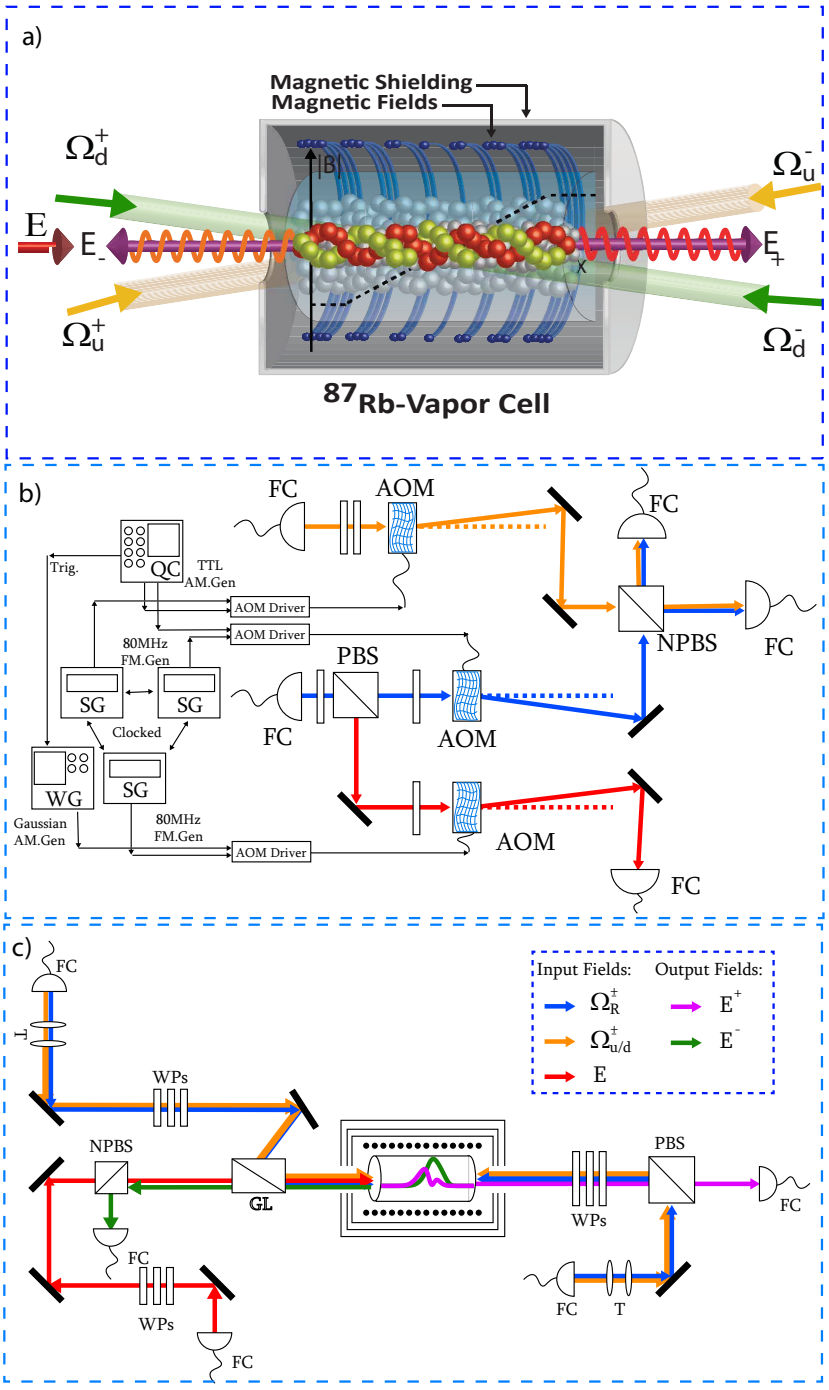

Figure 6.4: (a) The conceptual overview of the experiment. Counter propagating control fields ($\pm$) couple that are effectively coupled to the two different tripod states (u, d) as indicated by the green and yellow control fields (Ω_d^+,Ω_d^-, Ω_u^+, Ω_u^-) (b) Detuning of the different fields using AOM drivers (c) The experimental setup of how the different fields were incident on the vapor cell. Attention is drawn to the two input control fields from the different sides $\Omega_{u,d}^{\pm}$ (yellow) and the two output probe fields $E^{\pm}$ in pink and green.

6.3 Experimental Realisation.

6.3.1 Apparatus

The experiment was carried out in a ^{87}Rb vapor cell as in Chapter 2. We employed two amplified external-cavity diode lasers (Toptica TA Pros) to address the different atomic transitions. Acousto-Optical Modulators are used to prepare the different detunings (Fig. 6.4 (b)). Finally Si photodiodes (Thorlabs PDA 10) are used to detect the output fields (Fig. 6.4 (c))

6.3.2 Creation of tripod DSP.

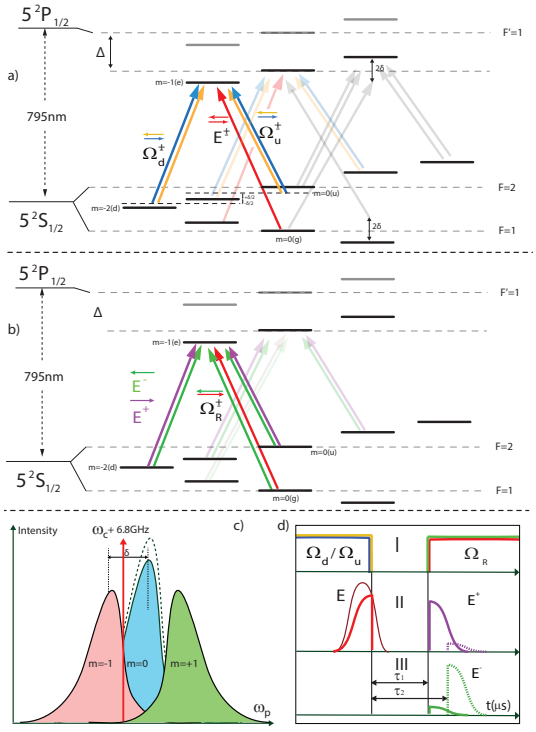

Figure 6.5: **Storing and retrieval of light pulses for the simulation**(a) The magnetic field induces Zeeman splitting such that we see the different lambda systems produced as shown.This shows the setup for storing. (b) The setup for retrieval. (c) A specific detuning of the laser field are chosen to couple weakly to the other Zeeman splitted levels as shown in lighter arrows in (a) and (b). (d) Pulse sequence of the experiment.

All the transitions used in the experiment are within the ^{87}Rb D_1 line. The storage is based on EIT. The probe is stabilised using top-of-fringe locking to

saturation spectroscopy of a Rb vapour cell and the control field is stabilised by an optical phase lock loop to the probe field. The probe pulses $E(z,t)$ with a width of 400 μs is tuned to $5S_{1/2}|F, m_F = 1, 0\rangle \rightarrow 5P_{1/2}|F', m_{F'} = 1, 0\rangle$ ($|g\rangle \rightarrow |e\rangle$) (with detuning $\Delta = 250MHz$). The writing control fields (Ω_u and Ω_d) are tuned at $|F, m_F = 2, 0\rangle \rightarrow |F', m_{F'} = 1, 0\rangle$ ($|u\rangle \rightarrow |e\rangle$ with detuning $-\delta/2$) and $|F, m_F = 2, -1\rangle \rightarrow |F', m_{F'} = 1, 0\rangle$ ($|d\rangle \rightarrow |e\rangle$ with detuning $+\delta/2$)(see Fig. 6.5 a). The EIT lines have an average FWHM of 1.2 MHz [23]. We create the tripod DSP Ψ_T in an atomic ensemble using EIT in the following way. Firstly, three separated EIT systems are created by breaking the degeneracy of the Rb atoms Zeeman sub-levels through applying a DC magnetic field B (see Fig. 2a) with a δ/B ratio of 1.09 MHz/G.
Secondly, we isolate two of the EIT systems by using a single control laser that is symmetrically detuned ($\pm\delta/2 = \pm g_d \mu_B B/2$) from the transitions $|u\rangle \rightarrow |e\rangle$ and $|d\rangle \rightarrow |e\rangle$, effectively forming two control fields Ω_u and Ω_d (see Fig. 2b). Lastly, we send a pulse of light ($E(z,t)$) undergoing tripod DSP dynamics due to Ω_u and Ω_d, thus creating the components of Ψ_T (Ψ_u and Ψ_d). We calibrate the coherence of this tripod scheme by storing Ψ_T and retrieving it using a co-propagating control field (Ω_R) coupled to the $|g\rangle \rightarrow |e\rangle$ transition. The retrieved tripod DSP ($\Psi_T^{'}$) has two components, $\Psi_u^{'}$ and $\Psi_d^{'}$ with a frequency difference $\delta = \omega_{ue} - \omega_{de}$. We find a suitable δ by choosing a magnetic field B that maximizes the beat note in the retrieved mode.

The tripod DSP Ψ_T is created using Ω_u and Ω_d. The time sequence of the creation of Ψ_T and the readout of $\Psi_T^{'}$ is shown in Fig.6.5(d). Ψ_T is stored for $2\mu s$ after which it is mapped onto $E_d^{'}$ and $E_u^{'}$ using Ω_R. Ω_R is tuned to $|F, m_F = 1, 0\rangle \rightarrow |F', m_{F'} = 1, 0\rangle$ ($|g\rangle \rightarrow |e\rangle$). Polarisation elements supply 42 dB of control field attenuation (80% probe transmission). We measure the optical component of $\Psi_T^{'}$ showing the detuning δ between $E_d^{'}$ and $E_u^{'}$ in the form of a beat note (with frequency δ) which is controlled using B.

6.3.3 Measurement of 1+1 Dirac Dynamics.

Once suitable atom-light detunings are chosen, we proceed to create the SSL $\mathbf{\Psi}$. We use two control fields (Ω_u^+ and Ω_d^+) co-propagating with the probe $E(z,t)$ and two additional counter-propagating control fields Ω_u^- and Ω_d^- (see Fig. 6.5a). The created SSL components $\Psi^{\pm}$ are then stored for 2μs. During storage, the interaction of Ψ^+ and Ψ^- follows the Dirac dynamics outlined by equation 6.6.

After storage, these dynamics are mapped onto the SSL components $\Psi'^{\pm}$ by applying the counter-propagating control fields Ω_R^+ and Ω_R^- (see Fig. 6.5 b). We detect the optical form of $\Psi'^{\pm}$ ($E'^{\pm}(z,t)$) simultaneously in independent

photo-detectors.

We vary the storage time for fixed two-photon detuning, thus changing the interaction time between the SSL components. Each pair of correlated experimental points is obtained by measuring the respective storage of light signals, integrating its total energy for varying storage time. We observe coupled oscillations for the intensities retrieved in each direction, $|E'^{+}(z,t)|^2$ (blue dots) and $|E'^{-}(z,t)|^2$ (red dots) in Fig. 6.6, as expected from the usual Dirac dynamics coupling the two components of the spinor. Most importantly, the frequency of the oscillation is changed by varying the two-photon detuning, which testifies to the coherent nature of the process (see Fig. 6.6a and b). We note that similar oscillations between SSL frequency components have been shown in previous studies [129]. However, in our implementation, the two spinor components correspond to different propagation directions, which is the key design element for engineering Dirac dynamics. In its essence, our implementation is closely related to the behaviors predicted to be observed in a highly correlated quantum gas of photons in 1-Dimensional nonlinear optical fibers [130]. In their proposal, two counter-propagating DSPs create a spatial Tripod DSP affected by a Kerr field while in our case two counter-propagating Tripod DSPs couple to each other and create the dynamics.

We benchmarked the aforementioned results against numerical solutions of the 1+1 dimensional Dirac equation of the form (including a coherence decay rate γ to account for losses in the real experiment):

$$i\partial_t \mathbf{\Psi} = \left(iv_g\sigma_z\partial_z + m_{eff_0}v_g^2\sigma_y - \gamma\right)\mathbf{\Psi},$$

with the initial condition $\mathbf{\Psi_0} = (\Psi_0^+, \Psi_0^-)$ extracted from the shape of the original SSL right after storage. The solid lines in Fig.6.6c and d represent the numerical simulation with fixed $v_g = 1.0cm/\mu s$, $m_{eff_0}v_g^2 = 3.3 * \delta$ and $\gamma = 0.3$. In this work, the magnetic field intensity has a lower and an upper band limit. To avoid creating any higher order DSP dynamics, the magnetic field needs to be large enough to remove one of the EIT lines from the intersection of the other two lines as it is demonstrated in Fig. 6.5a. Additionally, the field must remain small enough not to eliminate the cross-talk between m=-1 and m=0 EIT lines. As storage time is increased, the SSL components lose their mutual coherence, and thus the experimental data begins to deviate from the theoretical prediction. Nonetheless, these measurements provide strong evidence that the SSL dynamics follows that of relativistic particles. The main deviation from the numerical prediction happens as the control field coupling terms are not forming a perfect **Omega** as depicted in section 6.2.3. In this implementation, especially due to use of imperfect optical elements, the

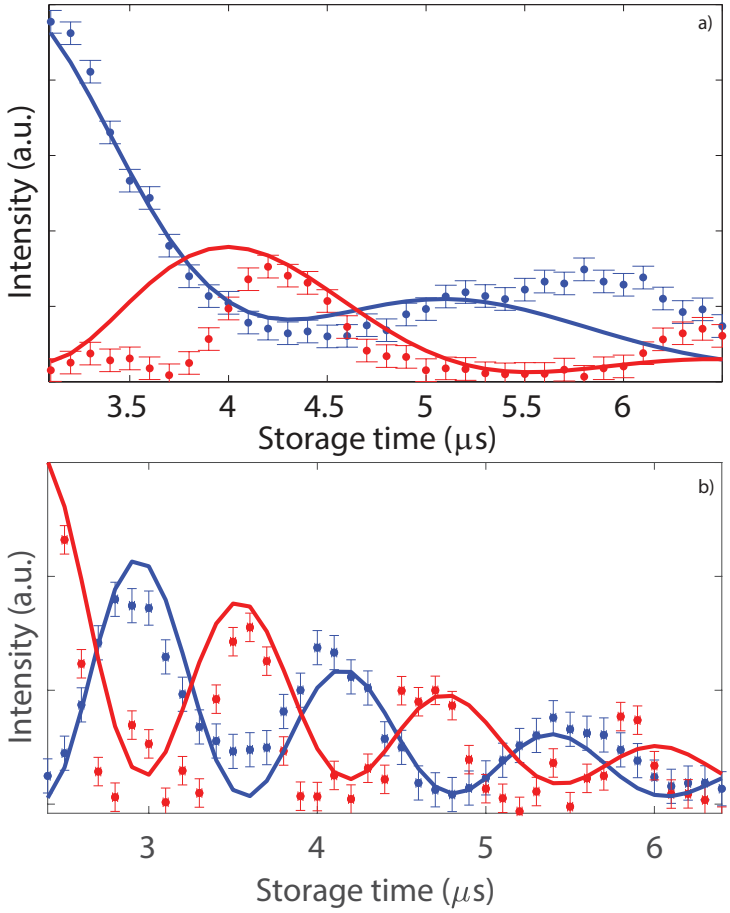

Figure 6.6: **Dirac dynamics using SSL.** Evaluating $|E^{\pm'}|^2$ for each τ results in an out of phase oscillation between the forward (blue dots) and backward (red dots) components of the SSLs. We plot the experimental data for $\delta = 350$kHz (a) and 700kHz (b). Solid lines in (a) and (b) corresponds to numerical solutions of the SSL Dirac equation (eq. 6.6).

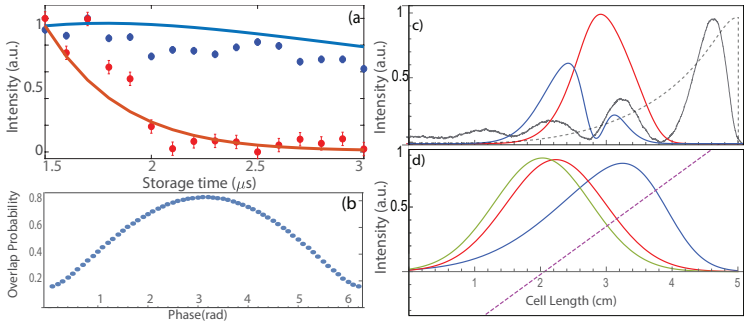

Figure 6.7: (a)Evaluating $|E^{\pm'}|^2$ for each τ for the JR experiment for the forward (blue dots) and backward (red dots) components of the SSLs. (b) Numerical estimation of the overlap of the phase based on experimental parameters. (c) Reconstructed temporal wave-functions for the different experiments. Coupled Dirac-Spinors oscillating(Red and Blue). Decaying uncoupled DSP (dotted line) (d) The spatial location of initial SSL components Ψ_0^+ (blue) and Ψ_0^- (red) together with $\phi(z)$ (green) in the cell. Magnetic gradient (purple). (c) $\int dz \mathbf{\Psi_0^\dagger} \psi_{zero}$ as a function of the phase between $\Psi^{+'}$ and $\Psi^{-'}$.

Omega is not symmetric. This results in higher order coupling terms which modulate additional oscillations, highlighted in Fig. 6.6.

6.3.4 Relativistic dynamics with topological behaviour.

Having built an analog Dirac simulator, we now move to mimic the JR model. To engineer $m_{eff}(z)$, we use a spatially varying magnetic field changing the two-photon detuning along the propagation axis of the light. Instead of the hyperbolic tangent function, we choose a linearly-varying mass profile, which is created by applying a linear magnetic field (purple line, Fig.6.7d) and perform experiments akin to our previous section. In this case, the zero-mode takes the form of a Gaussian (green line, Fig.6.7d). Figure 6.7a shows the obtained results.

This result has been benchmarked against a numerical solution of the modified Jackiw-Rebbi model with $\gamma = \begin{pmatrix} \gamma_1 & 0 \\ 0 & \gamma_2 \end{pmatrix}$ and $m_{eff}(z)v_g^2 \propto \delta = (0.745\frac{MHz}{cm}(z - 2.5cm) + 0.35MHz)$ The solid lines in Fig.6.7a (red and blue) represent the numerical solution with $\Phi = \pi$. The observed inhibition of oscillations is consistent with the initially occupied zero-mode [122], although the dynamics do not follow that of the JR model exactly because of the vastly different values of γ_1 and γ_2. This is because the two spinor components $\Psi^{+'}$ and $\Psi^{-'}$ couple to a magnetic field insensitive and a magnetic field sensitive EIT line,respectively (see Fig. 6.5a) [131]. This effect currently limits the

simulation time to about $2\mu s$. Even though this is enough time to observe the zero-energy mode, there are two approaches to increase the coherence time of the simulator. Following a similar physics, each tripod DSP can be created using two excited states corresponding to $87Rb$ D1 and D1 transition lines. Doing so allows the use of two central EIT lines (i.e., magnetic field insensitive lines) for both the forward and the backward components of the SSLs. Additionally, anti-relaxation coated vapor cells can be used to increase the effective coupling between the two modes by at least one order of magnitude as it was shown in [23]. Implementing both of these techniques will increase the coherence time of the simulator to above $50\mu s$.

As a further evidence of the initially occupied zero mode, we also calculate the overlap of the experimentally extracted $\mathbf{\Psi_0} = (\Psi_0^+, \Psi_0^-)$ (red and blue lines in Fig.6.7 a, measured at 1.5 μs storage time) with the zero-mode spinor: $\int dz \mathbf{\Psi_0^\dagger} \psi_{zero}$. In Fig. **??**b, we plot this overlap for different values of the global phase between the SSL components, Φ Noticeably, the best overlap of $\sim 80\%$ is also obtained for $\Phi = \pi$, which supports our claim that $\mathbf{\Psi_0}$ was prepared in the zero-mode.

6.4 Discussion

We have experimentally demonstrated the realization of a controllable coupling between two counter-propagating SSL components, simulating the dynamics of a relativistic massive fermion in a 1+1 Dirac equation. By adding a static background bosonic field (via the use of a magnetic field gradient), we have also simulated the celebrated Jackiw-Rebbi model. We have benchmarked our work with theoretical simulations by carefully reconstructing the initial SSL wave functions and using them in a numerical solution of the corresponding Dirac and JR differential equations. These values are then compared with the experimental data achieved by varying the storage time, showing an excellent correlation within the coherence time of the atoms. Lastly, we have also measured signatures of the JR zero-mode by observing the inhibition of the oscillation between the spinor components as predicted by the theory.

We consider our experiment to be an important first step towards more complex quantum simulations with many quantum relativistic particles. Possible extensions include the study of the Klein paradox [132] or the MIT bag model [133] by using coupled light-matter SSLs. Moreover, as slow light polaritons can be made to interact strongly, our work provides a pathway towards analog simulators of complex phenomena described by interacting quantum field theories. Possibilities include the simulation of: charge fractionalisation

in bosons[134], the interacting random Dirac model [135] and the renormalisation of mass due to interacting fermions [136]. Furthermore, interacting relativistic models such as the famous Thirring model [137] are now within experimental reach. As many of these important QFT predictions are only addressable using high energy experiments, this new breed of light-matter room temperature simulators will be an exciting tool to reach unexplored realms of physics.

6.5 Conclusion

In this chapter, I showed how we used our room-temperature light-matter interface to simulate the Dirac and Jacki-Rabiw models. We consider our experiment to be an essential first step towards more complex quantum simulations with many quantum relativistic particles. Adding interacting quantized modes from the double cavity node adds richness to the platform, that isn't available to competing platforms. This also enables connection through the network infrastructure we built, which might lead to distributed quantum simulators. In the next chapter, some of the groundwork to have interacting and nonlinear modes in the double cavity setup is presented.

Chapter 7

Towards double cavity-EIT

7.1 Introduction

As we've seen in the previous chapter once certain technical difficulties can be sorted out, we would be able to lock the cavities and measure vacuum Rabi splitting. The simulation shown at the end of Chapter 5 explains how the collective action will be used to enhance the single-atom coupling. This chapter will cover the road to measuring simultaneous double cavity interactions.

7.2 Double Cavity Simulation

For the simulation of two cavity coupling, the level diagram is shown in Fig.

We start with the following single atom, two photonic mode Hamiltonian:

$$H = H_{\text{atom}} + H_{\text{light}} + H_{\text{light-atom}} + H_{\text{driving field}} \tag{7.1}$$
$$H = (\Delta_A + \delta_A)\sigma_{11} \tag{7.2}$$
$$- \delta_A(a^\dagger a) - \delta_B(b^\dagger b) \tag{7.3}$$
$$+ g_A a\sigma_{12}^\dagger + g_A^* a^\dagger \sigma_{12} + g_B b\sigma_{12}^\dagger + g_B^* b^\dagger \sigma_{12} \tag{7.4}$$
$$+ E_A a + E_A^* a^\dagger + E_B b + E_B^* b^\dagger \tag{7.5}$$
$$\tag{7.6}$$

with the $\delta_{A,B}$ is the detuning between the probe-laser and Cavity A,B $\Delta_{A,B}$ is the cavity-atom detuning for Cavity A, B. $E_{A,B}$ is the normalized pulse strength of the coherent driving fields.

We simulated the non-linear response of the two cavities in the following way. Using codes that follow the same principles as [138], we numerically

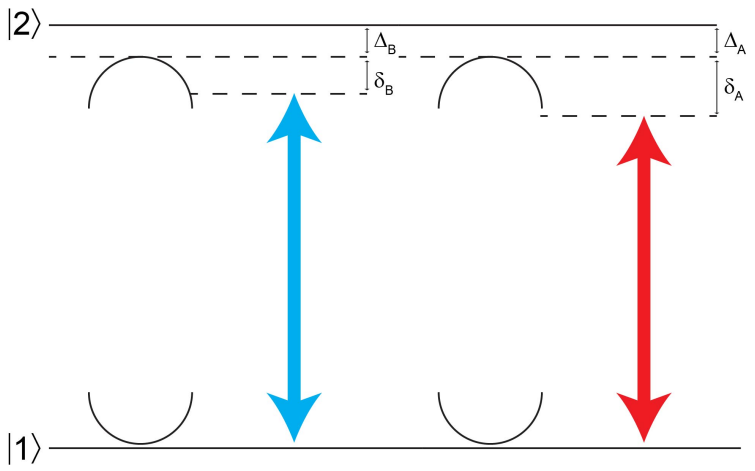

Figure 7.1:
Level Scheme of two VRS cavity simulations. $\delta_{A,B}$ is the detuning between the probe-laser and Cavity A,B $\Delta_{A,B}$. The curves represent the transition the cavity is coupled too and the blue (B) and red (A) represent the two coherent driving fields.

solve the Hamiltonian through the Lindblad formalism. The disipative terms that are included are cavity decay, atomic decay. The change in absorption and dispersion are found from the calculated density matrices. The master equation is

$$\begin{aligned}\dot{\rho} = &-i[H,\rho] + \kappa_A(2a\rho a^\dagger - a^\dagger a\rho - \rho a^\dagger a)\\ &+ \kappa_B(2b\rho b^\dagger - b^\dagger b\rho - \rho b^\dagger b\\ &+ \Gamma_{21}(2\sigma_{13}\rho\sigma_{13}^\dagger - \sigma_{22}\rho - \rho\sigma_{22})\\ &+ \gamma_{22}(2\sigma_{22}\rho\sigma_{22}^\dagger - \sigma_{22}\rho - \rho\sigma_{22})\end{aligned} \tag{7.7}$$

The dynamics are found by finding the steady-state dynamics $\dot{\rho} = 0$ for different values of probe-cavity detuning of Cavity A (δ_A).

In Fig. 7.2 an example of the results are shown. If Cavity B is detuned and the transmission is plotted for different values of probe-cavity detuning of Cavity A (δ_A), an asymmetric change in the Vacuum Rabi responses are seen.

The asymmetric AC stark shift given by a detuned cavity in the other cavity spectrum shows how one Fabry-Perot cavity influences the other and can be exploited for tunable cavity resonances.

One significant observation is how the light in Cavity B becomes absorbed close to these new resonances of Cavity A.

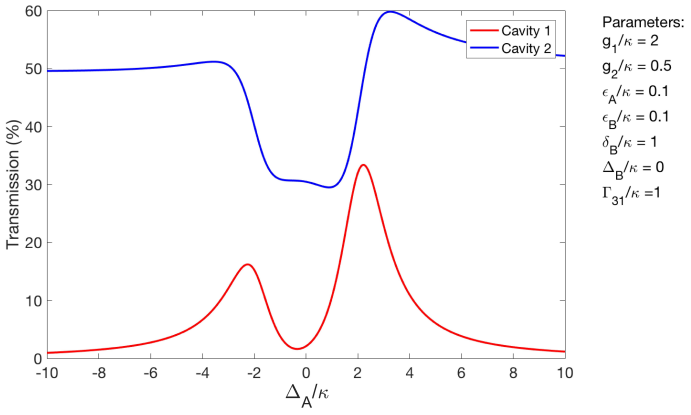

Figure 7.2: The normal mode splitting shown in both cavities. Only detuning of the one cavity is changed. The graph predicts a change in the symmetry of the VRS in that cavity mode and the new frequency dependence in the transmission in the other cavity.

7.3 Increasing interaction time

The important question that arrives with these systems are the different time-scales involved. The importance of time-scales is beautifully explained by Kimble [139]. The coherent transfer of the Hamiltonian between the atoms and cavities happen at g_A^{-1} and g_B^{-1}, while the incoherent decay out of the system happens at the time-scales of Γ^{-1} and κ_A^{-1} andκ_B^{-1}.

For the strong coupling regime where the goal is to have many coherent events before the photon decays out of the system, a strict requirement of having $g \gg \kappa, \Gamma$ is required.

However, since we are investigating a different part of the cooperativity parameter space, the relevant time-scale is the time that the same collective atomic coupling with collective g_N stays coupled to *both* cavities. This question will guide future investigations in this system.

The primary way we would like to proceed is by using the slow-light mechanism we have been very successful in, namely EIT.

By slowing down the light in the cavity, we believe the interaction time effectively increases.

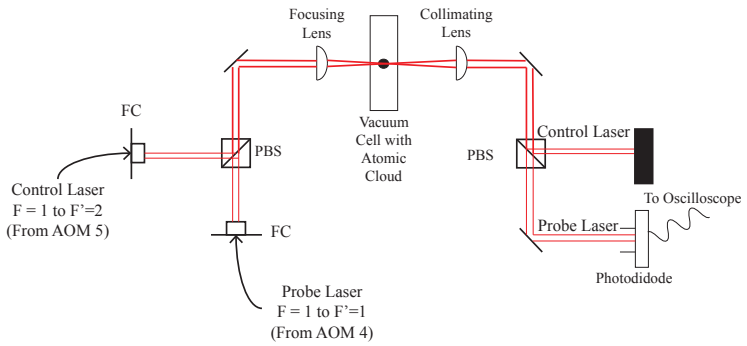

Figure 7.3: Experimental Set-up of MOT EIT. The control fields and probe fields were co-propagating in the MOT EIT experiments. Reproduced from [108]

7.4 Measuring EIT in MOT

Before adding the cavities to the MOT system, EIT experiments were done with the MOT alone. These results are extensively talked about in the thesis of Zak Burkley [108] and just a concise summary of the results will be presented here.

In Fig, 7.3 the experimental setup of a characterization of EIT is shown. The EIT control and probe fields are co-propagating through the vacuum cell. Two photodiodes are used to detect the two signal.

The pulse sequence of the first experiments is shown in Fig. 7.4. After the cooling fields are switched off an EIT peak is visible.

Different detunings of the probe give the graph in Fig. 7.5. The two peaks in the profile were found to be Zeeman level splitting due to stray magnetic fields. Using compensation coils, this was corrected as shown in Fig. 7.6.

Finding that a current of 1.5A gives only one peak, we can see that we are able to get EIT in our setup.

7.5 Double Cavity overlap measurements

7.6 Cavity EIT simulations

The results in the previous sections, gives confidence in simulating what can be seen when EIT is added to a two-cavity coupled system. The Hamiltonian is similar to before but the lasers are incident on different transitions and a

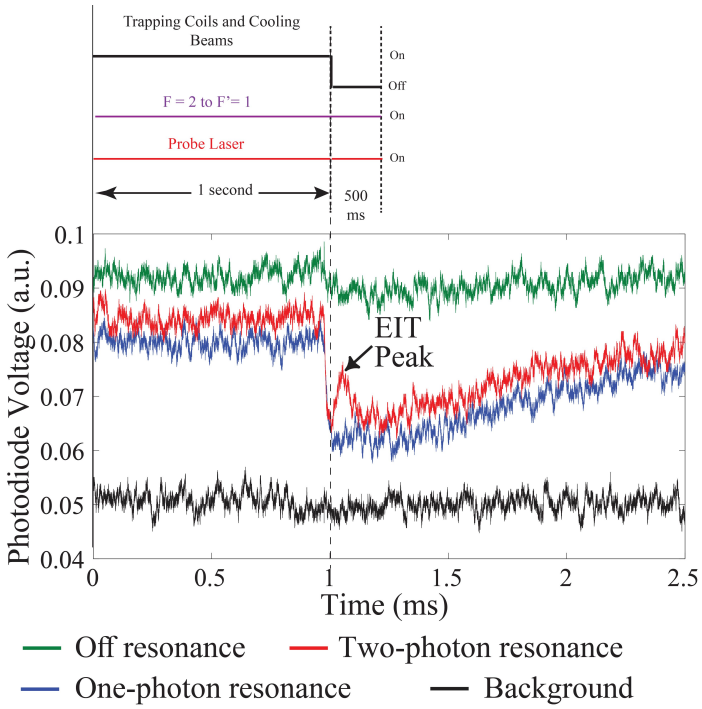

Figure 7.4: **EIT peak seen in MOT setup.** Pulse sequence shows how coils and cooling fields are switched off and afterwards a peak of transmission is seen. The difference between the blue and red traces shows the EIT transmission peak. Adapted from [108]

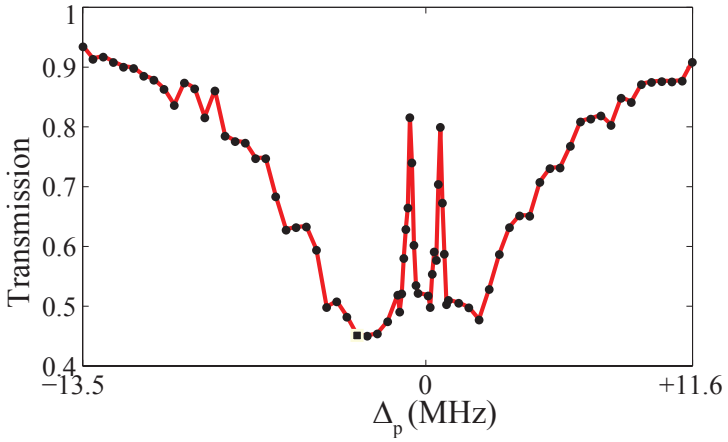

Figure 7.5: **EIT vs Probe Detuning**. Approximately 100 measurements of the kind in Fig. 7.4 is used to construct this graph for different probe detunings. Two absorption peaks are seen. Reproduced from [108]

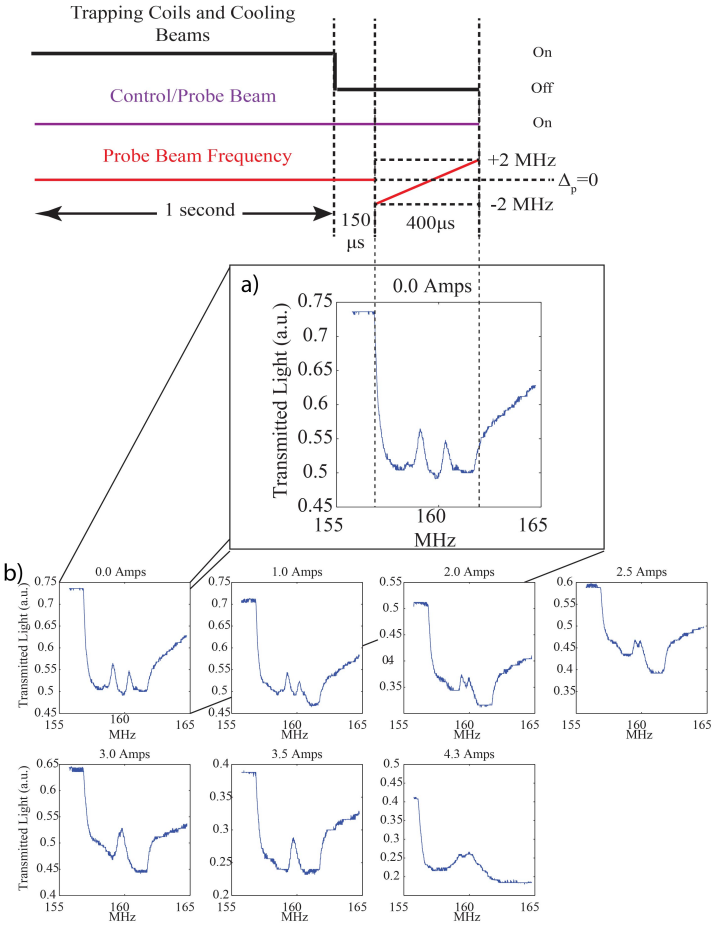

Figure 7.6: **Control of the EIT peaks using compensation coils.** a) Shows how the probe field was scanned in order to see EIT peaks. b) By applying extra magnetic fields Zeeman splitting effects are cancelled. Reproduced from [108].

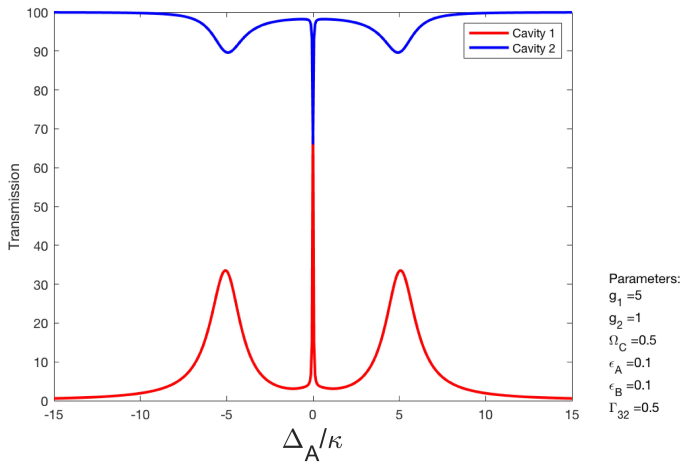

Figure 7.7: Result of simulating two cavity experiment with the EIT Hamiltonian.

control field is present.

$$H = H_{\text{atom}} + H_{\text{light}} + H_{\text{light-atom}} + H_{\text{driving field}} + H_{\text{Control field}} \tag{7.8}$$
$$H = (\Delta_A + \delta_A + \delta_C)\sigma_{11} + (\Delta_B + \delta_B)\sigma_{44} + \delta_C\sigma_{33} \tag{7.9}$$
$$- \delta_A(a^\dagger a) - \delta_B(b^\dagger b) \tag{7.10}$$
$$+ g_A a\sigma_{13}^\dagger + g_A^* a^\dagger\sigma_{13} + g_B b\sigma_{24}^\dagger + g_B^* b^\dagger\sigma_{24} \tag{7.11}$$
$$+ E_A a + E_A^* a^\dagger + E_B b + E_B^* b^\dagger \tag{7.12}$$
$$+ \Omega_C\sigma_{23} + \Omega_C^*\sigma_{23} \tag{7.13}$$

The cavity EIT spectrum shown in 7.7 show a dispersion engineering that can lead to phase shifts that are not given by the anharmonic latter of the cavity.

The graph only shows the detuning of the one cavity. The effect on the transmission of the second cavity indicates that there is a reversible change between the two atoms and resonators.

Moreover, the influence of a higher number of atoms should be considered and the impact of having the cavities crossed.

7.7 Current overlap measurement

7.7.1 Experimental Setup

Starting from the setup as described before, the only difference is that the two cavities had to be scanned in a way that was tractable to handle the overlap with software. The one cavity was scanned at 10Hz, the other at 100Hz and with similar amplitudes.

The two function generators were synchronized to two different channels in our pulse delay unit. This gave us the ability to get 200 pulses with 170 and on and 30 off and a wider gap in pulses for triggering.

The pulses were then measured using the SPCMs as before. The results were sent to a Matlab script that sorted the different triggering positions and then folded the slow horizontal peaks and on top of each other.

The positions of the smaller peaks were then identified to be relative to the slow-scanned peaks. The averages of the overlapping points and non-overlapping points were separately calculated.

7.7.2 Results

The results of this can be seen n in the figure 7.8. The red data points show the overlapped points, and the black points show no overlap. From these results, no effect of the overlap could be discerned.

7.8 Discussion

There are many possible reasons for this. Chiefly at that point was the strength of the vertical coupling. However, the geometric questions that were raised are illustrated in the following picture.

When considering the mutual coupling, one has to look at the overlap region in space that would be part of the experiment. The results very specifically depend on where the two beams intersect in the combination of the cloud.

Moreover, some atoms are only coupled to individual cavities. If this number of atoms are more than each other or a larger number than that of the ones that are doubly coupled, we cannot see what the output would be. Any effect of the overlap would be washed away by these effects. This idea is illustrated in Fig. 7.9.

To address this issues, a few strategies need to be followed.

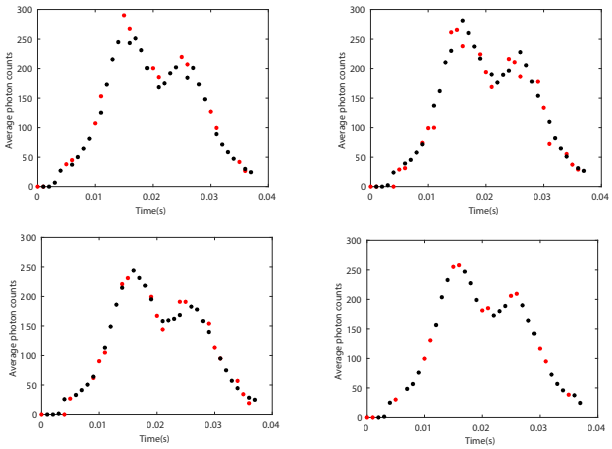

Figure 7.8: The null result of difference between overlapped (red) and nonoverlapped (black) points is showned in these graphs.

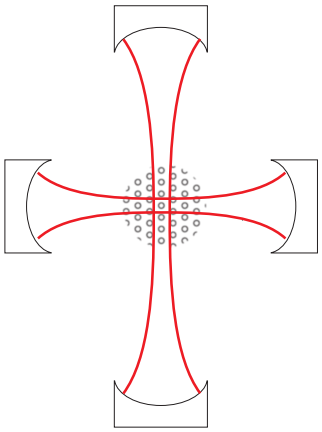

Figure 7.9: Not all atoms in the MOT will be coupled to both modes

More understanding of the nature of such a routing effect can be obtained doing some more simulation. Mainly, the type of scattering models that were presented in the previous chapter can be very illustrative, since they do not concern with the large Hilbert spaces that are required for the quantum treatment of the problem.

However, it would also be good to get some more experimental understanding to the question.

Chief among this would be to implement two-dimensional imaging of the MOT in which one can understand what happens to the atomic cloud when both standing waves are present. Using off-resonant light can increase this visibility.

Locking the two cavities will allow lower photon number experiments and better statistical analysis with post-selection.

7.9 Conclusion

In this chapter, I showed how using simple model Hamiltonians and numerical simulations we can predict effects for our double cavity system for s two-level system and a double cavity EIT system. EIT was realized in the MOT. Measurement of simultaneous cavity probing was taken. All of these show that we are on our way to measure experimental results to test the impact of double cavity EIT. In the final chapter, a more long-term vision will be presented to wrap-up all the parts of the thesis.

Chapter 8

Outlook

The pinnacle of this thesis was the experimental results of the world's first magneto-optically trapped ensemble atoms coupled to two crossed optical resonators in Chapter 5. This new type of interface will open many different avenues of research for the fundamental understanding of atom-cavity coupling, quantum simulation, non-linear interactions, and quantum simulation. In the near future, we can expect to use the bi-directionality of the interface between it and our memories for it to act as a new kind of light source [54, 111, 140], characterize it with csQPT (Chapter 3) and investigate non-linear interactions (Chapter 7). Once nonlinearities can be manipulated, we can extend our work on quantum simulation (Chapter 6) and examine models such as the Thirring model [141]. In the long run, these improvements in the cross-cavity node and the quantum memory infrastructure I helped develop (Chapter 2), will help propel quantum network technologies from the lab-based systems available today, towards small, scalable functional quantum networks.

Many different research questions need to be answered to achieve these goals. Some new and interesting problems involving maximizing the number of atoms that are simultaneously coupled still need to be solved. Moreover, the resulting some interactions need to be characterized and compared to theory, and I believe some fascinating question regarding cavity-atom coupling can be understood better [114, 99].

A large part of the thesis described the design and building of the atomic and optical elements of the double cavity experiment. Many technical difficulties remain, chief of which is the cavity locking and multiple dimensional imaging. As with any new technology, solving these problems will lead to innovative new solutions that can be used in other areas.

Furthermore, our focus on quantum networks compels us to connect our cross-cavity node to our quantum memories. In the near term, this can be done

in different ways as shown in 1.2 in Chapter 1. Our confidence in connecting our devices comes from how, in Chapter 2, I explained how our memories achieved $> 90\%$ fidelity and exhibited shot-by-shot operation for random polarization state, over a 20m free-space link [55].

One idea would be to combine many elements presented and set up experiments such as the one shown in Fig. 8.1. Here the quantum simulation platform of Slow Light Spinors (Chapter 6), combined with sources that create quantized modes of light and interact with the cross-cavity system through engineered interactions (Chapter 7). The results are analyzed using homodyne detection (Chapter 3) the extension of the csQPT research toward more that one mode has already started and combines new technologies such as machine-learning and high-performance parallelization. The simplicity and robustness or this characterization procedure would make it ideal for the facilitation of practical quantum optical gates into future networks and provide a universal tool for the characterization of multi-state quantum components.

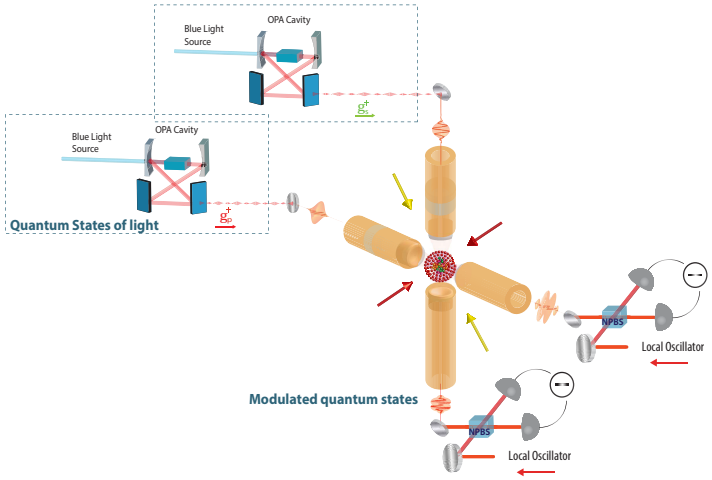

Figure 8.1: Experiment combining components shown in thesis. The double cavity experiment is shown (Chapters 4,5 and 7). The simulation protocol is the same as Chapter 6. The homodyne detection will follow the work shown in Chapter 3.

We have started using SSL to simulate the Dirac and Jacki-Rabiw models which we hope will lead to quantum simulations of many relativistic quantum particles. The Thirring model can be simulated by a system in which nonlinearities can be generated to mimic interactions between bosons [141]. Even though our current system only allows for Fermi interactions between two particles at a time, you can imagine that connecting more that one quan-

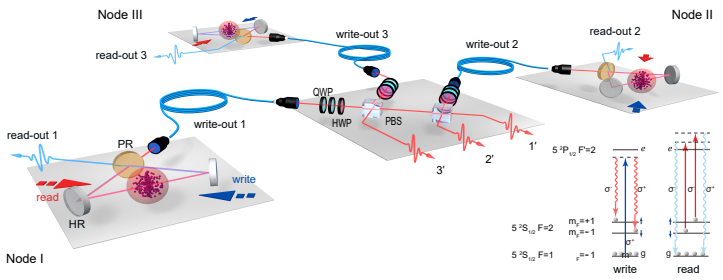

Figure 8.2: State of the art hybrid memory-photon experiment. Four light-matter interfaces are shown. Picture from [140]

tum simulator we can create a statistical sample and do experiments that more closely represent practical many-body systems. An exciting intermediate way to do this, before more than one simulation node exists, is to store the result of the first experiment in a quantum memory and discretize the simulation.

The other direction is using the cross-cavity node as a photon source using the well-known DLCZ protocol [54, 111, 140]. Currently, the is the state of the art system that uses cavity enhanced DLCZ photons is shown in Fig. 8.2 reproduced from [140]. It is being used to entangled three photons, an essential resource in photonic quantum network proposals [140, 142].

This system has **three (3)** quantum light-matter interfaces.

In photographs, the devices that were presented in this thesis and that I have helped create are shown in Fig. 8.3. If one counts the number of quantum light interfaces, considering that each quantum memory uses a dual-rail setup to store polarization, ends up to be **six (6)**. Double the current state of the art!

In just five years, our room-temperature quantum memories have reached ultra-low noise operation [23]. This gives me the confidence to predict that in the next few years, by using cavity enhancement from our cross-cavity experiment, and interfacing with our room-temperature quantum memories, our system will be able to compete with systems with significantly more technical overhead.

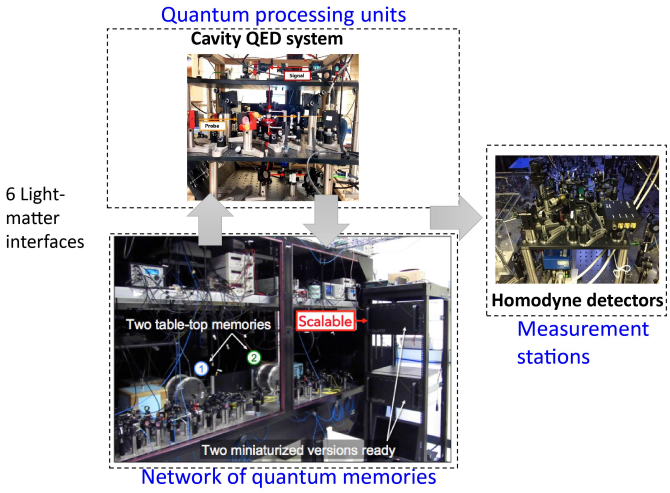

Figure 8.3: In our lab if counted for each rail, the memories account for 4 light-matter interfaces. The double cavity node accounts for 2. This presents a network that should be interconnect in a few years of 6 light-matter interfaces.

Chapter 9

Bibliography

[1] Brunner, N., Cavalcanti, D., Pironio, S., Scarani, V., and Wehner, S., *Bell nonlocality*, Rev. Mod. Phys. **86**, 419 (2014).

[2] Reiserer, A. and Rempe, G., *Cavity-based quantum networks with single atoms and optical photons*, Rev. Mod. Phys. **87**, 1379 (2015).

[3] Castelvecchi, D., *The quantum internet has arrived (and it hasn't).*, Nature **554**, 289 (2018).

[4] Kimble, H. J., *The quantum internet*, Nature **453**, 1023 (2008).

[5] Bennett, C. H., Brassard, G., and Ekert, A. K., *Quantum Cryptography*, Scientific American **267**, 50 (1992).

[6] Shalm, L. K., Meyer-Scott, E., Christensen, B. G., Bierhorst, P., Wayne, M. A., Stevens, M. J., Gerrits, T., Glancy, S., Hamel, D. R., Allman, M. S., Coakley, K. J., Dyer, S. D., Hodge, C., Lita, A. E., Verma, V. B., Lambrocco, C., Tortorici, E., Migdall, A. L., Zhang, Y., Kumor, D. R., Farr, W. H., Marsili, F., Shaw, M. D., Stern, J. A., Abellán, C., Amaya, W., Pruneri, V., Jennewein, T., Mitchell, M. W., Kwiat, P. G., Bienfang, J. C., Mirin, R. P., Knill, E., and Nam, S. W., *Strong loophole-free test of local realism*, Phys. Rev. Lett. **115**, 250402 (2015).

[7] Hensen, B., Bernien, H., Drau, A. E., Reiserer, A., Kalb, N., Blok, M. S., Ruitenberg, J., Vermeulen, R. F. L., Schouten, R. N., Abelln, C., Amaya, W., Pruneri, V., Mitchell, M. W., Markham, M., Twitchen, D. J., Elkouss, D., Wehner, S., Taminiau, T. H., and Hanson, R., *Loophole-free bell inequality violation using electron spins separated by 1.3 kilometres*, Nature **526**, 682 (2015).

[8] Giustina, M., Versteegh, M., Wengerowsky, S., Hochrainer, J. H. A., Phelan, K., Steinlechner, F., Kofler, J., Larsson, J.-A., Abellan, C., Amaya, W., Pruneri, V., Mitchell, M. W., Beyer, J., Gerrits, T., Lita, A., Shalm, L. K., Nam, S. W., Scheidl, T., Ursin, R., Wittmann, B., and Zeilinger, A., *A significant-loophole-free test of bell's theorem with entangled photons*, Phys. Rev. Lett. **115**, 250401 (2015).

[9] Yin, J., Cao, Y., Li, Y.-H., Liao, S.-K., Zhang, L., Ren, J.-G., Cai, W.-Q., Liu, W.-Y., Li, B., Dai, H., Li, G.-B., Lu, Q.-M., Gong, Y.-H., Xu, Y., Li, S.-L., Li, F.-Z., Yin, Y.-Y., Jiang, Z.-Q., Li, M., Jia, J.-J., Ren, G., He, D., Zhou, Y.-L., Zhang, X.-X., Wang, N., Chang, X., Zhu, Z.-C., Liu, N.-L., Chen, Y.-A., Lu, C.-Y., Shu, R., Peng, C.-Z., Wang, J.-Y., and Pan, J.-W., *Satellite-based entanglement distribution over 1200 kilometers*, Science **356**, 1140 (2017).

[10] Abbott, B. P. e. a., *Observation of gravitational waves from a binary black hole merger*, Phys. Rev. Lett. **116**, 061102 (2016).

[11] Scarani, V., Bechmann-Pasquinucci, H., Cerf, N. J., Dušek, M., Lütkenhaus, N., and Peev, M., *The security of practical quantum key distribution*, Rev. Mod. Phys. **81**, 1301 (2009).

[12] Lo, H.-K., Curty, M., and Qi, B., *Measurement-device-independent quantum key distribution*, Phys. Rev. Lett. **108**, 130503 (2012).

[13] Bacco, D., Canale, M., Laurenti, N., Vallone, G., and Villoresi, P., *Experimental quantum key distribution with finite-key security analysis for noisy channels*, Nat Commun **4**, 2363 (2013).

[14] Liu, Y., Chen, T.-Y., Wang, L.-J., Liang, H., Shentu, G.-L., Wang, J., Cui, K., Yin, H.-L., Liu, N.-L., Li, L., Ma, X., Pelc, J. S., Fejer, M. M., Peng, C.-Z., Zhang, Q., and Pan, J.-W., *Experimental measurement-device-independent quantum key distribution*, Phys. Rev. Lett. **111**, 130502 (2013).

[15] Tang, Z., Liao, Z., Xu, F., Qi, B., Qian, L., and Lo, H.-K., *Experimental Demonstration of Polarization Encoding Measurement-Device-Independent Quantum Key Distribution*, Phys. Rev. Lett. **112**, 190503 (2014).

[16] Abruzzo, S., Kampermann, H., and Bruß, D., *Measurement-device-independent quantum key distribution with quantum memories*, Phys. Rev. A **89**, 012301 (2014).

[17] Panayi, C., Razavi, M., Ma, X., and Lütkenhaus, N., *Memory-assisted measurement-device-independent quantum key distribution*, New Journal of Physics **16**, 043005 (2014).

[18] Vallone, G., Dequal, D., Tomasin, M., Vedovato, F., Schiavon, M., Luceri, V., Bianco, G., and Villoresi, P., *Interference at the Single Photon Level Along Satellite-Ground Channels*, Phys. Rev. Lett. **116**, 253601 (2016).

[19] Panayi, C., Razavi, M., Ma, X., and Lütkenhaus, N., *Memory-assisted measurement-device-independent quantum key distribution*, New J. Phys. **16**, 043005 (2014).

[20] Abruzzo, S., Kampermann, H., and Bruß, D., *Measurement-device-independent quantum key distribution with quantum memories*, Phys. Rev. A **89**, 012301 (2014).

[21] Briegel, H.-J., Dür, W., Cirac, J. I., and Zoller, P., *Quantum Repeaters: The Role of Imperfect Local Operations in Quantum Communication*, Physical Review Letters **81**, 5932 (1998).

[22] Dür, W., Briegel, H.-J., Cirac, J. I., and Zoller, P., *Quantum repeaters based on entanglement purification*, Physical Review A **59**, 169 (1999).

[23] Namazi, M., Kupchak, C., Jordaan, B., Shahrokhshahi, R., and Figueroa, E., *Ultralow-noise room-temperature quantum memory for polarization qubits*, Phys. Rev. Applied **8**, 034023 (2017).

[24] Namazi, M., Mittiga, T., Kupchak, C., and Figueroa, E., *Cascading quantum light-matter interfaces with minimal interconnection losses*, Phys. Rev. A **92**, 033846 (2015).

[25] Kupchak, C., Rind, S., Jordaan, B., and Figueroa, E., *Quantum process tomography of an optically-controlled kerr non-linearity*, Scientific Reports **5**, 16581 EP (2015).

[26] Laurat, J., *On-demand entanglement could lead to scalable quantum networks.* (2018).

[27] Reiserer, A., Kalb, N., Rempe, G., and Ritter, S., *A quantum gate between a flying optical photon and a single trapped atom*, Nature **508**, 237 (2014).

[28] Hacker, B., Welte, S., Rempe, G., and Ritter, S., *A photon–photon quantum gate based on a single atom in an optical resonator*, Nature **536**, 193 (2016).

[29] Schindler, P., Barreiro, J. T., Monz, T., Nebendahl, V., Nigg, D., Chwalla, M., Hennrich, M., and Blatt, R., *Experimental repetitive quantum error correction*, Science **332**, 1059 (2011).

[30] Riordan, M., Hoddeson, L., and Herring, C., *The invention of the transistor*, Rev. Mod. Phys. **71**, S336 (1999).

[31] Kok, P. and Lovett, B. W., *Introduction to Optical Quantum Information Processing*, Cambridge University Press (2010).

[32] Metcalf, H. and van der Straten, P., *Laser Cooling and Trapping.*, Springer New York (2001).

[33] Fleischhauer, M., Imamoglu, A., and Marangos, J. P., *Electromagnetically induced transparency: Optics in coherent media*, Reviews of modern physics **77**, 633 (2005).

[34] Akibue, S. and Murao, M., *Network coding for distributed quantum computation over cluster and butterfly networks*, IEEE Transactions on Information Theory **62**, 6620 (2016).

[35] Leung, D., Oppenheim, J., and Winter, A., *Quantum network communicationthe butterfly and beyond*, IEEE Transactions on Information Theory **56**, 3478 (2010).

[36] Tanji-Suzuki, H., Chen, W., Landig, R., Simon, J., and Vuletić, V., *Vacuum-induced transparency*, Science **333**, 1266 (2011).

[37] Bouwmeester, D., Ekert, A., and Zeilinger, A., editors, *The Physics of Quantum Information*, Springer Berlin Heidelberg, Berlin, Heidelberg (2000), ISBN 978-3-642-08607-6 978-3-662-04209-0.

[38] Fleischhauer, M. and Lukin, M. D., *Dark-State Polaritons in Electromagnetically Induced Transparency*, Physical Review Letters **84**, 5094 (2000).

[39] Lawrence, J., Brukner, i. c. v., and Zeilinger, A., *Mutually unbiased binary observable sets on n qubits*, Phys. Rev. A **65**, 032320 (2002).

[40] Altepeter, J. B., James, D. F. V., and Kwiat, P. G., *Quantum State Estimation. Lecture Notes in Physics.*, Springer, Berlin. (2004).

[41] Altepeter, J., Jeffrey, E., and Kwiat, P., *Photonic state tomography*, Adv. in Atom. Mol. and Opt. Phys **52**, 105 (2005).

[42] Kupchak, C., Mittiga, T., Jordaan, B., Namazi, M., Nölleke, C., and Figueroa, E., *Room-temperature single-photon level memory for polarization states*, Scientific Reports **5**, 7658 EP (2015).

[43] Specht, H. P., Nölleke, C., Reiserer, A., Uphoff, M., Figueroa, E., Ritter, S., and Rempe, G., *A single-atom quantum memory*, Nature **473**, 190 (2011).

[44] Gündoğan, M., Ledingham, P. M., Almasi, A., Cristiani, M., and de Riedmatten, H., *Quantum storage of a photonic polarization qubit in a solid*, Phys. Rev. Lett. **108**, 190504 (2012).

[45] Phillips, N. B., Gorshkov, A. V., and Novikova, I., *Light storage in an optically thick atomic ensemble under conditions of electromagnetically induced transparency and four-wave mixing*, Phys. Rev. A **83**, 063823 (2011).

[46] Lauk, N., O'Brien, C., and Fleischhauer, M., *Fidelity of photon propagation in electromagnetically induced transparency in the presence of four-wave mixing*, Phys. Rev. A **88**, 013823 (2013).

[47] Karpa, L., Vewinger, F., and Weitz, M., *Resonance Beating of Light Stored Using Atomic Spinor Polaritons*, Physical Review Letters **101**, 170406 (2008).

[48] Riedl, S., Lettner, M., Vo, C., Baur, S., Rempe, G., and Dürr, S., *Bose-Einstein condensate as a quantum memory for a photonic polarization qubit*, Physical Review A **85**, 022318 (2012).

[49] Cirac, J. I., Zoller, P., Kimble, H. J., and Mabuchi, H., *Quantum state transfer and entanglement distribution among distant nodes in a quantum network*, Phys. Rev. Lett. **78**, 3221 (1997).

[50] Datta, A., Zhang, L., Nunn, J., Langford, N. K., Feito, A., Plenio, M. B., and Walmsley, I. A., *Compact Continuous-Variable Entanglement Distillation*, Phys. Rev. Lett. **108**, 060502 (2012).

[51] Kómár, P., Kessler, E. M., Bishof, M., Jiang, L., Sørensen, A. S., Ye, J., and Lukin, M. D., *A quantum network of clocks*, Nat. Phys. **10**, 582 (2014).

[52] Reiserer, A., Kalb, N., Blok, M. S., van Bemmelen, K. J. M., Taminiau, T. H., Hanson, R., Twitchen, D. J., and Markham, M., *Robust quantum-network memory using decoherence-protected subspaces of nuclear spins*, Phys. Rev. X **6**, 021040 (2016).

[53] Bussières, F., Clausen, C., Tiranov, A., Korzh, B., Verma, V. B., Nam, S. W., Marsili, F., Ferrier, A., Goldner, P., Herrmann, H., Silberhorn, C., Sohler, W., Afzelius, M., and Gisin, N., *Quantum teleportation from a telecom-wavelength photon to a solid-state quantum memory*, Nat. Photonics **8**, 775 (2014).

[54] Duan, L.-M., Lukin, M. D., Cirac, J. I., and Zoller, P., *Long-distance quantum communication with atomic ensembles and linear optics*, Nature **414**, 413 (2001).

[55] Namazi, M., Vallone, G., Jordaan, B., Goham, C., Shahrokhshahi, R., Villoresi, P., and Figueroa, E., *Free-Space Quantum Communication with a Portable Quantum Memory*, Physical Review Applied **8**, 064013 (2017).

[56] Bennett, C. H. and Brassard, G., *Quantum Cryptography: Public Key Distribution and Coin Tossing*, in *Proceedings of the IEEE International Conference on Computers, Systems and Signal Processing, Bangalore, India*, 175, IEEE, New York (1984).

[57] Elkouss, D., Martinez-Mateo, J., and Martin, V., *Information Reconciliation for Quantum Key Distribution*, Quantum Inf. Comput. **11**, 0226 (2011).

[58] Schweickert, L., Jöns, K. D., Namazi, M., Cui, G., Lettner, T., Zeuner, K. D., Scavuzzo Montaña, L., Filipe Covre da Silva, S., Reindl, M., Huang, H., Trotta, R., Rastelli, A., Zwiller, V., and Figueroa, E., *Electromagnetically Induced Transparency of On-demand Single Photons in a Hybrid Quantum Network*, arXiv e-prints arXiv:1808.05921 (2018).

[59] Feizpour, A., Hallaji, M., Dmochowski, G., and Steinberg, A. M., *Observation of the nonlinear phase shift due to single post-selected photons*, Nat Phys **11**, 905 (2015).

[60] Distante, E., Farrera, P., Padrn-Brito, A., Paredes-Barato, D., Heinze, G., and de Riedmatten, H., *Storing single photons emitted by a quantum memory on a highly excited Rydberg state*, Nat Commun **8**, 14072 (2017).

[61] Distante, E., Padrn-Brito, A., Cristiani, M., Paredes-Barato, D., and de Riedmatten, H., *Storage Enhanced Nonlinearities in a Cold Atomic Rydberg Ensemble*, Physical Review Letters **117**, 113001 (2016).

[62] Lobino, M., Korystov, D., Kupchak, C., Figueroa, E., Sanders, B. C., and Lvovsky, A. I., *Complete characterization of quantum-optical processes*, Science **322**, 563 (2008).

[63] Lobino, M., Kupchak, C., Figueroa, E., and Lvovsky, A. I., *Memory for light as a quantum process*, Phys. Rev. Lett. **102**, 203601 (2009).

[64] Anis, A. and Lvovsky, A. I., *Maximum-likelihood coherent-state quantum process tomography*, New Journal of Physics **14**, 105021 (2012).

[65] Chang, D. E., Vuletic, V., and Lukin, M. D., *Quantum nonlinear optics [mdash] photon by photon*, Nat Photon **8**, 685 (2014).

[66] Braunstein, S. L. and Pati, A. K., *Quantum Information with Continuous Variables*, Kluwer Academic (2003).

[67] Peyronel, T., Firstenberg, O., Liang, Q.-Y., Hofferberth, S., Gorshkov, A. V., Pohl, T., Lukin, M. D., and Vuletic, V., *Quantum nonlinear optics with single photons enabled by strongly interacting atoms*, Nature **488**, 57 (2012).

[68] Firstenberg, O., Peyronel, T., Liang, Q.-Y., Gorshkov, A. V., Lukin, M. D., and Vuletic, V., *Attractive photons in a quantum nonlinear medium*, Nature **502**, 71 (2013).

[69] Chen, W., Beck, K. M., Bücker, R., Gullans, M., Lukin, M. D., Tanji-Suzuki, H., and Vuletić, V., *All-optical switch and transistor gated by one stored photon*, Science **341**, 768 (2013).

[70] Tiecke, T. G., Thompson, J. D., de Leon, N. P., Liu, L. R., Vuletic, V., and Lukin, M. D., *Nanophotonic quantum phase switch with a single atom*, Nature **508**, 241 (2014).

[71] Volz, J., Scheucher, M., Junge, C., and Rauschenbeutel, A., *Nonlinear [pi] phase shift for single fibre-guided photons interacting with a single resonator-enhanced atom*, Nat Photon **8**, 965 (2014).

[72] Imamoḡlu, A., Schmidt, H., Woods, G., and Deutsch, M., *Strongly interacting photons in a nonlinear cavity*, Phys. Rev. Lett. **79**, 1467 (1997).

[73] Kang, H. and Zhu, Y., *Observation of large kerr nonlinearity at low light intensities*, Phys. Rev. Lett. **91**, 093601 (2003).

[74] Bajcsy, M., Hofferberth, S., Balic, V., Peyronel, T., Hafezi, M., Zibrov, A. S., Vuletic, V., and Lukin, M. D., *Efficient all-optical switching using slow light within a hollow fiber*, Phys. Rev. Lett. **102**, 203902 (2009).

[75] Chen, Y.-F., Wang, C.-Y., Wang, S.-H., and Yu, I. A., *Low-light-level cross-phase-modulation based on stored light pulses*, Phys. Rev. Lett. **96**, 043603 (2006).

[76] Lo, H.-Y., Chen, Y.-C., Su, P.-C., Chen, H.-C., Chen, J.-X., Chen, Y.-C., Yu, I. A., and Chen, Y.-F., *Electromagnetically-induced-transparency-based cross-phase-modulation at attojoule levels*, Phys. Rev. A **83**, 041804 (2011).

[77] Hosseini, M., Rebic, S., Sparkes, B. M., Twamley, J., Buchler, B. C., and Lam, P. K., *Memory-enhanced noiseless cross-phase modulation*, Light Sci Appl **1**, e40 (2012).

[78] Shapiro, J. H., *Single-photon kerr nonlinearities do not help quantum computation*, Phys. Rev. A **73**, 062305 (2006).

[79] Gea-Banacloche, J., *Impossibility of large phase shifts via the giant kerr effect with single-photon wave packets*, Phys. Rev. A **81**, 043823 (2010).

[80] Pack, M. V., Camacho, R. M., and Howell, J. C., *Transients of the electromagnetically-induced-transparency-enhanced refractive kerr nonlinearity: Theory*, Phys. Rev. A **74**, 013812 (2006).

[81] Pack, M. V., Camacho, R. M., and Howell, J. C., *Transients of the electromagnetically-induced-transparency-enhanced refractive kerr nonlinearity*, Phys. Rev. A **76**, 033835 (2007).

[82] Li, R. B., Deng, L., and Hagley, E. W., *Fast, all-optical, zero to π continuously controllable kerr phase gate*, Phys. Rev. Lett. **110**, 113902 (2013).

[83] Zhu, C., Deng, L., and Hagley, E. W., *Polarization-selective kerr-phase-shift method for fast, all-optical polarization switching in a cold atomic medium*, Phys. Rev. A **90**, 063841 (2014).

[84] Li, R. B., Deng, L., and Hagley, E. W., *Fast, all-optical logic gates and transistor functionalities using a room-temperature atomic controlled kerr gate*, Phys. Rev. A **90**, 063806 (2014).

[85] Imamoḡlu, A., Schmidt, H., Woods, G., and Deutsch, M., *Strongly interacting photons in a nonlinear cavity*, Phys. Rev. Lett. **79**, 1467 (1997).

[86] Lvovsky, A. I. and Raymer, M. G., *Continuous-variable optical quantum-state tomography*, Rev. Mod. Phys. **81**, 299 (2009).

[87] Lvovsky, A. I., *Iterative maximum-likelihood reconstruction in quantum homodyne tomography*, Journal of Optics B: Quantum and Semiclassical Optics **6**, S556 (2004).

[88] Leonhardt, U., *Measuring the quantum state of light*, Cambridge University Press (1997).

[89] Kumar, R., Barrios, E., Kupchak, C., and Lvovsky, A. I., *Experimental characterization of bosonic creation and annihilation operators*, Phys. Rev. Lett. **110**, 130403 (2013).

[90] Fedorov, I. A., Fedorov, A. K., Kurochkin, Y. V., and Lvovsky, A. I., *Tomography of a multimode quantum black box*, New Journal of Physics **17**, 043063 (2015).

[91] Jamiołkowski, A., *Linear transformations which preserve trace and positive semidefiniteness of operators*, Reports on Mathematical Physics **3**, 275 (1972).

[92] Cooper, M., Slade, E., KarpiÅski, M., and Smith, B. J., *Characterization of conditional state-engineering quantum processes by coherent state quantum process tomography*, New Journal of Physics **17**, 033041 (2015).

[93] Shahrokhshahi, R., Sagona-Stophel, S., Jordaan, B., Namazi, M., and Figueroa, E., *Room temperature conditional π-phase shifts mediated by simultaneously propagating single-photon level pulses*, arXiv e-prints arXiv:1803.07012 (2018).

[94] Beck, K. M., Hosseini, M., Duan, Y., and Vuletić, V., *Large conditional single-photon cross-phase modulation*, Proceedings of the National Academy of Sciences **113**, 9740 (2016).

[95] Uphoff, M., Brekenfeld, M., Rempe, G., and Ritter, S., *An integrated quantum repeater at telecom wavelength with single atoms in optical fiber cavities*, Applied Physics B **122**, 46 (2016).

[96] Nguyen, C. H., Utama, A. N., Lewty, N., Durak, K., Maslennikov, G., Straupe, S., Steiner, M., and Kurtsiefer, C., *Single atoms coupled to a near-concentric cavity*, Phys. Rev. A **96**, 031802 (2017).

[97] Wu, H., Gea-Banacloche, J., and Xiao, M., *Observation of intracavity electromagnetically induced transparency and polariton resonances in a doppler-broadened medium*, Phys. Rev. Lett. **100**, 173602 (2008).

[98] Ray, T., Sharma, A., Jyothi, S., and Rangwala, S. A., *Temperature measurement of laser-cooled atoms using vacuum rabi splitting*, Phys. Rev. A **87**, 033832 (2013).

[99] Tanji-Suzuki, H., Leroux, I. D., Schleier-Smith, M. H., Cetina, M., Grier, A. T., Simon, J., and Vuleti, V., *Interaction between Atomic Ensembles and Optical Resonators*, in *Advances In Atomic, Molecular, and Optical Physics*, volume 60, 201–237, Elsevier (2011), ISBN 978-0-12-385508-4.

[100] Corder, C., Arnold, B., and Metcalf, H., *Laser cooling without spontaneous emission*, Phys. Rev. Lett. **114**, 043002 (2015).

[101] Kurpiers, P., Magnard, P., Walter, T., Royer, B., Pechal, M., Heinsoo, J., Salath, Y., Akin, A., Storz, S., Besse, J.-C., Gasparinetti, S., Blais, A., and Wallraff, A., *Deterministic quantum state transfer and remote entanglement using microwave photons*, Nature **558**, 264 (2018).

[102] Phillips, W. D. and Metcalf, H., *Laser deceleration of an atomic beam.*, Physical Review Letters 48 **9**, 59699 (1982).

[103] Chu, S., Hollberg, L., Bjorkholm, J. E., Cable, A., and Ashkin, A., *Three-dimensional viscous confinement and cooling of atoms by resonance radiation pressure.*, Physical Review Letters **55**, 48 (1985).

[104] Metcalf, H. J. and van der Straten, P., *Laser Cooling and Trapping*, Graduate Texts in Contemporary Physics, Springer, New York (2001).

[105] Raab, E. L., Prentiss, M., Cable, A., Chu, S., and Pritchard, D. E., *Trapping of neutral sodium atoms with radiation pressure.*, Physical Review Letters **59**, 263134 (1987).

[106] Ianzano, C., *Towards Dual Cavity Resonance in a Rubidium Ensemble*, Master's thesis, Stony Brook University (2018).

[107] Steck, D. A., *Rubidium 87 d line data* (2015).

[108] Burkley, Z. N., *Towards Single Photon Nonlinearities Using Cavity EIT.*, Master's thesis, Stony Brook University (2014).

[109] G, H., *Fabry-Perot Interferometers*, Cambridge University Press (1988).

[110] Goy, P., Raimond, J. M., Gross, M., and Haroche, S., *Observation of cavity-enhanced single-atom spontaneous emission.*, Phys. Rev Lett. **50**, 19031906 (1983).

[111] Simon, J., Tanji, H., Thompson, J. K., and Vuletić, V., *Interfacing collective atomic excitations and single photons*, Phys. Rev. Lett. **98**, 183601 (2007).

[112] Agarwal, G. S., *Vacuum-field rabi splittings in microwave absorption by rydberg atoms in a cavity*, Phys. Rev. Lett. **53**, 1732 (1984).

[113] Zhu, Y., Gauthier, D. J., Morin, S. E., Wu, Q., Carmichael, H. J., and Mossberg, T. W., *Vacuum rabi splitting as a feature of linear-dispersion theory: Analysis and experimental observations*, Phys. Rev. Lett. **64**, 2499 (1990).

[114] Reimann, R., Alt, W., Kampschulte, T., Macha, T., Ratschbacher, L., Thau, N., Yoon, S., and Meschede, D., *Cavity-Modified Collective Rayleigh Scattering of Two Atoms*, Physical Review Letters **114**, 023601 (2015).

[115] Feynman, R. P., *Simulating physics with computers*, International Journal of Theoretical Physics **21**, 467 (1982).

[116] Bloch, I., Dalibard, J., and Nascimbene, S., *Photonic quantum simulators*, Nat Phys **8**, 267 (2012).

[117] Blatt, R. and Roos, C. F., *Quantum simulations with trapped ions*, Nat Phys **8**, 277 (2012).

[118] Houck, A. A., Türeci, H. E., and Koch, J., *On-chip quantum simulation with superconducting circuits*, Nature Physics **8**, 292 (2012).

[119] Aspuru-Guzik, A. and Walther, P., *Photonic quantum simulators*, Nat Phys **8**, 285 (2012).

[120] Rechtsman, M. C., Zeuner, J. M., Plotnik, Y., Lumer, Y., Podolsky, D., Dreisow, F., Nolte, S., Segev, M., and Szameit, A., *Photonic floquet topological insulators*, Nature **496**, 196 (2013).

[121] Unanyan, R. G., Otterbach, J., Fleischhauer, M., Ruseckas, J., Kudriašov, V., and Juzeliūnas, G., *Spinor slow-light and dirac particles with variable mass*, Phys. Rev. Lett. **105**, 173603 (2010).

[122] Angelakis, D. G., Das, P., and Noh, C., *Probing the topological properties of the jackiw-rebbi model with light*, Scientific Reports **4**, 6110 EP (2014).

[123] Shen, S.-Q., *Topological Insulators: Dirac Equation in Condensed Matters*, Springer-Verlag Berlin Heidelberg (2012).

[124] Hasan, M. Z. and Kane, C. L., *Colloquium: Topological insulators*, Rev. Mod. Phys. **82**, 3045 (2010).

[125] Ryu, S., Schnyder, A. P., Furusaki, A., and Ludwig, A. W. W., *Topological insulators and superconductors: tenfold way and dimensional hierarchy*, New Journal of Physics **12**, 065010 (2010).

[126] Jackiw, R., *Fractional and majorana fermions: the physics of zero-energy modes*, Physica Scripta **2012**, 014005 (2012).

[127] Karpa, L., Vewinger, F., and Weitz, M., *Resonance Beating of Light Stored Using Atomic Spinor Polaritons*, Physical Review Letters **101**, 170406 (2008).

[128] Ruseckas, J., Kudriašov, V., Juzeliūnas, G., Unanyan, R. G., Otterbach, J., and Fleischhauer, M., *Photonic-band-gap properties for two-component slow light*, Phys. Rev. A **83**, 063811 (2011).

[129] Lee, M.-J., Ruseckas, J., Lee, C.-Y., Kudriašov, V., Chang, K.-F., Cho, H.-W., Juzeliānas, G., and Yu, I. A., *Experimental demonstration of spinor slow light*, Nature Communications **5**, 5542 (2014).

[130] Chang, D. E., Gritsev, V., Morigi, G., Vuleti, V., Lukin, M. D., and Demler, E. A., *Crystallization of strongly interacting photons in a nonlinear optical fibre*, Nature Physics **4**, 884 (2008).

[131] Maynard, M.-A., Bouchez, R., Lugani, J., Bretenaker, F., Goldfarb, F., and Brion, E., *Time-dependent phase shift of a retrieved pulse in off-resonant electromagnetically-induced-transparency˘based light storage*, Phys. Rev. A **92**, 053803 (2015).

[132] Klein, O., *Die reflexion von elektronen an einem potentialsprung nach der relativistischen dynamik von dirac*, Zeitschrift für Physik **53**, 157 (1929).

[133] Chodos, A., Jaffe, R. L., Johnson, K., and Thorn, C. B., *Baryon structure in the bag theory*, Phys. Rev. D **10**, 2599 (1974).

[134] Semenoff, G., Matsumoto, H., and Umezawa, H., *Fermion zero modes, supersymmetry, and charge fractionalization of quantum solitons*, Phys. Rev. D **25**, 1054 (1982).

[135] Keil, R., Zeuner, J. M., Dreisow, F., Heinrich, M., Tünnermann, A., Nolte, S., and Szameit, A., *The random mass Dirac model and long-range correlations on an integrated optical platform*, Nature Communications **4**, 1368 (2013).

[136] Shankar, R., *Renormalization-group approach to interacting fermions*, Rev. Mod. Phys. **66**, 129 (1994).

[137] Thirring, W. E., *A soluble relativistic field theory*, Annals of Physics **3**, 91 (1958).

[138] Souza, J. A., Figueroa, E., Chibani, H., Villas-Boas, C. J., and Rempe, G., *Coherent Control of Quantum Fluctuations Using Cavity Electromagnetically Induced Transparency*, Physical Review Letters **111** (2013).

[139] Kimble, H. J., *Strong interactions of single atoms and photons in cavity qed*, Physica Scripta **1998**, 127 (1998).

[140] Jing, B., Wang, X.-J., Yu, Y., Sun, P.-F., Jiang, Y., Yang, S.-J., Jiang, W.-H., Luo, X.-Y., Zhang, J., Jiang, X., Bao, X.-H., and Pan, J.-W., *Hybrid entanglement of three quantum memories with three photons*, ArXiv e-prints (2018).

[141] Angelakis, D. G., Huo, M.-X., Chang, D., Kwek, L. C., and Korepin, V., *Mimicking interacting relativistic theories with stationary pulses of light*, Phys. Rev. Lett. **110**, 100502 (2013).

[142] Wallnöfer, J., Zwerger, M., Muschik, C., Sangouard, N., and Dür, W., *Two-dimensional quantum repeaters*, Phys. Rev. A **94**, 052307 (2016).